Turbulence forecasting over South Africa using diagnostics from the convective scale ensemble prediction system of the Unified Model: a pilot study

by
Lauren Smith

Submitted in partial fulfilment of the requirements
for the degree of

MASTER OF SCIENCE

In the Faculty of Natural & Agricultural Sciences University of Pretoria

Pretoria

July 2022

Turbulence forecasting over South Africa using diagnostics from the convective scale ensemble prediction system of the Unified Model: a pilot study

Lauren Smith

Supervisor:	Prof. L.L. Dyson
Co-supervisor:	Mrs. S. Landman
Department:	Department of Geography, Geoinformatics and Meteorology
Faculty:	Faculty of Natural and Agricultural Sciences
University:	University of Pretoria
Degree:	Master of Science

Abstract

Clear air turbulence is a hazardous micro-scale feature to the aviation industry, and the forecasting thereof remains a significant challenge. Clear air turbulence indices describe possible turbulent development mechanisms and are utilized as a forecasting tool. The selected indices for this research are the Ellrod Turbulence index and the Turbulence Kinetic Energy index converted into the Eddie Dissipation Rate available from the South African Weather Service Convective Scale Ensemble Prediction System. Through eleven 2018 case study investigations over 39 clear air turbulence events, the indices from the Convective Scale Ensemble Prediction System are evaluated against pilot reports of clear air turbulence. That is to establish which indices are better suited for aviation purposes over South Africa. Eleven case studies were identified for three different weather categories namely cut-off lows, upper air troughs and upper air zonal flow. The investigations established that the ensemble average and ensemble probability forecasts of the two indices are skilful in predicting clear air turbulence events. However, there is evidence of under-forecasting event severity over South Africa. In general, the EDR severity forecasts outperformed the Ellrod severity forecasts. However, Ellrod performed better when forecasting clear air turbulence associated with cut-off lows while the EDR outperformed the Ellrod in the upper air trough and upper air zonal flow weather categories. Ellrod had the most missed forecasts when dealing with the upper air trough weather category. The post-processing of the clear air turbulence maps would contribute to current forecasting methods of clear air turbulence by the conjoint display and interpretation of both indices over South Africa.

Declaration

I, Lauren Smith declare that the thesis that I hereby submit for the degree Master of Science at the University of Pretoria, is my own work and has not previously been submitted by me for degree purposes at this or any other tertiary institution.

SIGNATURE: L. Smith

DATE: 10/07/2022

Acknowledgements

I would like to give my thanks and appreciation to:

- Prof. L.L. Dyson (University of Pretoria) for her well rounded advice, endless patience, assistance, and guidance as well as caring support during the course of this study, without it this would have not been possible.
- Mrs. S. Landman (SAWS) for her well rounded advice, assistance and guidance throughout the study. The endless patience and assistance with the programming involved. Above all, I thank her for supplying the CSEPS model data needed to conduct this study.
- Ms. K. Marais and A. Demertzis, the SAWS librarians who always extended a helping hand with acquisition of research articles and books.
- The South African Weather Service for the supplying and giving permission to utilise the observational data.
- The South African Civil Aviation Authority Airport Traffic Navigation System Head Office who gave permission to utilise the waypoint and flight path data.
- The Aviation Safety at Safair Operations (Pty) Ltd, which gave permission to utilise and analyse the pilot reports that were investigated in the study.
- To Ms. S. Kenmuir for her hard work and being an outstanding linguist. Additionally, Mrs. C. Miller for her endless patience, support and advise.
- To my father, for his endless helping hand with proofreading, patience, support and advise.
- To my mother for her loving care, support and patience.
- To the Cape Town Weather Office forecaster personal and the regional manager for their support, understanding and patience.

Contents

List of Figures

List of Tables

List of Abbreviations:

AC	Altocumulus
ACC	Area Control Centre
ACSA	Airport Company of South Africa
AMSL	Above Man Sea Level
Apr	April
CAT	Clear Air Turbulence
CAA	Civil Aviation Authority
Cb	Cumulonimbus
CIT	Convectively Induced Turbulence
COL	Cut-Off Low
CSEPS	Convective Scale Ensemble Predication System
D	Deformation
DEF	Resultant Deformation
DEVG	Derived Equivalent Vertical Gust
DNC	Day Natural Color
DSH	Deformation Shearing
DST	Deformation stretching
EDR	Eddie Dissipation Rate
Ellrod index	Ellrod Turbulence Index
EUMETSAT	European Organisation for the Exploitation of Meteorological Satellites
FABL	Bloemfontein Airport
FAUP	Upington

FIR	Flight Information Region
GFS	Global Forecasting System
ICAO	International Civil Aviation Organization
IR10.8	Infrared single channel 10.8
KH	Kelvin-Helmholtz
LGT	Light
LGTT	Light Turbulence
LLJ	Low Level Jet
MDT	Moderate
MDTT	Moderate Turbulence
Mrch	March
MOGREPS	Meteorological Office Global and Regional Ensemble Prediction System
MOGREPS-G	Meteorological Office Global and Regional Ensemble Prediction System - Global model
MSG	Meteorology Geostationary Second Generation
NCEP	National Centres for Environmental Prediction
NIR1.6	Near Infrared band 1.6
NWP	Numerical Weather Prediction
Oct	October
PBL	Planetary Boundary Layer
PCGRIDS	Personal Computer Gridded Interactive Display and Diagnostic System
PIREP	Pilot Report
Rf	Flux Richardson number

RGB	Red, Green and Blue
Ri	Richardson's number
RSA	Republic of south Africa
SACCA	South Africa Civil Aviation Authority
SAWS	South African Weather Service
Sep	September
SMAG	Smagorinsky model
SVR	Severe
SVRT	Severe Turbulence
TI	Turbulence Index
TKE	Turbulence Kinetic Energy
VIS0.6	Visible band 0.6
VIS0.8	Visible band 0.8
VWS	Vertical Wind Shear
WMO	World Meteorological Organization
WV6.2	Water vapour channel 6.2
WV7.3	Water vapour channel 7.3

Chapter 1 : Introduction

Atmospheric clear air turbulence (CAT) is a hazardous weather phenomenon which has an impact on the Aviation industry. CAT is known to last from a few hours to a day and causes loss of life due to moderate to severe shaking or bumpiness of the aircraft in flight (de Villiers and van Heerden, 2001; Sharman et al., 2006; Venkatesh and Mathew, 2013). The forecasting of CAT remains a significant challenge (Ellrod and Knapp, 1992; Venkatesh and Mathew, 2013; Storer et al., 2017) due to the current limited understanding of the phenomena mechanisms; it being a micro scale feature which demands computing power; and is influenced by the chaotic nature of the atmosphere (de Villiers and van Heerden, 2001, Sharman et al., 2006). CAT is forecasted by turbulence indices such as Turbulent Index 1, Turbulent Index 2, Brown index and the Dutton index as well as by using other variables such as vertical wind shear, horizontal wind speed, and frontogenesis, (Dutton and Panofsky, 1970; Brown, 1973; Hopkins, 1977; Ellrod and Knapp, 1992). The definition of turbulence is further explained in Section 2.1. These indices are derived from numerical weather predication model variables that attempt to capture the meso- and micro scale features of CAT (Ellrod and Knox, 2010). The selected indices for this research are the Ellrod Turbulence Index (TI), referred to as the Ellrod index in this research, and the Turbulence Kinetic Energy (TKE) index, which is converted into the Eddie Dissipation Rate (EDR) index. The indices are readily available, built-in indices of the Convective Scale Ensemble Predication System (CSEPS).

Turbulence is one of the significant hazardous weather phenomena that prevents aircrafts from flying at an altitude which promotes the optimum performance of an aircraft (Storer et al., 2019). Significant airline costs and operational impacts, such as air pollution are associated with encounters of hazardous weather phenomena such as turbulence, where turbulence was found to be the cause of 65% weather-related incidents (Sharman et al., 2006; Storer et al., 2019). The ‘weather-related incidents’ refer to incidents that happen to the pilot in-flight that is outside the pilot control resulting in anything from loss of orientation to a full-blown crash, caused by hazardous weather. Airline costs and flight discomfort may be avoided by means of strategic *en route* planning by pilots when given a confident turbulence forecast

(Sharman et al*.,* 2012). The South African Weather Service (SAWS) aviation weather forecasters endeavour to meet the International Civil Aviation Organization (ICAO) and World Meteorological Organization (WMO) certified organisational requirements, so as to ensure aviation safety (SAWS, 2019).

The Airport Company of South Africa (ACSA) indicated in the 2017/2018 annual report of the South Africa Civil Aviation Authority (SACAA) a passenger growth of 3.8% at O.R. Tambo International Airport, 7.3% at Cape Town International Airport and 8.5% at King Shaka International Airport (Mokoena, 2018). The increase in passenger numbers has resulted in the increase in the number of domestic flights by 2.2% and of international flights by 4.7% (Mokoena, 2018). The annual growth of passenger aircraft flights, no matter how large, can potentially lead to an increase of passengers encountering turbulence over South Africa (RSA).

An escalated risk for the aviation industry of encountering hazardous weather can be based on an ever-increasing demand for domestic and international flights (Khosa, 2019). It is therefore crucial to have the ability to predict the timing, location and severity of CAT accurately (Sharman et al., 2006; Khosa, 2019). Pilots report the locations of CAT utilising waypoints over South Africa. Waypoints are point coordinates *en route* or closest to the airway and/or airport, which are found in the set

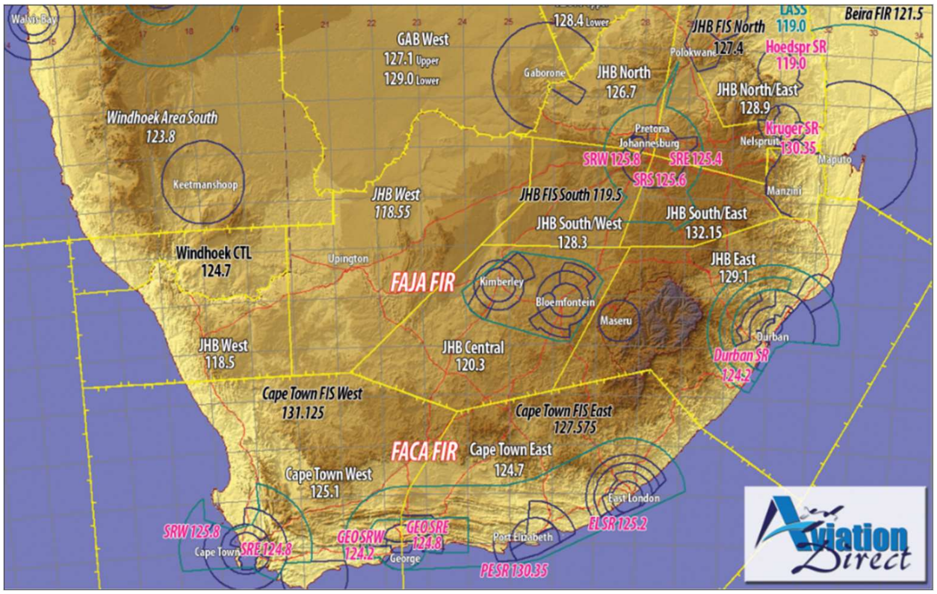

Figure 1.1: Maps of the FIR sectors (yellow line boundaries. South Africa has two main FIR sectors, FAJA (Johannesburg) and FACT (Cape Town) FIRs. It is a section of airspace in which flight information service and alerts are provided. The green and dark blue lines are designated airspace and routes around the airspace. The thin orange lines are motor ways. (image by Aviation Direct, 2020).

flight information region (FIR) and area control centre (ACC) sectors (CAA, 2013), illustrated in Figure 1.1 and 1.2.

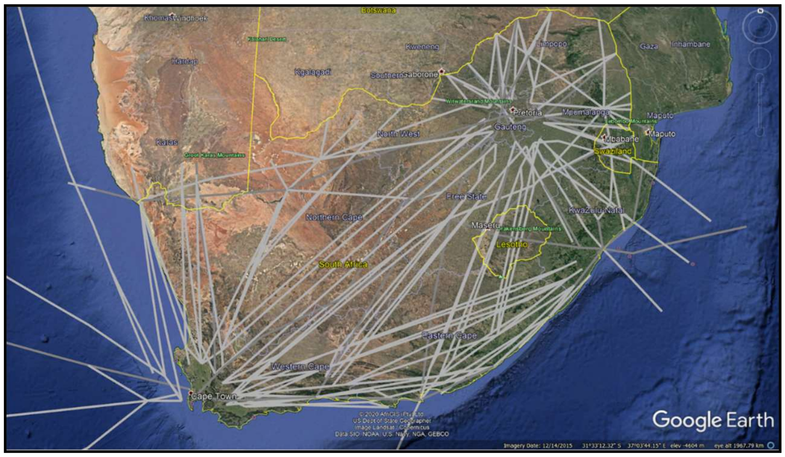

Figure 1.2: Maps of the airways/flight paths (thin grey lines) over South Africa (SACAA AIP ENR 3,3 3/14 and Google Earth, 2020).

Deterministic numerical weather prediction (NWP) model outputs are believed to be less dependable than probabilistic models' output. This is due to the sampling method (Figure 1.3) of uncertainty towards an event from the initial conditions of the ensemble model, and the chaotic and non-periodic characteristics of the atmosphere. The more ensemble members within the model, the higher the skill score but any error or biases in the initial conditions will also be present within the ensemble (Ebert, 2001; Tennant et al., 2007; Landman et al., 2012).

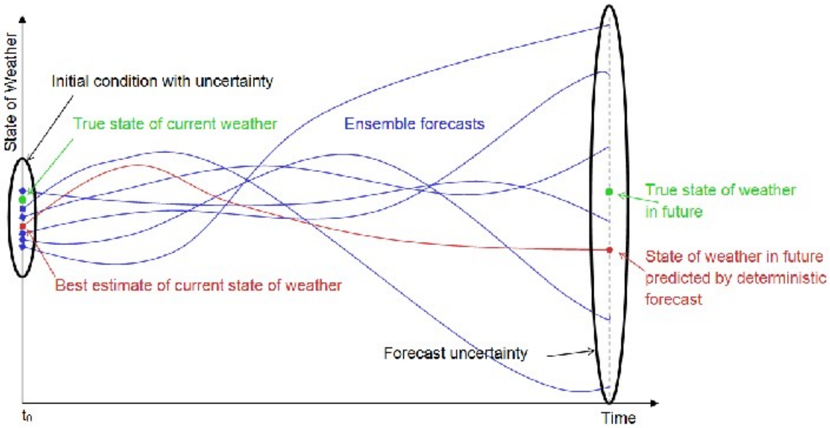

Figure 1.3: A schematic explaining how uncertainty is captured by ensemble model. The ensemble forecasts are closer to the observation (the true state of weather the green dot (Cheung et. al., 2015).

With the understanding that deterministic models carry uncertainty, forecasters subjectively conceptualise the probability of forecast outcomes, by using different single model outcomes based on prior experience of the shortcomings of the model itself (Landman et al., 2012). Yet with the increased availability of data and the combination of turbulence indices it has been proven that deterministic NWP models are accurate (Storer et al., 2019). However, probabilistic NWP models have been shown to be more skilful when the focus is on probabilistic outcomes from a single model rather than a combination of forecaster conceptualized deterministic model outputs.

Kopeć et. al. (2011) stated that the performance of turbulence indices is fairly average. That may be partially due to those indices being over- or underestimated. Gill and Buchanan (2014) and Storer et al. (2019) agree that current probability turbulence indices are utilised in a pragmatic, more sensible and practical approach when establishing probability forecasts, instead of empirically referring to more of an observational (did it occur or did it not occur) approach (Gill and Buchanan, 2014; Storer et al., 2019). A further contributing factor is the deficiency in resolution and the understanding of CAT mechanisms (Section 2.1.1) affecting the forecasting of CAT as a phenomenon (Kopeć et. al., 2011). An ensemble forecast systems' main objective is to address the uncertainty of a forecast by predicting the probable outcome of the weather event that is deterministically represented (Landman et al., 2012). Hence, due to the combination of several different initial assimilations for each ensemble member within a single model, an ensemble prediction system is generated. The combined principle of probability with determinism in turn provides a forecast event or non-event (Landman et al., 2012). Therefore, utilising an ensemble NWP system, the performance of the forecast could be increased so as to decrease the level of uncertainty within the forecast (Gill and Buchanan, 2014). A single ensemble model is therefore chosen for the purpose of this study.

The SAWS in-house convective scale ensemble prediction system (CSEPS) has numerous diagnostics for CAT prediction, but these have not been verified to establish skill and usability. Research is required to establish whether the CSEPS CAT indices can be used to produce CAT forecast maps over South Africa. One of the advantages of using the CSEPS is that there were 12 ensemble members available between 2012 and 2018, after which 6 more members were added. In this dissertation 12 ensemble members are utilised and the CSEPS ensemble average and ensemble probability forecasts are compared to observations. The CSEPS forecasts are all available at a 4.5 km horizontal resolution.

Conducting case studies is considered meaningful in meteorology as research case studies are considered empirical investigations towards extreme or rare weather events (Schultz, 2010; Wedawatta et al., 2011). Case study research provides a breakdown of a significant weather and goes about identifying and analysing that weather event, while applying theory (Schultz, 2010). This approach benefits the forecasting methodology by suggesting new improved procedures. Case studies also lead to new understanding of model performance and practical understanding of the phenomenon investigated and they may contribute to the post processing of NWP systems (Wedawatta et al., 2011). This dissertation makes use of case studies to determine the accuracy of turbulence forecast on events basis. There is only a limited number of turbulence observations which makes a comprehensive statistical analysis unsuitable.

1.1 Aim and objectives

The intention of this dissertation was to determine if the ensemble average and probabilistic forecast of the Ellrod index and TKE converted into the EDR, available from the CSEPS, predict known turbulence events over South Africa.

The aim of this study, therefore, was to determine if the Ellrod and EDR indices, can predict clear air turbulence over South Africa utilising the ensemble average and probabilistic forecast from the CSEPS. The aim is accomplished through the following objectives:

1. Identify thresholds for the Ellrod and EDR indices from literature and compare the ensemble average and probabilistic forecast to known CAT events.
2. Do a subjective comparison of the CAT forecast against pilot reports (PIREPs) to establish which index proves to be more accurate when utilising the thresholds specific for aviation over South Africa.
3. Analyse the accuracy of CAT forecast for different weather systems.
4. Provide recommendations as to the application of the indices to predict CAT in an operational environment over South Africa when utilising the CSEPS.

The necessary steps that were taken in order to achieve the objectives were:

a. Turbulence observations (PIREPs) were obtained from the Civil Aviation Authority (CAA) of South Africa for the year 2018. (Chapter 3;4);

b. Threshold values for the indices were found from literature and compared to the Ellrod and EDR forecasts. These values were used to compare the CSEPS CAT forecasts to turbulence observations for 11 case studies over South Africa (Chapter 3;4);

c. Three weather categories were identified and the CAT forecast skill for Ellrod and EDR was tested for the three categories separately (Chapter 4);

d. The ensemble average and ensemble probability forecasts of all 11 case studies were subjectively evaluated to establish the usefulness of the Ellrod and EDR indices (Chapter 4;5).

This dissertation consists of six chapters. This chapter 1 describes the aim and objectives towards the research problem. Chapter 2 defines turbulence and highlights forecasting techniques thereof. The data and methodology used in this study for the generation of the ensemble average and ensemble probability forecast events are described in Chapter 3. The case studies are presented in Chapter 4 along with the CSEPS output discussion followed in Chapter 5. A summary concluding this study findings along with recommendations and limitations of this thesis are given in Chapter 6.

Chapter 2 : Background Literature

The following Section discusses the definition of turbulence, specifically clear air turbulence but different types of turbulence is also discussed. Current clear air turbulence forecasting approaches will also be detailed.

2.1 Turbulence

The planetary boundary layer (PBL) is the lowest portion of the atmosphere that interacts directly with the earth's surface (Holton, 2004; Wallace and Hobbs, 2006). In the PBL, the wind flow is influenced by viscosity interactions, which entails internal friction causing resistance to wind flow resulting in non-uniform flow. This results in turbulent eddies (Holton, 2004). Eddies are swirls of many sizes occurring within the airflow (Wallace and Hobbs, 2006).

Turbulent motion is not only found near the surface but may also occur in the free atmosphere, i.e. the region above the PBL. It can also occur in the locality of fronts, jet streams, cloud-free regions, and convective motion at higher altitudes (Holton, 2004, Overeem, 2002). Any superimposed wind flow that contains eddies are evanescent and are replaced by the succession of different sizes of eddies, thereby promoting the continuum of turbulent eddies (Wallace and Hobbs, 2006, Holton, 2004). The resulting turbulent eddies have temporal and spatial scales which range from planetary scale to mesoscale to less than 2 mm (Storer et. al., 2019; Wallace and Hobbs, 2006).

Turbulent eddies are also generated through a process called the *turbulence cascade,* where the inertial energy of the large eddies is transferred to smaller eddies (Wallace and Hobbs, 2006). Inertial energy is referring to the uniform moving energy that will continue until by some other force (friction) changes either the direction or speed or both. Large turbulent eddies, therefore, experience a loss of energy and the eddy motion may be quantified in terms of the atmospheric energy budget and, more specifically, the rate at which the kinetic energy is dissipated (Wallace and Hobbs, 2006).

TKE is energy that is not conserved within the atmosphere and dissipates into internal energy as a result of viscosity, even at the molecular scale (Wallace and Hobbs, 2006). The TKE equation is found by subtracting the component of the mean momentum equations (See Holton (2004), equations 5.9-5.11 p.119) from the unaveraged equations of momentum in cartesian co-ordinates (See Holton (2004), and equations 5.1-5.2 p.117). The resulting three equations must be added and averaged to show the TKE equation (equation 3.9) (Holton, 2004) (Section 3.3.2.d).

Turbulence continues to exist when there is a continual generation of eddies generated from shear or buoyancy that counterbalances the energy transfer of kinetic energy within the energy cycle, which eventually dissipates (Wallace and Hobbs, 2006). The TKE equation may confirm the link between the transportation of heat and moisture, which leads to the Taylor's hypothesis.

The Taylor's hypothesis describes turbulence as a motion that can be measured at a fixed point while atmospheric motion passes at that point in time. Wind speed can then be translated into a turbulent measurement. This measurement has a U and a V component which represents the x- and y-cartesian wind directions (Stull, 1988). The hypothesis is represented by an equation shown as:

$$M^2 = U^2 + V^2 \qquad 2.1$$

where M is denoted as the maximum wind magnitude, and U and a V are the eastward-moving and northward-moving cartesian wind directions.

Furthermore, when the eddy has a diameter of ʎ and is advected at a mean wind speed (M) at the time period (P) at a fixed point, then

$$P = ʎ/M \qquad 2.2.$$

When the temperature differs at two opposite points of the eddy motion, for example, 10 °C at the initial point and 5 °C is measured 10 seconds later, with a mean wind speed of 10 m/s, then the calculation of the temperature change is done by using the following equation:

$$\frac{\partial T}{\partial t} = -M\partial T/\partial x_d \qquad 2.3$$

Where, $\frac{\partial T}{\partial t}$ denotes the temperature gradient, x_d is in a direction parallel to the mean wind

Therefore, the temperature change, or temperature gradient, at that point will be $\frac{\partial T}{\partial t} = -0.5$ Ks^{-1} where equation 2.3 is the final expression of the Taylor's hypothesis for temperature in one dimension. This equation may be written in terms of frequency f, radius per time, wavenumber k , and radius per unit length, where $k = 2\pi/\Lambda$ and $=$ $2\pi/P$, along with $\sigma_M < 0.5, M$ being the standard deviation of the wind speed (Willis and Deardorff, 1976). This equation is said to be a measurement of turbulent intensity when the turbulent eddy is small in relation to the mean wind speed (Stull, 1988).

Stull (1988) also describes turbulence as irregular swirls of motion (eddy motion) and divides wind into three categories, namely mean wind, perturbations, and waves. These may occur alone or all at once. Previous studies have stated that the main processes that result in turbulence are large temperature and wind velocity gradients within the atmosphere (Overeem, 2002).

Turbulence is largely driven by kinetic energy within the atmosphere and is dependent on the instability of the atmosphere. It may be measured by a term denoted by the Flux Richardson number (Rf):

$$Rf = -BPL/MP \qquad 2.4$$

Where,

$$BPL = \overline{w'\theta'}(\frac{\bar{g}}{\theta_0}) \text{ , and} \qquad 2.5$$

$$MP = -\overline{u'w'}\frac{\partial\bar{u}}{\partial z} - \overline{v'w'}\frac{\partial\bar{v}}{\partial z} \qquad 2.6$$

Where, $\overline{w'\theta'}(\frac{\bar{g}}{\theta_0})$, $\overline{u'w'}\frac{\partial\bar{u}}{\partial z}$, $\overline{v'w'}\frac{\partial\bar{v}}{\partial z}$, are the mean potential temperature vertical velocity, vertical flux of zonal momentum, the basic state zonal flow vertical shear respectively.

The Rf number takes buoyancy into account; thus the vertical motion of the atmosphere is included and not only the horizontal eddy advection passing a fixed point (Holton, 2004; Stull, 1988). When the Rf number results in a negative term in a statically unstable atmosphere, convective motion is seen as the cause of turbulence. Convective motion occurs when the earth's surface is heated by the sun, and the warm surface, in turn, heats the bottom layer of the atmosphere, resulting in a statically unstable atmosphere. The unstable atmosphere responds by creating thermals. Thermal motion occurs when warm air rises, and cold air moves down to recreate the equilibrium the atmosphere once had. Once this equilibrium is reached, the atmosphere is known to be statically neutral, and turbulence may cease (Wallace and Hobbs, 2006). If the Rf number results in a positive term, then it is suggested that the mechanical production is strong enough, and turbulence is thus produced in a statically stable atmosphere. However, if the static stability increases, the production of turbulence decreases. For example, when a temperature inversion forms due to radiative cooling, the potential for turbulent eddies is decreased (Holton, 2004).

The diameter of each eddy may differ within the general eddy field and may be very small. The temporal scale of eddies is exceptionally short, from a few seconds to a few minutes to half an hour, depending on the size of the eddy. It thus diminishes the forecast skill to deterministically forecast turbulence at a useful period of a day or two ahead (Wallace and Hobbs, 2006). If the dissipation of kinetic energy is constant, then it is implied that the kinetic energy would be renewed in 2.6 days in the free atmosphere, thus rendering a forecast of more than two days ahead as being useless (Holopainen, 1962). It is, therefore, difficult to explicitly simulate eddy motion to a size scale that has an effect on aviation (approximately an eddy of a 100 m scale has an influence on an aircraft (Sharman et al., 2006)) within forecasting numerical prediction models since some of the numerical prediction models have too coarse a resolution (Storer et. al., 2019).

Turbulent indices are used to describe the net effect of many eddies. Based on the aforementioned reason, and since diagnostics in a general sense calculate turbulence based on the principle that the energy will have an influence, then the aviation scale will cascade down from large to small (Storer et. al., 2019).

In the following paragraphs, the six different turbulent mechanics will be investigated. Clear air turbulence will be discussed in more depth, as it is the main focus of this study. The discussion will provide a further understanding of the production of clear air turbulence and the effects turbulence has on the aviation industry. The other five different turbulent mechanics are, wake vortex turbulence, mountain waves, turbulence due to convection, low-level wind shear and low-level jets.

2.1.1 Clear air turbulence

Clear air turbulence (CAT) is the main subject of this research. CAT is described in many research articles, and the majority of authors agree that CAT is defined as a non-homogeneous layer above the PBL. The definition includes that CAT is ‘bumpiness’ encountered in a cloud-free region, that is not in or near to visible convective activity such as thunderstorms. Some definitions may exclude cirrus clouds, while others include them (Hopkins, 1977; Kopeć et. al., 2011; Haman and

Bajer, 2011). Wind directional and speed shear also have to be present (Hopkins, 1977; de Villiers and van Heerden, 2001; Overeem, 2002).

CAT is said to have a life span that is shorted lived (few minutes) and may be long in duration (half an hour to days) within an atmospheric layer (Overeem, 2002). The vertical dimension of CAT is thought to be between 200 m to 1500 m thick (Hopkins, 1977) but may also have a vertical dimension of 500 – 1000 m and even 25 – 4500 m (Overeem, 2002). The horizontal dimension of CAT is described as 80 – 500 km along the wind direction and 20 – 100 km across the wind flow (Overeem, 2002). To describe the region dynamically where CAT is found the Boussinesq approximation is made with the layer in which CAT occurs. The density variation is only important with regards to the buoyancy term and thus the density become constant, and the buoyancy term negative (incompressible atmosphere) therefore referred to as incompressibility assumption (see equation 2.8) (Dolaptchiev et.al., 2019). CAT is associated with strong vertical and horizontal wind shear, and generally develops more frequently over mountainous regions than over plains and the ocean (Colson and Panofsky, 1965). In this dissertation the CAT diagnostics (Section 3.3.2) are only studied over the continent of South Africa. CAT is developed by mechanisms that are related to standing waves on the lee side of a mountain and wind shear in a statically stable layer, as well as where the highest-velocity wind speeds and tight horizontal temperature gradients are evident (Hopkins, 1977). A CAT event is classified into three categories: light, moderate, and severe which is detailed in Table 2.1 (Dutton, 1971; de Villiers and van Heerden, 2001; Gill and Buchanan, 2014).

Table 2.1: Subjective clear air turbulence classification guide (de Villiers and van Heerden, 2001; World Meteorology Organization, 2007)

Category	**Description**
Light	Slight bumpiness whereby the pilot will put the seat belt sign on.
Moderate	Passengers are required to remain seated due to difficulty in moving around as well as loose objects that may shift around onboard. Slight changes in aircraft altitude and in accelerometer readings.
Severe	Violent jolting of the aircraft in all directions, including passengers being thrown from side to side. Loose objects are tossed around in

the cabin and cockpit. The aircraft is difficult to control. May also include damage to the aircraft, significant and quick changes in aircraft altitude and in accelerometer readings.

The known and accepted CAT formation mechanisms are inertia gravity waves that may venture in non-linear regimes and break (mountain wave-induced CAT) and Kelvin-Helmholtz instability which is associated with wind shear (Overeem, 2002, Storer et. al., 2019). These mechanisms are also more likely in winter months since temperature gradients and wind speeds are stronger and more frequently developed in winter of the southern hemisphere (Overeem, 2002), although this is not to say that CAT doesn’t exist in the summer months. It is seen within an atmospheric profile, after the onset of CAT between two inversion layers (stable lapse rate), an unchanging wind speed associated with a constant water vapour mixing ratio is found bounded within the layer. Hence shear and instability are seen above an adiabatic layer due to the mixing of eddies above and below the adiabatic layer which transports heat and momentum (Overeem, 2002).

Kelvin-Helmholtz (KH) instability is a result of strong vertical wind shear due to waves that become amplified and that have then tumbled over into a thin stable layer of the atmosphere (generating eddies), like the waves of the ocean. The associated wind shear in the formation of CAT in a statically stable layer has been connected to the KH instability. Amongst other instability indicators, it is the most popular used to described CAT (Hopkins, 1977; Overeem, 2002). The energy decreases into mesoscale turbulence eddies, negative buoyancy, and heat, and appears as wave-like clouds called *Billow clouds*, as shown in Figure 2.1 (Hopkins, 1977).

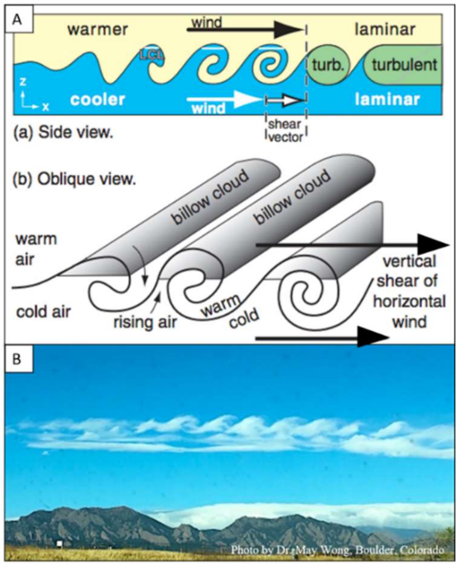

Figure 2.1: (A) Schematic of Kelvin-Helmholtz wave formation. The difference in airspeed of the warm air and cold air results in vertical shear. (B) A photo of Kelvin-Helmholtz cloud waves (Stull, 2018; Photo by Dr May Wong, Boulder, Colorado).

The energy source of KH instability is the mechanical energy that is produced from wind shear. CAT may persist when the initial mechanical energy production source contains strong enough vertical wind shear to overcome the stability and become an unstable layer. Under these conditions, the basic state available potential energy is generated from diabatic processes, it is then converted into eddy available potential energy, which in turn is converted into eddy kinetic energy (or turbulent kinetic energy). The eddy kinetic energy (turbulent eddies) continues to increase until the dissipation rate equals that of the production rate. The eddy motion (perturbations) loses energy when it is either converted into basic state kinetic energy or if it dissipates by means of wind shear (internal friction) generated by breaking synoptic Rossby waves. a great majority of the TKE is converted to potential energy (Overeem, 2002). The continuous increase of the turbulent eddies results in greater entrainment within the layer. If there is a capping inversion layer, the $\Delta\theta$ (potential temperature) diminishes entrainment by reducing the inertial energy increase resulting from the inertial production of thermals and eddies (Wallace and Hobbs, 2006). Hence, resulting in a boundary layer that is deepening, becoming warmer and drier (Bopape et al., 2020). The rate at which TKE is generated by buoyancy is proportional to the up and down motion (sensible heat flux) of the warm air within the turbulence layer (Wallace and Hobbs, 2006).

In a stable layer in a cloud free region, turbulence can occur when the inertial mechanical production of CAT is able to overcome the effects of increased stability and viscosity (Holton, 2004). The Rf (Section 2.1) equation 2.4 can be simplified to equation 2.7 known as the Richardson's number (*Ri*):

$$Ri = \frac{g\partial\theta}{\theta\partial z} / (\left|\frac{\partial \vec{V}}{\partial z}\right|)^2 \qquad 2.7$$

if the assumption is made that in a statically stable environment the wind shear production is strong enough to overcome the static stability. Where g denotes the acceleration of gravity, θ is potential temperature, $\underset{V}{\rightarrow}$ denotes the horizontal wind vector and z is the geopotential height.

Positive buoyancy reduces TKE when converted into potential energy by means of thermal motion as described above. The resulting environmental turbulence is thus dependent on the strength of the inertial mechanical production by wind shear against the depletion of buoyancy resulting from the increase in static stability (Holton, 2004; Wallace and Hobbs, 2006). Therefore, the Ri depicts the ratio between potential temperature and horizontal wind vector at a given geopotential height. This ratio depicts the rate at which turbulent energy is depleted and the decrease in buoyancy in the stable atmospheric layer which is caused by vertical wind shear (Hopkins, 1977). Previous research has shown that when the Ri is 0.25, then Kelvin-Helmholtz instability occurs (Hopkins, 1977; Wallace and Hobbs, 2006; Colson and Panofsky, 1965); however, it is seldom computed by the NWP models (Storer et al., 2019). This has been attributed to the NWP models' resolution being too coarse since turbulent regions could be smaller than 100 km which will more likely affect aircraft, as thresholds are NWP model specific (Storer et al., 2019).

Kelvin-Helmholtz instability relating to CAT may exist and increase in severity when the above-mentioned conditions are met. These conditions attributed to CAT are small-scale motion of negative buoyancy and heat within a stable layer of air. It has been reported that when meso-scale or larger atmospheric scale motion contribute to the generation of CAT, the motion needs to be ageostrophic. Geostrophic motions may not change the potential temperature gradient and therefore may not always result in CAT production (Overeem, 2002). Ageostrophic motion refers to wind flow opposite to that of the main geostrophic wind, resulting from the pressure gradient force i.e., wind flow of different speed and direction as to that of the main airflow in the horizontal in the mid to upper atmosphere (Wallace and Hobbs, 2006).

2.1.2 Clear air turbulence areas

Meso-scale synoptic patterns form thin vertical baroclinic layers or frontal zones with associated stability and wind shear, this being due to continuous motion towards equilibrium within the atmosphere. Trough or frontal regions are associated with extratropical cyclones in the mid-latitudes along with upper air jet streams. These synoptic-scale weather patterns may therefore develop the ideal conditions for KH instability to occur, which will then potentially result in CAT (Ellrod et al., 2003). The amplification or curvature of the trough line and jet streams as well as the sharply concave anticyclonic flow, are characteristic of ageostrophic flow (Ellrod et al., 2003).

The resulting regions that are prone to CAT development within synoptic patterns are mainly associated with: upper air troughs/perturbations; shear layers near the tropopause due to CAT being a function of height and wind shear; within baroclinic regions below the upper air jet stream core; on the cold side of the jet (on the low-pressure side); and the area related to the confluent and diffluence region of two jet streams (Ellrod et al., 2003).

de Villiers and van Heerden (2001) have reported that CAT occurs over South Africa (RSA) at higher altitudes in the atmosphere and is closely related to the upper air jet stream. This corresponds to other global areas, such as in America where the Rocky Mountains produce mountain wave-induced CAT, and which is influenced by mid-latitude cyclones. A study in Japan also concluded that CAT is related to upper air troughs and upper air jet streams A study done in 1965 by Binding (1965), cited by Hopkins (1977) stated that CAT is observed 61% of the time over the North Atlantic where, of that observed are more likely of moderate to greater in severity. This includes association with cyclonically curved jet streams cores as opposed to sharp ridges (Hopkins, 1977; Sharman et al., 2006; Chan and Wong, 2014). A jet stream is defined generally as fast narrow current of moving air. The upper air jet stream is situated near the tropopause (the zone separating the stratosphere and troposphere) where the zonal wind flow is at a maximum, generally indicated from 30 ms^{-1} and more (Figure 2.2) (Holton, 2004; Gallego et al., 2005; Spensberger et al., 2017).

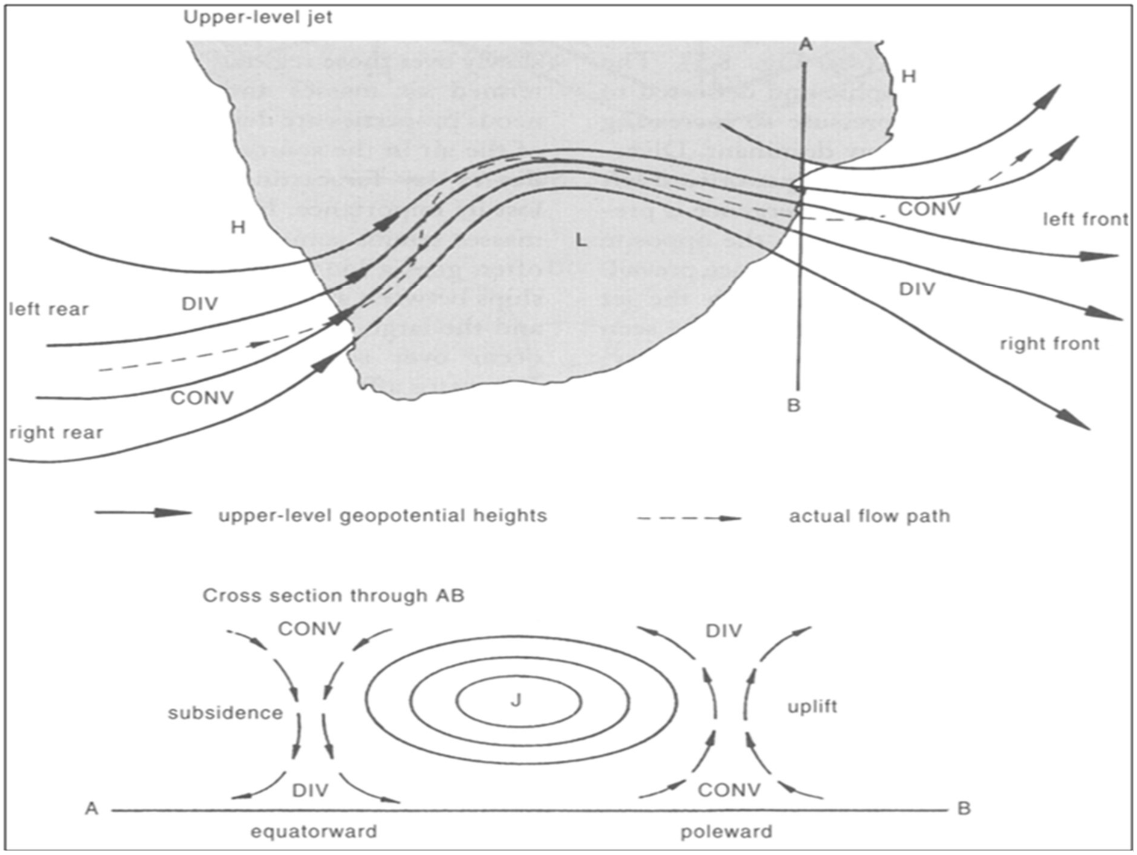

Figure 2.2: A schematic diagram of the subtropical jet stream over South Africa. The figure shows the convergence (CONV) and divergence (DIV) zones of the upper-air jet stream at the (rear and front) entry and exit, respectively. The jet stream follows a natural curvature (dashed arrows) along the pressure gradients (upper-level geopotential heights, solid arrows). The cross-section (AB) depicts the vertical motion at the polar- and equator-sides of the jet stream as a result of convergence and divergence (adopted from Preston-Whyte and Tyson, 1988, p. 160).

If an upper-air jet stream (marked by the actual flow path, dashed arrows in Figure 2.2) is associated with an upper-air trough, (marked by the upper-level geopotential heights, solid black arrows) which has a well-developed curvature, then the confluence and diffluence will have significant effects on the strength of the jet stream, as depicted in Figure 2.2. Diffluence is usually the result of a Coriolis force being greater than the momentum balance and is found on the poleward, right-front region of the jet stream. The motion becomes dominated and thus ageostrophic since the wind moves outwards and to the right, following a path towards higher pressure, thereby increasing the diffluence. On the other side, towards the equator, a confluence is dominant at the exit region of the jet stream. At the rear side of the jet stream, the diffluence region towards the jet stream is on the equator side and the confluence takes place on the poleward side of the jet stream (Preston-Whyte and Tyson, 1988, p. 160).

The upper air jet stream wind acceleration results from cross-stream pressure gradients resulting from the ageostrophic motion. This leads to vorticity differences on either side of the jet stream core, thereby causing significant vertical and horizontal wind shear near the edges (Hopkins, 1977; de Villiers and van Heerden, 2001). CAT can develop in the baroclinic region below the jet stream core near the tropopause (Ellrod et al., 2003). The baroclinic region is the area of maximum cyclonic curvature of the trough (northeast relative to the shear line) in the Southern Hemisphere, on the cold side of the jet stream, i.e. on the low-pressure side of the core (Figure 2.2). An increase in wind shear and instability of the atmosphere will thus increase the severity of CAT production (de Villiers and van Heerden, 2001).

Upper-level jet streams are associated with wind shear and with upper air macro-scale weather patterns that result in the development of CAT prone regions, such as steep upper air troughs, upper air cut-off low (COL) pressures, ridges and baroclinic instability (Ellrod et al., 2003). The jet stream is not only associated with baroclinic instability but also frequently develop in association with barotropic instabilities. These instabilities are linked to vertical and horizontal shear and barotropic instability waves become amplified by obtaining kinetic energy from the westerly mean-flow field (Holton, 2004).

Baroclinic waves become amplified by adapting potential energy due to the horizontal temperature gradient (Holton, 2004). The baroclinic motion of the atmosphere associated with the mid-latitude upper air jet stream results in an upstream motion of eddy potential energy. The eddy potential energy reaches a maximum before the closed COL is developed. The amplification is due to the conversion of eddy potential energy into eddy kinetic energy. The downward motion of the eddy kinetic energy will be at its maximum in the same location where the closed upper air low pressure forms (Ndarana et al., 2020). The development of a COL strengthens when the energy conversion of potential eddy energy to kinetic eddy energy is strengthened. This is based on the influx of energy from ageostrophic changes which are responsible for the transport of eddy kinetic energy in a north-eastwards flow from the upstream centre (Ndarana et al., 2020).

In the subtropics, baroclinic waves associated with the subtropical jet stream propagates eastwards in the mid-latitudes of the southern hemisphere, and when an upper air trough develops towards the equator, a split in the westerly flow occurs. This occurs when a trough of cold air aloft at the mid-upper troposphere becomes 'cut-off' from the main westerly flow (Singleton and Reason, 2007; Stander et al., 2016). The COL (Figure 2.3) pressure aloft may be associated with a strong surface high pressure to the south of the system. This surface high pressure may, at times, intrude along the west-east axis into an area of lower pressure which is then called a ridging high-pressure (Stander et al., 2016). The COL may also deepen to the surface east of the upper air system. The orientation of the low pressure aloft which is cut-off together with the low-pressure extending to the surface gives rise to a baroclinic structure (Singleton and Reason, 2007; Stander et al., 2016).

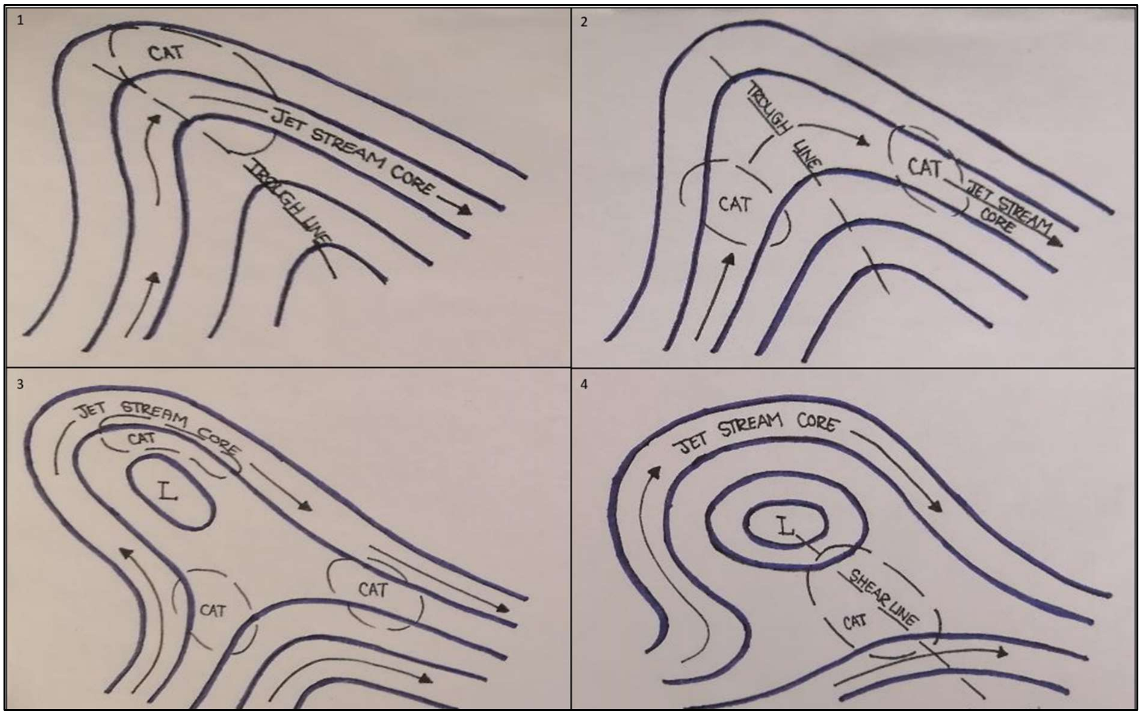

Figure 2.3: A schematic diagram of CAT associated with the formation of a COL. (1) CAT is more likely to develop on the east side of the trough line to the north of the lowest pressure, where the maximum cyclonic curvature occurs. Moderate to severe CAT may be found after maximum amplification of the upper-air trough. (2) The trough will amplify and regions of confluence and diffluence become stronger resulting in CAT development in those regions. (3+4) The low pressure is now 'cut-off' and light to moderate CAT may be associated with the region just north of that low pressure. Moderate to severe CAT may occur around the 'throat' which is the zone between the 'cut-off' low and mean westerly flow (adopted from Holton, 2004, and redrawn by L. Smith).

Before a COL is fully developed, the CAT development area in connection with sharp cyclonic motion is divided into three Sections. The first association is the actual amplification of the upper air trough (Figure 2.3 1). Secondly, CAT is then connected to the downstream motion resulting from cyclogenesis relative to the upper air trough

(Figure 2.3 2). Thirdly, CAT is found to the north in connection with the redevelopment of a jet stream core when cyclogenesis is generated to the left of the main jet stream core (Figure 2.3 3) (Hopkins, 1977). All three scenarios may occur separately or all at once (Hopkins, 1977). The CAT is at its maximum within the region north of 100% amplification and is thus the area of maximum cyclonic horizontal shear resulting from the jet stream core (Figure 2.3 1). CAT is also much more likely to be generated in the region just to the rear of an upper air trough, within the ridge. That is the north-south to south-east direction flow which results in CAT occurring near the outflow region of the north-south upper air jet stream and within the region known as the ‘neck’ (Figure 2.3 4) (Hopkins, 1977).

The location of CAT prone spots that are associated with COL developments are found to be within confluent and diffluent regions. The area that is between the main flow westerly jet stream, ageostrophic motion, and the jet stream, which is linked to the cut-off low pressure, is known as the diffluence region (Figure 2.3 3). In addition, confluent regions on the north-south downward motion of the upper air jet stream are found around the COL. The confluent region relating to an upper air trough is highly likely to develop CAT when two jet streams are about 500 km apart, and when the northern jet stream core is associated with cold air at a lower atmospheric level than the southern jet stream core. This will result in static stability as well as strong upper air vertical wind shear within the confluent region (Hopkins, 1977).

The vertical motion can be noted on an upper air sounding, where noticeable backing with wind is seen between the two jet stream cores. CAT is generated within a diffluence region and is likely to increase in severity when associated with a surface low pressure that has cold front characteristics. The severity of the CAT event is likely to be light with vertical dimensions of about 600 m above the tropopause and which extends down to approximately 2000 m from the tropopause. Other regions where CAT can develop is within the region to the northeast where the atmosphere is stable, and thus processes can take place according to the thermal wind equation which results in conditions becoming favourable for KH instability (Hopkins, 1977).

The severities of CAT that are known to develop when associated with a COL, are light CAT just south of the low-pressure centre, as shown in figure 2.3 (4). Moderate CAT is found in the centre or ‘throat’ of the COL (Figure 2.3 4), where two opposing cyclonically curved flows can occur between the ‘cut-off’ low and the main westerly mean flow, where the wind speed is at least 25 ms^{-1}. Hopkins (1977) has stated that moderate to severe CAT may also occur when the wind speeds increase the opposing jet-stream cores to approximately 60 ms^{-1} (Hopkins, 1977).

In January 1994, a flight between Durban and Cape Town International airports had flown through CAT which left two cabin crew personnel injured (de Villiers and van Heerden, 2001). In another incident in 2014, the Captain of an Airbus A340-300 encountered severe turbulence *en route* to Hong Kong from O.R Tambo International Airport. It was reported that the severe turbulence encounter lasted a few seconds, but it had significant effects including 18 passengers and three cabin crew personnel being injured (Boomgaard, 2014). Interior damage was reported, the oxygen masks close to an exit door had dropped down from the overhead compartment and damage to the onboard baggage overhead panels was reported due to the passenger's heads that had impacted the panels (Naidoo, 2017). The Captain reported that it was CAT at 37 000 ft, and that it could not have been detected by the onboard radar (Boomgaard, 2014). In 2017, passengers onboard a Kulula flight *en route* to Cape Town International Airport experienced CAT. The passengers expressed their experience as traumatic and fearful (Naidoo, 2017).

2.2 Other turbulence types

The following Section describes types of turbulence mechanisms other than clear air turbulence that have a role to play in airmanship and air safety for all pilots.

2.2.1 Wake vortex turbulence

Wake vortex turbulence is not a meteorological phenomenon, but is rather a result of the aircraft's aerodynamics, and is transported by wind flow. Low-pressure develops over the top surface of the wing, and high pressure beneath the wing. This pressure difference leads to a two-counter rotary airflow which tails the aircraft from both wingtips. Wake vortex turbulence attains its strength based on the aircraft size and the shape of the wing. The vortexes are more consistent under stable atmospheric conditions and low aircraft speeds but are short-lived. The decay of this phenomenon occurs when the rotary airflow sinks downward at approximately 300ft to 500ft per minute, or when it reaches the earth's surface (World Meteorology Organization, 2007).

2.2.2 Mountain Waves

Orographic turbulence is generated by means of wind flow over rough terrain and mountainous terrain that may perturb a uniform airflow (World Meteorology Organization, 2007; Beer, 1976). These interactions may cause convection, as well as gravity waves known as mountain waves (World Meteorology Organization, 2007; Turner, 1999). Air circulation that is influenced orographically not only moves around the higher ground but also over the terrain whilst losing buoyancy as the air traverses upward on the lee side (Beer, 1976). This movement of airflow is known as gravity waves. Mountain waves also develop in RSA, generally under stable atmospheric conditions. This results from pre-frontal north-westerly winds over the South African escarpment or due to a Fohan-type air circulation over the interior (Geldenhuys et al., 2019).

Mountain waves may also occur in unstable atmospheric conditions, which are known as untrapped waves. These untrapped waves propagate vertically upwards and may be seen in the stratosphere as orographic cirrus (World Meteorology Organization, 2007).

In regions that lack mountainous features gravity waves may occur during a temperature inversion (Beer, 1976). Gravity waves maintain a continuum when the atmosphere is stable, and when the density gradient is stably restored. The propagating wave may start to collapse in regions where the velocity of the zonal flow is equivalent to the zonal phase velocity. In unstable atmospheric conditions, gravity waves are said to become unstable due to the presence of sheared circulation. This occurs on the lee side of the mountain and may become amplified and develop into a vortex, known as a rotor. Lenticular and rotor clouds are visible indications of mountain waves and cap clouds found on the top of mountains where the air has become saturated (Beer, 1976).

Mountain waves may cause light to fatal damage to aircraft. A light-aircraft had a fatal crash in 2015 in South Africa north of the Tsitsikamma Mountains (Geldenhuys et al., 2019). In Iceland, on 13 October 2016, a High-Altitude Long-Range research aircraft (HALO) encountered severe turbulence between two mountains, Hofsjokull and Langjokull (Wilms, et al., 2020).

2.2.3 Turbulence due to Convection

Convective turbulence originates from the development of *Cumulonimbus clouds* (Cb). There are two classifications of convectively induced turbulence (CIT). The first, in-cloud CIT, develops within clouds by means of strong variational speed updrafts and downdrafts near the anvil cloud feature (Kim and Chun, n.d.; Barber et al., 2018). Secondly, out-of-cloud CIT occurs in a cloud-free region (Kim and Chun, n.d). Out-of-cloud CIT is due to wind shear and gravity waves that form after the cloud top penetrated the tropopause (the region above the troposphere and below the stratosphere). CIT may be more intense during convective deformation than during the mature stage of growth, which causes additional concern to the aviation industry since it may seem that there is no longer a threat from a dissipating Cb (Barber et al., 2018).

Gust fronts develop as a result of evaporative cooling in a downdraft that can be associated with precipitation or no precipitation, which become deflected outwards horizontally near the ground. The gust front is known as the boundary between the cold denser air and the surrounding warmer environmental air that may cause new thunderstorms to develop. The rapidly moving gust front may also be hazardous to aircraft due to abrupt wind direction and speed changes (Martner, 1997). Downdrafts or microbursts are hazardous to aircraft due to the implications of the aircraft’s aerodynamics. The most hazardous time to encounter a downdraft or microburst is when the aircraft is taking off or landing.

2.2.4 Low-level wind shear

Low-level wind shear, also known as mechanical turbulence, is a function of the wind speed, terrain characteristics and stability characteristics of the PBL. Turbulence eddies form in the vertical in unstable conditions which then include wind gusts, therefore increasing the effects of turbulence. Meteorological phenomena that are associated with low-level wind shear are nocturnal low-level jet streams, thunderstorms, and frontal systems, as well as non-meteorological causes such as buildings around and on the aerodrome (World Meteorology Organization, 2007).

Low-level wind shear is associated with sudden changes of wind speed and direction with height. If this is found in the vertical above the runway, it may lead to difficulty in landing or during take-off. The wind may be blowing across the runway and cause the aircraft to turn at an angle, pushing the aircraft's nose to point away from the runway while approaching the runway (World Meteorology Organization, 2007).

2.2.5 Low-level jets

A generalised description of a low-level jet (LLJ) is an elongated zone of maximum wind speed usually greater than 12 ms^{-1} in the lower troposphere, found generally below 700hPa (Hongbo, Mingyang, Bin, et al. 2013), i.e. found between 850hPa and 600hPa as well as below 850hPa (approximately 5000 ft) (Hongbo et al. 2013).

An LLJ develops as a result of diurnal effects that are due to the decoupling and coupling of the surface and PBL. The decoupling and coupling effects cause an inertial sinusoidal swing that generates a wind maximum within the PBL. The LLJ can, therefore, be generated due to the effects of thermal wind over uneven terrain at night. This is produced because of the slight differences in the horizontal temperature gradient which are usually associated with a temperature inversion caused by the decoupling and coupling effects (Oliveira et al., 2018).

Another formation method is due to pressure gradients in the horizontal that is associated with propagating synoptic scale disturbances. These disturbances are linked with a transverse ageostrophic circulation that results from the upper-air jet stream. LLJs associated with the second type of development are usually found just below 10 000 ft (700hPa) (Oliveira et al., 2018).

Synoptic scale disturbances are associated with temperature and vorticity advection, which result in frontal circulation. Fronts are regions generated due to frontogenesis. Frontogenesis is associated with baroclinic waves and tropospheric jet streams. These are known as mid-latitude cyclones, and locally as cold fronts. These weather systems are known to be more intense at the surface due to a more defined temperature gradient (Holton, 2004). Cold fronts are typically linked to the formation of a low-level jet stream, which is found ahead of the surface cold front (Figure 2.4).

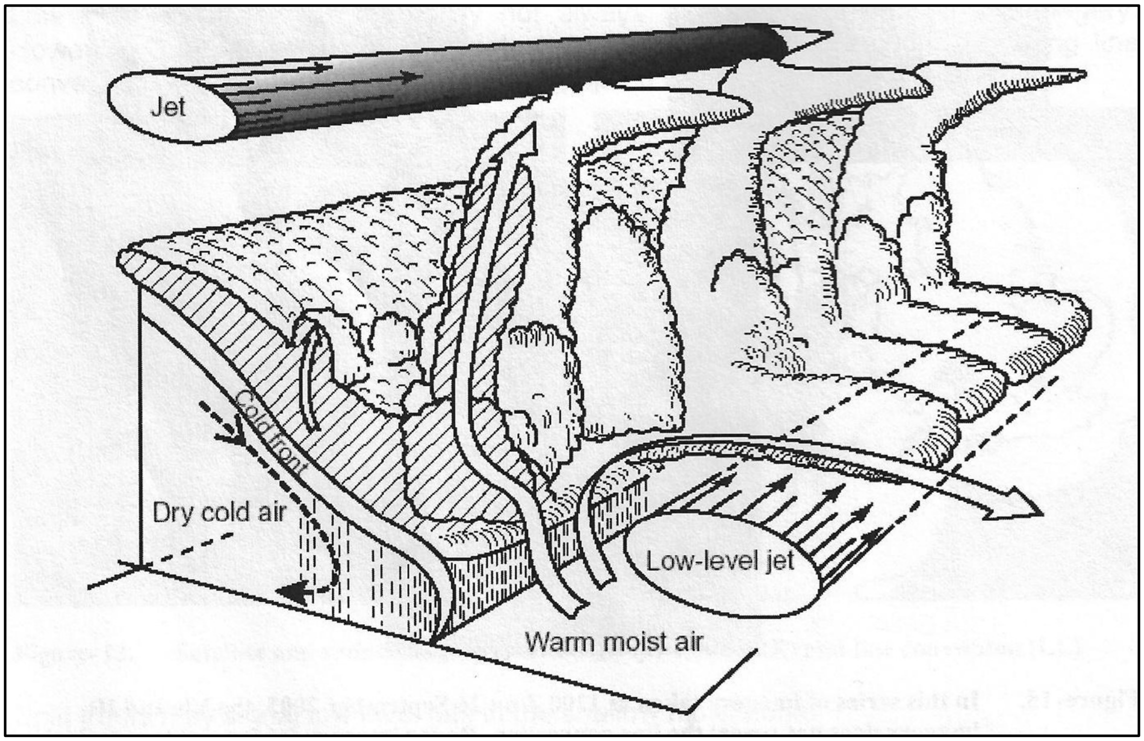

Figure 2.4 Conceptual model of a low-level jet associated with a cold front. As the cold front propagates towards the warm air region, a temperature gradient is generated. The dense dry cold air is pushed below the warm moist air. The colliding air masses may result in wind directional change at the surface ahead of the cold front, thus developing a wind speed increase due to rotary circulation (Adopted from World Meteorology Organization, 2007).

The LLJ that is generated ahead of a cold front can present as a great threat to the aviation industry because at night the wind direction turns and thus shear may occur below or above the aircraft, whereby even gravity waves may develop (World Meteorology Organization, 2007; Balmez and Stefan, 2014). These LLJs (Figure 2.4) can affect take-off and landing procedures, where wind direction and speed fluctuations may result in the increase or decrease of headwinds, causing a sudden increase or decrease of the aircraft's altitude (Balmez and Stefan, 2014).

The six types of turbulence have been discussed including their effects on aircraft. CAT, which is the focus of this study, occurs in the upper levels of the atmosphere. CAT is associated with an upper air jet stream and the dissipation of kinetic energy. The most severe region where CAT is formed is on the cold side of the jet stream. CAT may also develop in the mid- to lower levels of the atmosphere. However, wake turbulence is not a meteorological phenomenon and is not forecasted by the South African Weather Service.

Orographic turbulence occurs often in South Africa due to the mountainous terrain and escarpment along the coastal regions of the country. Mountain waves are dependent upon the stability of the atmosphere that leads to standing waves and rotors which generate below the crest of mountains. This may result in gravity waves propagating horizontally away from the mountain for kilometres, which, in turn, produces turbulence. Turbulence due to convection has been shown to cause gust fronts, which may lead to the redevelopment of thunderstorms. Microbursts are not always associated with precipitation and thus may be dry descending air or be associated with virga. Low-level wind shear and low-level jet streams are mechanically and orographically generated. Low-level shear occurs both in the vertical and the horizontal.

Aviation weather forecasters at SAWS have been forecasting CAT for many years by utilising the Global Forecasting System (GFS) model data output as one of the available tools to forecast CAT. CAT has become of great interest among scientists for many years (Chan and Wong, 2014; Storer et. al., 2019). Many forecasting turbulence indices have been tested and are still being used (Storer et. al., 2019). The following Section will discuss some forecasting techniques and indices that are utilised.

2.3 Forecasting Turbulence

There are a variety of CAT indices and diagnostics available for forecasting CAT. It should be kept in mind that CAT is a micro-scale phenomenon that is being forecast on the basis of having a theoretical connection to mesoscale phenomena. Different scales at play influence the accuracy and skill of the forecast since the forecast is dependent on the statistical accuracy and skill of a high-resolution model in predicting the mesoscale weather pattern responsible for inducing CAT. These predictions of CAT have been done empirically by means of comparing observations of CAT (for example, PIREPs) to synoptic features deterministically. Hence it has been said that CAT remains a difficult weather phenomenon to predict, including the fact that NWP models are not 100% accurate in relaying the actual atmospheric conditions (Hopkins, 1977; Overeem, 2002; Gill and Buchanan, 2014; Sharman, 2018).

A deterministic model (as discussed in Chapter 1) may, for example, indicate uncertainty in the forecast CAT event due to the uncertainty of the forecast position of an upper air jet stream core, which is known to be a significant CAT location indicator. The uncertainty will result in inaccurate upper air jet stream placement and thus also inaccurate CAT regions. Therefore, the position of the CAT event can carry uncertainty and also, potentially, the severity of the CAT event can be uncertain. That could also be due to the excessive energy dissipation from an eddy potential energy transforming to an eddy kinetic energy within the energy budget equation (Hopkins, 1977; Overeem, 2002; Gill and Buchanan, 2014; Sharman, 2018).

An ensemble forecast (Chapter 1) could potentially decrease the uncertainty, by means of forecasting the probability of the jet stream core location over 12 members, which would result in an increase of certainty (Hopkins, 1977; Gill and Buchanan, 2014) towards the forecast of the CAT event location and severity (Hopkins, 1977; Overeem, 2002; Gill and Buchanan, 2014; Sharman, 2018).

2.3.1 Techniques

A case study by Chan and Wong (2014) on severe turbulence encountered over the South China Sea presented a method of utilising quick access recorder (QAR) data, that was available from the flight under investigation. The application of a mesoscale model showed evident turbulence forecasts with 24 to 27 hours lead time. The QAR data also indicated conditions associated with severe turbulence. These conditions included strong downdrafts, high wind shear hazard factor, and an increase in wind speed, as well as high values of eddy dissipation rates (EDR) which were calculated from the QAR data set (Chan and Wong, 2014).

2.3.1.a Turbulence kinetic energy converted into eddy dissipation rate

The eddy dissipation rate is related to the dissipation of kinetic energy. As discussed in Section 2.1, the dissipation rate of kinetic energy is the result of frictional forces that transform the energy into heat after the conversion from potential and internal energy.

$$\frac{\bar{D}(TKE)}{Dt} = MP + BPL + TR + \varepsilon \qquad 2.8$$

The equation 2.8 is the TKE per unit mass, MP is the mechanical production, BPL is the buoyant production or loss, TR designates the redistribution by transport and pressure forces, and ε is describes the frictional dissipation, always positive which reflects the dissipation of the smallest scales of turbulence by molecular viscosity (Holton, 2004). This means that the mean generation of heat into the atmosphere must equate to the average work done by frictional forces (Holopainen, 1962). The concept of available potential energy was introduced by Lorenz (1955), which describes the relation between mechanisms that drive the friction and atmospheric energy cycle.

This close link is considered to describe the horizontal variance of temperature. This means that the available potential energy depicts the horizontal volume/area average of the temperature over the globe, which is recorded along a pressure surface. The thermodynamic equation can be studied to derive the equation that describes the rate of change of available potential energy. The resulting equation represents the rate of generation of available energy due to differential heating. The equation is then utilised to determine the loss of kinetic energy. This is known and described as the eddy dissipation rate (EDR), where $EDR = \varepsilon^{1/3}$ (Holopainen, 1962; Sharman and Pearson, 2017). Therefore, the cube root of the dissipation rate of TKE transformed into heat is equivalent to the EDR (Bechtold et al., 2021).

Chan and Wong (2014) concluded that obtaining QAR data was significantly useful. The increased availability of the QAR data would lead to more informative research conducted on turbulence and would assist in verifying numerical weather prediction (NWP) model output products (Chan and Wong, 2014). The EDR has become an established International Civil Aviation Organisation (ICAO) standard with the units of $m^{2/3}s^{-1}$ (Bechtold et al., 2021). It is a direct measurement of the EDR that provides a range from 0 to 1, where 0 indicates smooth conditions and 1 would be describing very turbulent conditions (Sharman and Pearson, 2017). In this study, therefore, the TKE diagnostic from the convective scale ensemble prediction system (CSEPS) will be converted to the EDR and evaluated as a forecast value instead of a direct measurement for the purposes of this study (Chapter 3). South Africa is a data sparce country and the air space is not as congested as in the northern hemisphere. Nor is it a parameter that is currently forecast over South Africa and EDR measurements from aircraft data is not currently collected or used by the SAWS operationally.

2.3.1.b The Ellrod turbulence index

Other CAT forecasting indices such as the Ellrod index, Turbulence (TB) index and possible short gravity waves diagnostic, as well as the Dutton’s empirical index and the Richardson number, are utilised and have been evaluated. In previous studies, verification was done on the Ellrod index with different NWP models that obtained favourable verification scores. The probability of detection ranged from 70% to 84% and the false-alarm rate ranged between 20% and 40% (Ellrod and Knapp, 1992). The Ellrod index is known to be one of the best performing indices and thus provides value in the aviation forecasting sector (Sharman and Pearson, 2017).

The Ellrod index is the second CAT forecast indicator that will be investigated in this study and is readily available from the CSEPS.

$$Ellrod\ index\ (TI1) = D\left|\frac{\partial\, \vec{v}}{\partial z}\right| \qquad 2.9$$

Where, D denotes the deformation term and $\left|\frac{\partial\, \vec{v}}{\partial z}\right|$ is the vertical wind shear term. The Ellrod index (equation 2.9) (Section 3.3.2.c) shows the relationship between deformation within the horizontal due to stretching and shear processes. Deformation is defined as the kinematic property of a flow, i.e., the ability to transform a volume of fluid or air from smooth to turbulent. Deformation is known to have an important role in producing and destroying temperature gradients, also known as upper-air frontal zones (Overeem, 2002). The tightening of the temperature gradient in the horizontal potentially through deformation strengthens the upper-air frontal zones, and then in turn increases the probability of CAT occurrences (Section 2.2.1) (Overeem, 2002).

Deformation by horizontal shear shows an idealised representation of how wind shear in the horizontal plane contributes to the tightening of the temperature gradient. This occurs when a south-westerly wind causes cold air advection (intrusion) coming into effect by a north-easterly wind that causes warm air advection. The isobars become tilted due to the opposing wind directions and air mass temperatures, resulting in a tightening of the temperature gradient, as explained by Bakker (1992), and cited in the Overeem (2002) tech report, titled: Verification of clear air turbulence forecasts.

Horizontal stretching may also tighten the temperature gradient due to dilatation, i.e., the wind directions differ over the isotherms, assuming a certain horizontal temperature gradient in the same airmass. For example, when a northerly wind direction turns westerly and easterly over the isotherms, then the temperature gradient strengthens where the isotherms become closer together (Overeem, 2002).

Convergence is considered to play an important role in the development of CAT as well. The convergence term is added to the Ellrod index (TI) equation and becomes the second equation (TI2), yet in this study, only T1 is utilised. Convergence is defined as the confluence of streamlines and/or deceleration of air parcels. This process increases the production of frontogenesis. The disturbances that result from frontogenesis may lead to the development of gravity waves, and thus the creation of a Kelvin-Helmholtz instability (Overeem, 2002).

The development of the turbulence index (TB index) was done by the Japan Meteorological Agency (JMP) for the JMP Fukuoka flight information region (FIR) due to that area being prone to turbulence (Kudo, 2011). In the study, Kudo (2011) found that the vertical wind shear index accuracy was similar to that of other indices, e.g. Ellrod indices, Dutton’s empirical index, Richardson number, and the horizontal wind shear index. Kudo (2011) found the accuracy of the different indices of predicting turbulence to be very similar to each other, and therefore the TB index became a combination of multiple turbulence indices.

Haman (1962) has suggested that short gravity waves may be a CAT diagnostic which has also been evaluated by aircraft observations (Sharman et al., 2012). CAT that is induced by short gravity is said to be stimulated periodically by shallow convection. This is related to low-level cumulus convection in an unstable atmosphere and may initiate propagating vertical waves towards the tropopause above the low-level cumulus in the stable layer. The amplitude of the vertically propagating wave also grows greater with height. Thus, the short gravity waves will begin to overturn as they hit a temperature inversion at a higher level or at the tropopause (Kopeć et. al., 2011). Kopeć et. al. (2011) defined the new index as the Wave Braking Density (WBD) index. Even though the WBD index showed favourable results, which was validated utilising a deterministic NWP model with a resolution of 39km, Kopeć et. al. (2011) concluded that more research is needed to determine the skill. It was also suggested that critical levels should be introduced (Kopeć et. al., 2011).

The method of combining multiple indices was also explored by Sharman et al. (2006) and Yamada (2008) which led to an increase in forecasting accuracy, according to Kudo (2011). A study by Storer et al. (2019) cited that Sharman et al. (2006) developed a turbulence forecasting system, called the Graphical Turbulence Guidance (GTG) (Storer et al., 2019). The GTG which is utilised over the United States is a weighted combination of turbulence indices (Kudo, 2011). The GTG was verified by means of utilising several turbulence diagnostics that were evaluated against pilot reports (PIREP). This was done to gain an understanding of the performance of the turbulence diagnostics (Storer et al., 2019). The GTG was proved to be useable and furthermore expressed concern that available deterministic turbulence forecasts may not indicate uncertainty. The GTG verification process reveal that many of the diagnostics in the probabilistic forecast showed evidence of an increase in skill. That was after verification was done against the derived equivalent vertical gust (DEVG) (Storer, et al., 2019). The ensemble forecast was evidently found to be more skilful than a single deterministic forecast (Storer, et al., 2019). The thought was suggested that if a probabilistic forecast could potentially be useful regarding an increase in the understanding of the forecast uncertainty, then this would result in optimum decision making and planning of the pilot’s flight path. Sharman et al. (2006) summarised that the GTG was indeed skilful, but the NWP model that was utilised was found to be coarse, so, to increase accuracy, it was suggested that an NWP model needs to be able to resolve the turbulence scale features (Sharman, et al., 2006).

2.3.2 A forecasting technique over South Africa

Over South Africa, one current forecasting CAT method utilises the Global Forecasting System (GFS). The GFS weather model is produced by the National Centre for Environmental Prediction (NCEP). Data is obtained twice a day at 00h00 UTC and 12h00 UTC with 180 hours lead time, which includes a horizontal resolution of 28 km. Therefore, using NCEP in this study is related to the operational GFS forecasts used in SAWS. The GFS data is displayed in the Personal Computer Gridded Interactive Display and Diagnostic System (PCGRIDS). The CAT forecast is generated and published daily as part of the significant weather (SIG WX) chart by the SAWS aviation weather forecasters. This is published on the South African Aviation website which is the designated aeronautical meteorological authority of South Africa. Significant weather charts are available three hourly, and, four hours before the time of validation.

The forecasting method is based on subjective severity thresholds of wind shear relating to the production of CAT in the vertical column of air, as a guide (World Meteorology Organization, 2007), and is shown in Table 2.2.

Table 2.2: Subjective severity thresholds of wind shear relating to CAT (World Meteorology Organization, 2007).

Wind shear	Moderate	Server
Horizontal shear	20 kt per degree of latitude	30 kt per degree of latitude
Vertical shear	6 kt per 1000 ft	9 kt per 1000 ft

Several studies have concluded that ensemble forecasting (probabilistic) systems are more useful and produce more skilful CAT forecasts (Sharman and Pearson, 2017; Storer et al., 2019). Research has also shown a need for higher resolution NWP model turbulence forecasts due to the complex nature of turbulence (Sharman and Pearson, 2017; Sharman et al., 2006). The SAWS in-house CSEPS has built in diagnostics for turbulence prediction but have not yet been verified to establish skill and usability over South Africa. The two indices that are chosen for this study will be utilised to generate CAT event forecasts to establish the usability of the CAT forecasting maps over South Africa, when comparing them to PIREPs (the aim of the study, Section 1.1). The methodology thereof follows in Chapter 3. The two indices investigated in this study are namely, the (i) Ellrod index and (ii) the dissipation rate of total kinetic energy multiplied to the power of one third (the cube root), which is equivalent to the eddy dissipation rate.

Further research is thus required to establish the usefulness of a higher resolution NWP model turbulence forecasts, as well as the usability thereof over South Africa. This study documents the forecast investigation of the CSEPS CAT indices (listed above) specific for aviation. Such research will potentially increase the confidence in turbulence forecasting over South Africa, and will potentially assist pilots in making safer, as well as more cost-effective and time-efficient, flight plans (Storer et. al., 2019). The next chapter is a detailed description of the data and methodology applied in this study.

Chapter 3 : Data and Methodology

3.1 Introduction

This chapter describes the CSEPS set up, including the resolution, domain and forecast period. The Pilot Reports (PIREPs) are then discussed, followed by detail about the data used to conduct the case studies. The limitation of the data is also detailed. Finally, a detailed discussion follows the Ellrod and EDR indices and the thresholds used to test the CSEPS forecast.

The main data source was observational data from the civil aviation industry of South Africa, PIREPs. PIREPs compiled in 2018 were chosen since that was the most recent complete accident log available for this study. The PIREPs were used to compile a list of 11 case studies. In addition, numerous other meteorological observational data sets were used to describe the atmospheric conditions for each case study. These data sets include satellite imagery from the Meteorology Geostationary Second Generation (MSG) satellite, analysed surface synoptic charts from the SAWSs Climate Service department, and skew-T diagrams from the University of Wyoming online archive as well as upper-air simulations from the National Centres for Environmental Prediction (NCEP).

For each case study, the atmospheric conditions are described, followed by the CSEPS output per location and associated turbulent events (light turbulence (LGTT), moderate turbulence (MDTT) and severe turbulence (SVRT)) were investigated. The investigation was conducted subjectively by comparing the forecast indices to the reported PIREP events.

In this chapter, the methodology applied and the data used are described. The chapter is divided into sub-sections to explain the data used, how the CAT forecasts were obtained, and the forecasts verified. The first sections describe the various observation data sets used to determine the case studies, followed by sections explaining the CSEPS set-up and diagnostic output. The last section provides information on the statistical scores used to verify the probabilistic forecasts and limitations.

3.2 Identification and Analysis of Case Studies

3.2.1 Pilot Reports

PIREPs include reported wind shear or turbulence encountered during a flight and are collected by the air traffic control personnel. Each report describes the location and flight level of the CAT event. The PIREPs were utilised to establish the specific case study dates during the study period of 2018. A total of 226 PIREPs were logged over 87 days, where 11 days (cases) were used in this study. Undoubtedly, this does not imply that these events are the only events, but there could be many cases that may not have been reported or logged. In one day, there was sometimes more than one PIREP captured, and a few PIREPs were at the same time but with different locations and/or heights. The flight levels at which the PIREPs were logged ranged from 26 000 ft to 41 000 ft across South Africa. The majority were reported over the central interior of RSA.

All the months of the year were listed in the database. February, March, and May to November were the months with the most frequent PIREPs logged, ranging from 5 to 8 events. November has most days (22) of PIREPs logged, followed by December and July. MDTT was reported as the most frequently occurring event out of the 226 PIREPs. SVRT was only reported six times. However, the weather associated with the SVRT events was influenced by convective cloud cover, and thundershowers were in the vicinity. Only three out of seven dates were singled out to be severe. The other dates included reports of a combination of MDT-SVR turbulence. Other PIREPs were reported as LGT, MDT or the combination of LGT-MDT turbulence. Events that were reported as LGTT, or MDTT are usually reported more often than the combination. The confidence in reporting a singled-out SVRT event seems to be very low since reporting a combination of turbulence events, namely, MDT-SVR or LGT-MDT are more prevalent. This reporting might indicate a pilot's limited ability to determine the severity of a CAT event objectively. The PIREPs' time was from early in the morning, 04h00 UTC to the evening at 21h00 UTC. It was noted that the LGTT events were more frequently reported in the morning hours and the MDTT events during the afternoon. The SVRT events were logged late morning into the afternoon.

3.2.2 Satellite Imagery

Meteorological Second Generation (MSG) satellite data was downloaded from the European Organisation for the Exploitation of Meteorological Satellites (EUMETSAT) archives.

The MSG satellite scans in real-time every 15 minutes 12 spectral bands (single channels), where 11 have a 3 km resolution. The 12th channel has a 1 km resolution. The single channels are numbered according to the scan sequence and direction (EUMETSAT, 2020).

The raw downloaded data was converted from .tar to .meta to be ingested in SAWS's in-house display tool (SUMO). The MSG satellite images generated for the in-depth case study are the colour composite airmass RGB (red, green and blue channels), Day Natural Color (DNC) RGB, the single-channel water vapour (WV6.2) and the infrared single channel 10.8 (IR10.8). The MSG airmass RGB is a combination MSG satellite image that is composed of the difference between the two water vapour channels (WV6.2 and WV7.3) for the red beam, the difference between the two infrared channels (IR9.7 and IR10.8) for the green beam, and the water vapour channel (WV6.2) for the blue beam. The MSG Airmass RGB distinguishes between warm and cold air masses and identifies dominating weather systems (EUMETrain, 2012).

The airmass RGB was used to identify the signature characteristics of a cut-off low system. The dry stratospheric descending air is identified by animating the imagery to see the reddish-brown colour's rotation into the cloud boundary, which in theory descends into the mid-level of the atmosphere. The cloud boundary appears as "'clumpy' white formation of thick moisture that begins to rotate clockwise, thus a low pressure in the southern hemisphere. The cloud formation is also a characteristic known as the classical 'comma 'shape' (EUMETrain, 2012). The WV6.2 channel is utilised in conjunction with the Airmass RGB to identify the cut-off low system. The WV6.2 channel scans the atmosphere from the top to about mid-level down with a nominal central wavelength of 6.25 μm. The WV6.2 displays the water vapour (grayscale colour) content within the atmosphere. A cut-off low is identified when the WV6.2 image is animated by the dry air seen as a black, rotating clockwise band. That illustrates a low pressure in the upper air, which is cut off from the main westerly upper airflow. The MSG DNC RGB is a true colour image and is a combination of the near-infrared band (NIR1.6) and two visible bands (VIS0.8 and VIS0.6). The MSG DNC RGB is utilised to identify cloud types, such as convective clouds that appear bright and clumpy, with white colour. Thin high-level clouds such as *cirrus* clouds are also seen as a thin, dark cyan colour, which is ice. It is used to distinguish between ocean and landmass, where the ocean is a black colour and the land a brown colour, whereas vegetation is seen via a green colour. It is used within this study to indicate if the PIREP location is within a cloud-free region. The IR10.8 single channel is utilised as well to indicate cloud-free regions of the late afternoon and evening hour PIREPs since the MSG DNC RGB uses sunlight and the IR10.8 uses temperature to distinguish between features such as land and cloud when the sun has passed over RSA (EUMETrain, 2012).

3.2.3 Skew-t Diagrams

The archived skew-ts were obtained from the University of Wyoming website (www.weather.uwyo.edu). The line on the right of the skew-t diagram (Figure 4.3) illustrates the air temperature from the surface to the maximum height of the radiosonde ascend. The line on the left of the vertical is the corresponding dew point temperature. The wind speed (kt; knots) and direction are indicated on the extreme right of each diagram. For example, the short line on the wind barb indicates 5 kt, a full line 10 kt, and a triangle equals 50 kt.

Skew-ts were used to establish the height of the upper air jet stream core and tropopause and if there was possible wind shear near the upper air jet stream and tropopause. This analysis confirms if the atmosphere was conducive to turbulence near the jet stream and tropopause.

3.2.4 Surface Synoptic Charts

The synoptic overview, which follows after the pilot report description, is described using the SAWSs analysed synoptic chart (Figure 4.2). The synoptic chart indicates the surface flow and current weather conditions based on synoptic stations. Additional information is cloud cover, which is essential for this study and current instability by reporting the type of clouds.

3.2.5 NCEP Reanalysis Data

Model output images were obtained directly from the Physical Science Laboratory website (http://psl.noaa.gov). The images are based on the NCEP FNL (final) operational model global tropospheric analysis data (National Centers for Environmental Prediction, 2020). The parameters required are daily average geopotential heights (gpm) at 250hPa (Figure 4.2a) and daily average wind speed at 250hPa (Figure 4.2b). The daily average geopotential heights in meters above sea level at 250hPa are illustrated by the rainbow colour scale at the bottom of the image (Figure 4.4). The wind speed is illustrated by the rainbow colour scale at the bottom of the image, where the maximum windspeed indicates the location of a jet stream core (Figure 4.2).

3.2.6 Identification of Case Studies

The 11 case studies utilised in this thesis are cases from the PIREP data base's 2018 summer and winter months (discussed in Section 3.2.1). Cases were selected in the summer (Oct-Mar) and winter (Apr-Sep) seasons to include the weather systems favourable for inducing CAT (Section 2.1.2). There were 134 PIREPs cases in summer and 92 in winter. The synoptic circulation patterns on each day that a PIREP was reported were investigated and three main weather patterns emerged: the COLs, upper air troughs and zonal upper airflow.

The decision on the choice of the dates for the case studies was based on;

- the number of PIREPs on any particular day (33 in total for this study).
- conformation that no convective cloud and thunderstorms were in the vicinity of the PIREP.

Only LGTT and MDTT PIREP reports were available for analysis as SVRT were only reported in the presence of convective cloud. The case study dates that met the conditions mentioned above are tabulated in Table 3.1, which also includes the number of PIREPs logged (total of 33) on the day (11 case studies) and the associated CAT severity (total of 39 events).

Table 3.1: The case study event dates for the year 2018 utilised for this study and listed according to the weather pattern categories, amount of PIREPs logged and associated turbulence severity, where light turbulence = LGTT, moderate turbulence = MDTT and severe turbulence = SVRT.

Weather Category	Date (2018)	Amount of PIREPs	Event severity
COL			
	16 July	3	2 LGTT & 2 MDTT
	20 May	1	LGTT
	09 August	1	LGTT-MDTT
	03 September	1	MDTT
Trough			
	03 May	8	2 LGTT & 6 MDTT
	21 May	5	3 LGTT & 2 LGTT-MDTT
	03 October	2	1 MDTT & 1 LGT-MDT
	05 November	3	1 LGTT & 2 MDTT
	09 December	5	4 LGTT & 1 MDTT
Zonal flow			
	10 June	3	3 MDTT
	18 November	1	1 LGTT

Source: PIREP data

The first case study in Table 3.1 is discussed in-depth in Section 4.1. The events on 16 July 2018 are associated with a cut-off low. This particular day also had the reported locations of the CAT within theoretical significant prone CAT regions. These regions are known to be influenced by CAT generation with the cut-off low and the upper air jet stream mechanisms. The case also had a total of 4 pilot reports that logged light, moderate and light to moderate turbulence. That made 16 July 2018 a good case study for this research approach since the case demonstrates how a specific weather phenomenon is identified, analysed and forecasted while applying theory. The meteorological details for the in-depth case study include the above-mentioned observational data. The first data investigated is the PIREP summary, which describes the location and flight level of the logged CAT event. This step was followed by the synoptic overview (Section 4.2.1), which also describes upper-air circulation based on the NCEP operational forecast data and the skew-t charts. The satellite imagery is then displayed and discussed. The combination of the observational data assisted in identifying the weather system and whether the PIREPs were within cloud-free regions.

After the background of the event day is discussed, the CSEPS model outcome at each location of the PIREPs in-depth case study follows.

The two indices values are displayed as the ensemble average and the ensemble probability for every flight level and 5-hourly interval. The individual ensemble member values of both indices were first calculated to see if there were any negative values. The Ellrod index values 'can't have a negative value due to the index formulation (Section 3.3.2.a). No negative values were found within the Ellrod index calculations. However, the Ellrod index values were very small and were multiplied by 1×10^7 (Overeen, 2002). However, some members were negative within the EDR index calculations and were therefore omitted from further calculations. The EDR index values were calculated by modifying the TKE value by the multiplication to the power of one-third, which resulted in the measured units of $m^{2/3}s^{-1}$. The ensemble average for both indices were calculated for the entire grid at the level and time interval of interest and divided by 12 (ensemble members). The indices values of the ensemble average were then tabulated and discussed. The ensemble probability was displayed and discussed along with the ensemble meteogram for both indices. The meteogram summarised the ensemble probability of an event to occur compared to the ensemble average, highlighting the ensemble's usability. The ensemble meteogram was utilised to determine the ensemble spread for each predictand, which shows the forecast uncertainty and tendency towards the threshold.

After the in-depth case study, the rest of the case study dates (11) are tabulated (Table 4.4-6) according to the three weather categories and is investigated in a similar method as the in-depth case study. Table 4.4-6 lists the dates under each weather category and the rest of the PIREP information in columns 2 to 5, and the CSEPS model output from columns 6 to 8. The PIREP information lists the pilot reported event time, the location (waypoint), the height (hPa/ft) of the event, and the event severity under the observation column. After that the CSEPS model output indicates both indices' ensemble average forecast. The columns list the ensemble probability (0-100%) of the event and severity (LGT, MDT, or SVR), followed by the event forecast level (height) for both indices ensemble probability forecast. The last three columns list the CSEPS model output and are highlighted to indicate the model evaluation results. Values highlighted in grey indicate a 'hit'. A 'hit' is assigned when the forecast matches the observation, where the time, location, level, and severity coincide. The values associated with an upward pointing arrow indicate a severity predicted higher than what was observed. The downward pointing arrow is when the forecast severity was too low. The 'high' indicates that the ensemble probability forecast was at a higher model level than the observation. Whereas the 'low' shows that the forecast was at a lower level. The observations, at times, are a combination of LGTT and MDTT, so in Table 4.4-6, the model output is listed for both events under the two last columns for both predictands, respectively. If the forecast is correct (hit) for at least one of the severity combinations, that PIREP is considered a hit. Each Table is discussed, followed by an overall discussion in Chapter 5. This data analysis of the 39 observations indicates how often the CSEPS forecast overestimated or underestimated the CAT events for the ensemble average and ensemble probability forecast. It will shed light on the uncertainty of the model and how well the CSEPS resolves the actual event associated with the weather category.

3.3 Numerical Weather Prediction Data

3.3.1 Convective Scale Ensemble Prediction System

The CSEPS is run in-house at SAWS and was used for the forecast simulations in this study. The CSEPS has a 500 x 450 grid points domain, with a 4.5 km horizontal grid resolution covering the South African (Figure 3.1). It has a lead time of 48 hours and is initialised twice daily at 12h00 UTC and 21h00 UTC. The 21h00 UTC run was utilised for this study to obtain maximum model performance (shortest lead time to the events while still considering regional model spin-up). That is consider the model data output to be the most reliable within the first 48 hours of the forecast and to minimise model spin-up display issues.

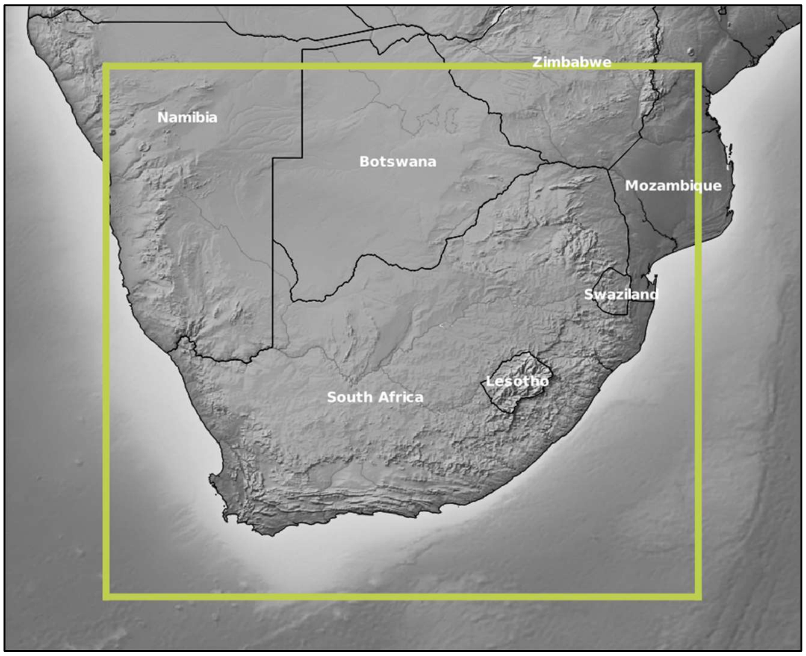

Figure 3.1: Domain coverage of the CSEPS runs indicated in yellow.

The SAWS operational CSEPS has 18 members. However, for the research simulations in 2018, the ensemble consisted of only 12 members due to the availability of the global ensemble members for driving data. The initial- and lateral boundary conditions were received from the United Kingdom's Meteorological Office's Global and Regional Ensemble Prediction System (MOGREPS) output. MOGREPS has a three-level cascade configuration of which one is a global model (MOGREPS-G). The MOGREPS-G has a 60 km horizontal grid resolution that utilises initial conditions from the four-dimensional variation data assimilation system and the local ensemble transform Kalman filter perturbation technique for initial perturbations (Golding et al., 2016).

Two forecast indices specific for CAT from the CSEPS were considered for this study, namely, the (i) Ellrod index (Turbulent Index, (TI)) and the dissipation rate of (ii) total kinetic energy converted to the EDR (Section 2.2.1). The mountain wave turbulence index is another available index, along with the Richardson number index, the diagnosed turbulent dissipation rate, dissipation from convection, and dissipation from the SMAG (Smagorinsky) model. These indices were not considered based firstly on the fact that the index needs to be for CAT and not convection related, and this study is for the upper air, from 18 000 ft up. Therefore, the mountain turbulence was not considered. The other indices are parameters that have been evaluated before. The EDR, as described in Chapter 2, was calculated by taking the cube root of the TKE output. The other parameters utilised in this study are the u and v wind components for calculating the vector winds. For each index, a 24-hourly forecast were generated on 52 model levels for all 12 ensemble members. For this research, the case study model data was then displayed specific for each case study built around each PIREP for a temporal resolution of 5 hours. The time interval was therefore inclusive of the case study event time. The model levels were used to run the EDR index, and model pressure levels were used for the Ellrod index. As explained in the case study section (3.3), the model level and pressure levels were converted to feet (ft) above mean sea level (AMSL) to correspond to the nearest flight level reported in the PIREP. The two CAT indices are explained in detail in the following sub-section.

3.3.2 Predictands:

a) Ellrod Index, TI

The Turbulent Index, referred to as the Ellrod Index in this dissertation, describes the atmosphere's horizontal deformation and vertical wind shear (Ellrod and Knapp, 1992). The stretching- (DST; eq. 3.1) and shearing-deformation (DSH; eq. 3.2) have components that are derived from the u and v wind components (Ellrod and Knapp, 1992; Overeem, 2002). Deformation refers to the 'deformation 'zones' evident near cloud boundaries where significant CAT develops. These regions are associated with a hyperbolic flow that occurs within COLs and the exit region of a jet stream (Section 2.1.2) but do not consider the mountain-wave or turbulence induced by thunderstorms (Ellrod and Knapp, 1992; Overeem, 2002). The DST equation calculated CAT zones well but indicated vast threat regions and proved difficult to interpret due to significant positive and negative maxima values (Ellrod and Knapp, 1992).

$$DST = \frac{\partial u}{\partial x} - \frac{\partial v}{\partial y} \qquad 3.1$$

$$DSH = \frac{\partial v}{\partial x} + \frac{\partial u}{\partial y} \qquad 3.2$$

Therefore, the DST and DSH eliminated the negative values and reduced the threat region (Ellrod and Knapp, 1992). The combination then became the resultant deformation (DEF), or the total deformation (D; eq. 3.3) (Ellrod and Knapp, 1992, Overeem, 2002),

$$DEF = D = \frac{(DST^2+DSH^2)}{2}\left|\frac{\partial \vec{v}}{\partial z}\right| \qquad 3.3$$

Where is $\left|\frac{\partial \vec{v}}{\partial z}\right|$ vertical wind shear. Overeem (2002) further derived the Ellrod Index equation by looking at the approximate thermal wind relationship given by:

$$\frac{\partial T}{\partial y} = -\frac{f_c T}{g}\frac{\partial U_g}{\partial z} \qquad 3.4$$

$$\frac{\partial T}{\partial x} = +\frac{f_c T}{g}\frac{\partial V_g}{\partial z} \qquad 3.5$$

Where, T (K), f_c, g, U_g, V_g, is temperature, Coriolis parameter (s^{-1}), acceleration of gravity ($m.s^{-2}$), u-component of geostrophic wind ($m.s^{-2}$), and v-component of geostrophic wind ($m.s^{-2}$) respectively (Stull, 1988).

The temperature gradient magnitude is given by:

$$|\nabla T| = \left(\left(\frac{\partial T}{\partial x}\right)^2 + \left(\frac{\partial T}{\partial y}\right)^2\right)^{0.5} = \left(\frac{f_c^2 T^2}{g^2}\left(\left(\frac{\partial U_g}{\partial z}\right)^2 + \left(\frac{\partial V_g}{\partial z}\right)^2\right)\right)^{0.5} = \frac{f_c T}{g}\,|VWS| \qquad 3.6$$

where,

$VWS = \frac{(\Delta u^2 + \Delta v^2)^{1/2}}{\Delta z}$ is vertical wind shear. 3.7

It is further assumed that the geostrophic wind is equal to the horizontal wind and frontogenesis takes place over a constant pressure level, as well as $|\nabla \theta| = |\nabla T|$, where θ denotes the potential temperature. These assumptions may cause an overestimation of the CAT values, according to Overeem (2002).

The equation 3.3 (DEF) is then combined with vertical wind shear due to a strong correlation between the forecast locations of both parameters separately and the significant CAT occurrences (Ellrod and Knapp, 1992; Overeem, 2002). The Ellrod index has the units of $10^{-7}s^{-2}$ and then described as,

$$TI = D|VWS| \qquad 3.8$$

The product of TI is double that of vertical wind shear (VWS) alone (Ellrod and Knapp, 1992). Convergence is known to potentially contribute significantly to the generation of CAT from wind fields aloft, hence the addition of a new term to the equation, called convergence (C_{vg}), but not considered for this purpose (Ellrod and Knapp, 1992).

All the terms comprising the TI equation are kinematic, therefore, they do not consider the pressure forces (Ellrod and Knapp, 1992). The values resulting from TI range from 0 to 12, where the values of 8 to 12 indicate a high probability of severe CAT occurring. For this study, values of greater than 12 were obtained; therefore, >8 will be investigated (Ellrod and Knapp, 1992). The thresholds for TI are tabulated in Table 3.2 and are considered for this study. For this study, it will be compared to the forecast values of the TI forecast values by the CSEPS, which is now further denoted as the 'Ellrod' 'Index'.

Table 3.2: The Ellrod index thresholds for each turbulence event utilised in this study as adopted from Ellrod and Knapp (1992).

Turbulence intensity measured in s^{-2}	Value range
Light (LGT)	2 – 4
Moderate (MDT)	4 - 8
Severe (SVR)	>8

b) Turbulent Kinetic Energy Index

In the atmospheric energy flow, differential heating, potential energy, and internal energy are generated that is converted into kinetic energy, so when subjected to friction, dissipation will occur. A previous study found that large kinetic energy losses are evident in the lower boundary layer and significant energy losses near the tropopause (Holopainen, 1962). The kinetic energy dissipation rate (also known as the mean intensity of the atmospheric energy cycle) is the net transformation of kinetic energy into eddy energy inside a column of air due to friction, denoted by D, where, $W_F = D$ and,

$$W_F = V.F(\frac{\Delta p}{g}) \qquad 3.9$$

W_F is the loss of kinetic energy because of frictional forces resulting from changes in the vertical component of the eddy stress that is averaged over a region of interest. V

is the mean wind speed and $\frac{\Delta p}{g}$ is the variation of pressure. Where, F is the eddy stress term,

$F = \frac{1}{\varrho}\frac{\partial \tau_z}{\partial z}$, and where ϱ is the nonadiabatic heating 3.10

and,

$$\tau_z = \varrho K \frac{\partial V}{\partial z}, \tag{3.11}$$

where K is the coefficient of eddy viscosity. K is known to decrease with increasing static stability.

After integration by parts equation 3.11 W_F becomes equation 3.12;

$$W_F = [V \cdot \tau_z]_{z_2}^{z_1} - \int_{z_2}^{z_1} \tau_z \cdot \frac{\partial V}{\partial z} dz \tag{3.12}$$

For the first kilometre of the atmosphere from the surface W_F becomes equation 3.13,

$$W_F(0 - 1000m) = \int_0^{1000} V \cdot \nabla p dz = f V_g M_y \tag{3.13}$$

Where, V_g denotes the speed obtained from the geostrophic wind and M_y is the integration cross isobaric mass transport, which equates to $M_y = (\tau_{x,0} - \tau_{x,1000})/f$. The assumption is then made that the eddy viscosity (K) at 1000 meters could approximately be $1.0 \times 10^5 cm^2$ and from $V_g \tau_{x,1000} = 0.3\, watts\, m^{-1}$. A contributing error of about 10% was found, and therefore, it was concluded that the term $\tau_{x,1000}$ could be neglected. Leading to the equation of 3.14,

$$W_F = V_g(\tau_{x,0} - \tau_{x,1000}) \tag{3.14}$$

The results of the study done by Holopainen (1962) concluded that the mean kinetic energy dissipation rate from the surface to 200hPa is approximately $10\, watts\, m^{-2}$. Where $4\, watts\, m^{-2}$ of the $10\, watts\, m^{-2}$ was evident from the surface to 900 hPa and $6\, watts\, m^{-2}$ the mid-atmosphere, between 900 hPa to 200 hPa (Holopainen, 1962). It is also found in Holopainen's study that the dissipation is constant for geostrophic wind speeds, which is less than $12\, m.s^{-2}$. Above the values of $12\, m.s^{-2}$ the dissipation rate increases due to an increase in wind speed (Holopainen, 1962).

TKE dissipation rate forecast values from the CSEPS initial data 21h00 UTC run were converted to EDR values by calculating the cube root for each TKE value (Section 2.3.1.a) for each grid point for all 12 ensemble members and has the units of $m^{2/3}s^{-1}$

(Bechtold et al., 2021). It is a direct measurement that ranges from 0 to 1, and the associated turbulence event is tabulated in table 3.3 as utilised in this study (Sharman and Pearson, 2017; ICAO, 2018).

Table 3.3: The EDR thresholds for each turbulence event utilised in this study as adopted from ICAO (2018).

Turbulence intensity measured in $\boldsymbol{m^{2/3}s^{-1}}$	Value range
Light (LGT)	0.1
Moderate (MDT)	0.4 – 0.7
Severe (SVR)	> 0.7

The data and methodology have been described. The following chapter is the compilation of all the case studies investigated to evaluate the two predictands' CSEPS model output. This thesis will end with Chapters 5 and 6, followed by the limitations and recommendations and future work of this research. This will enable the determination of the aim of the thesis to say whether or not the predictands are helpful as potential CAT indices over South Africa, specifically for Aviation.

Chapter 4 : Case Study

4.1 Introduction

Eleven case studies were identified and are discussed in this chapter. The first case study is discussed in detail in Section 4.2 while the other case studies are summarised in the succeeding Section 4.3. The case study discussions in this Section comprise of an analysis of the event forecasts and a comparison with the PIREPs for each weather category. The case studies serve to determine if the ensemble average and probabilistic forecast of the Ellrod and EDR indices, available from the CSEPS, are capable of predicting CAT over RSA (The aim of this dissertation). The first objective of this dissertation was to identify thresholds for the Ellrod and EDR indices from literature. A comparison of the ensemble average and probabilistic forecast values from the individual ensemble members to the known CAT events followed. That led to the confidence of utilising the thresholds since the forecast values fell within the similar values of the thresholds (Section 3.2.6). This was from the collection of the observational data and the index thresholds from past literature. The weather systems which occurred most frequently on days with PIREPs (Section 3.2.1) were (1) COL, (2) upper air trough, and (3) zonal flow (Section 3.2.6).

The first case study, presented in detail in Section 4.2. is the 16 July 2018 Cut-off low. The other case studies are presented in Section 4.3. For each case study a synoptic discussion is provided first, the PIREPs are analysed to locate the time, position, and intensity of the turbulent event. Finally, the CSEPS CAT forecasts of the ensemble average and ensemble probability are compared to the PIREPs in order to determine if there is any accuracy and therefore accomplishing objective two of this research (Section 1.1). The performance of the CSEPS model will be assessed with respect to

- the severity of the turbulence
- the location of the turbulence
- the time of turbulence
- the level at which the turbulence occurred.

4.2 Cut-off Low - 16 July 2018

The 16 July 2018 was identified as a COL weather system that occurred (Section 2.1.1). CAT regions that are associated with COLs occur between 500 and 200hPa. The first jet stream develops around the COL and the other jet to the south that remains part of the westly flow and CAT may occur in the confluence areas between the two jet streams (Figure 2.3 3). CAT also happens in the 'neck' of the low pressure that is cut-off from the westerly flow and to east of the cut-off low pressure (Figure 2.3 4). Another area prone to CAT relative to the COL is the region away from a possible shear zone that induces inertia-gravity waves, as well as near the subtropical jet stream (Venkatesh and Mathew, 2013) (Section 2.2.1). In this case study it will be shown that CAT occurred east of the COL over the western parts of the country, relative to the waypoint KYV. CAT also occurred near the subtropical jet stream near the waypoint BEBAS, which is on the cold side of the jet stream core. The waypoint EGNOM had mid-level clouds beneath the CAT occurrence height in the morning and in proximity of convective clouds and therefore the turbulence that was reported could not be classified as CAT and omitted from the case study discussion (Section 2.1.1).

The PIREPs for the 16th July 2018 indicated LGTT, MDTT, and LGT-MDT turbulent events (Table 4.1). The CAT events had been experienced at flight levels, 225hPa/FL360 and FL370 (which is close to 225hPa/FL360 model hights), and 300hPa/FL300, at the waypoint KYV (2 on Figure 4.1) and BEBAS (3 on Figure 4.1) found in the Northern Cape and KwaZulu-Natal provinces respectively.

Table 4.1: PIREP of turbulence reported at three locations on 16 July 2018. LGT=light, MDT=moderate. The flight level is indicated by FL and the pressure level closest to the flight level in the CSEPS data are included in hPa.

Location	Time	Level/Flight Level	CAT Event
EGNOM	08h32	225hPa/FL360	LGT-MDT (not CAT)
KYV	08h44	225hPa/FL360 (FL370)	LGT-MDT
KYV	16h10	225hPa/FL360	LGT
BEBAS	14h27	300hPa/FL300	MDT

Source: PIREP data

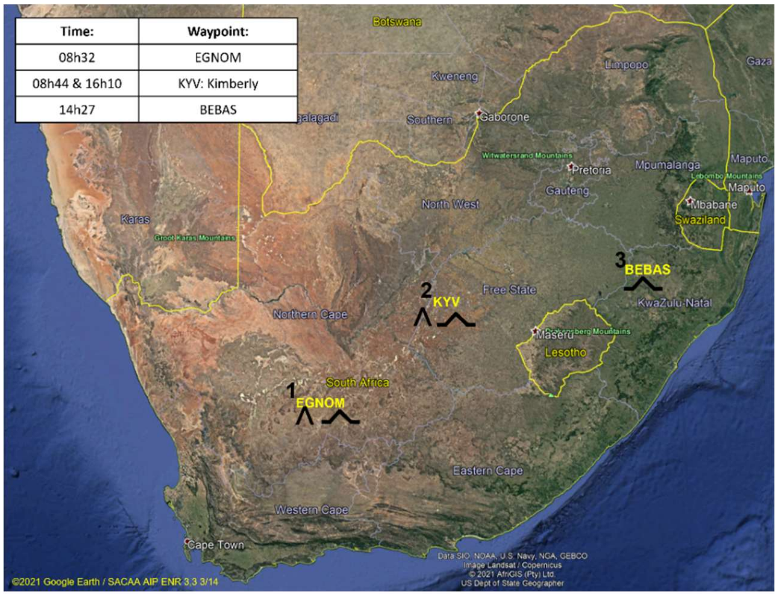

Time:	Waypoint:
08h32	EGNOM
08h44 & 16h10	KYV: Kimberly
14h27	BEBAS

Figure 4.1: The way points where turbulence was recorded on 16 July 2018 (yellow). The black symbols indicate light (^) and moderate (⌒) clear air turbulence (Google Earth, 2020 & SACAA AIP ENR 3.3 3/14, 2020)

4.2.1 Synoptic overview

In the upper air, at 250hPa/FL340, a COL is evident west of the country (enclosed dark purple contour) (Figure 4.2, left). The green to yellow shaded region shows the strongest winds speeds (Figure 4.2, right). Kock et al. (2006) postulated that wind strengths of > 30 ms^{-1} are commonly used to identify a jet stream core (Section 2.1). The winds speeds predicted at the core of the jet stream are between 60 and 70 ms^{-1} (grey to dark grey shaded region) on Figure 4.2, and 50 to 60 ms^{-1} over RSA. The strong winds over the north-eastern parts of RSA, therefore, represents the jet stream core position at 250hPa/FL340 (Figure 4.2 the dark shaded region overlayed with strong wind speeds, the long arrows). The jet stream core is in a similar position to where the generally cloud free region is found (Figure 4.3). Transverse *Cirrus* cloud band or 'scallops' are visible to the north-east of the strongest winds (Figure 4.2 & 4.3). That is indicative of a jet stream that is often associated with MDTT on the warm edge (towards the equator) and on the cold side of the subtropical jet stream (Overeem, 2002) (Figure 4.2 in the region of BEBAS) (Section 2.1.6).

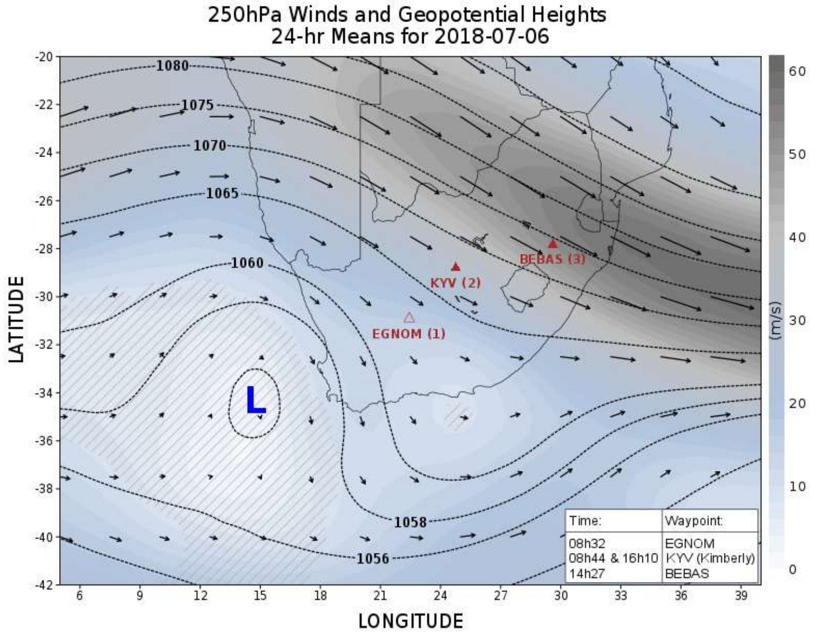

Figure 4.2: The 24hr mean geopotential heights in meters (thin black lines) overlayed by the wind speed in ms^{-1} (grey scale on the right) and zonal isotachs as shading (the arrows) at 250hPa/FL340 from the NCEP-DOE Reanalysis 2 (R2) https://psl.noaa.gov/data/gridded/data.ncep.reanalysis2.html.

In the figure 4.2 it is indicated that the position of the low pressure is slightly placed south from where it is seen on the satellite imagery, in figures 4.5. At the surface, Figure 4.3 shows light (5-10 kt, as classified by the Beaufort Wind scale) north-easterly winds over the central parts are observed as well as generally cloud free conditions over eastern South Africa at 12h00 UTC (also see Figure. 4.5). The upper air sounding of Upington (FAUP), Northern Cape province, taken at 00h00 UTC (Figure 4.4, left), and taken at 12h00 UTC at the Bloemfontein Airport (FABL) (Figure 4.4, right), are the nearest available soundings to the observations of the morning and afternoon PIREPs (Table 4.1). Unfortunately, the Upington skew-t in the morning has thick clouds from the surface extending until 300hPa and is in the proximity of convective clouds and therefore omitted from the case study discussion. It is also noted that there is no available skew-t diagram close to the third waypoint BEBAS on 16 July 2018.

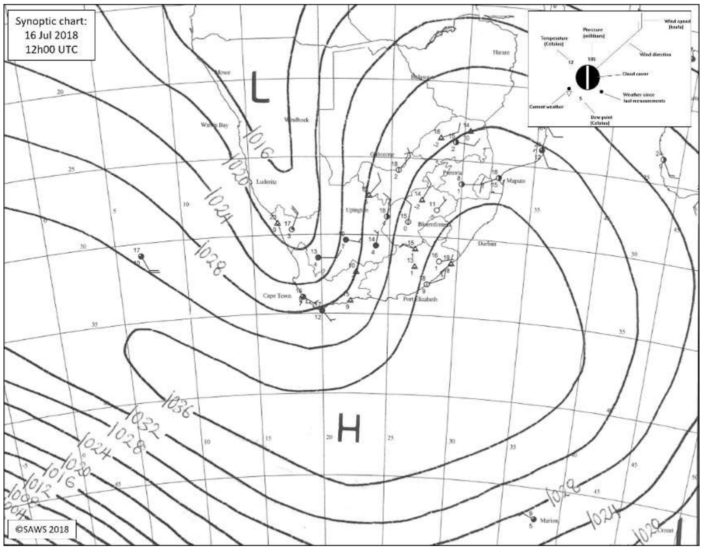

Figure 4.3: The surface synoptic chart on 16 July 2018 valid at 12h00 UT. A surface tough was over the western parts of country and the low pressure over Namibia (marked by the bold 'L'). The South Atlantic high pressure (marked by the bold 'H') was located to the south of the country (SAWS, 2018).

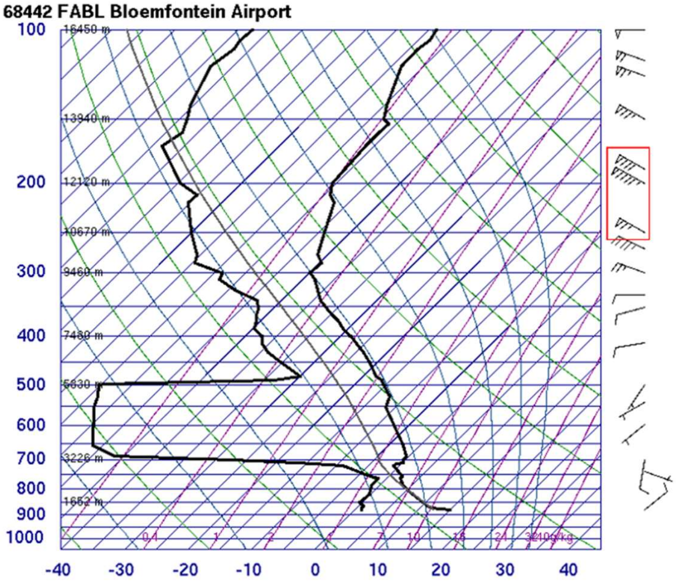

Figure 4.4 The skew-t diagram at Bloemfontein Airport at 12h00 UT. The air temperature is represented by the black line on the right of each graph and the dew point temperature is the black line on the left. Wind strength, indicated in knots, and direction are indicated on the extreme right column of each graph. The short line on the wind barb indicates 5 kt, a full line is equal to 10 kt and a triangle equals 50 kt. The diagram was obtained from the University of Wyoming (www.weather.uwyo.edu) but was done by the South African Weather Service.

At FABL 12h00 UTC between 250hPa/FL340 and 175hPa/FL410 (indicated by the red rectangle on figure 4.4) an increase in wind speed (65 kt to 95 kt) is evident and then a decrease again (95 kt to 80 kt) at 175hPa/FL410 and thus a jet stream core can be noted at 200hPa/FL390. A stable lapse rate is found between 220hPa/FL370 and 200hPa/FL390 and lower into the atmosphere between 350hPa/FL270 and 325hPa/FL280, which is indicative of potential CAT layers above and below those layers at 12h00 UTC. The FABL skew-t also indicates that the atmosphere is stable ahead of the COL, since the type of cloud is stratiform and found in the lower mid-level of the column of air (the skew-t dries out rapidly with height from 700 to 500hPa and below 800hPa) (Figure 4.4).

Figure 4.5 (left) illustrates the formation of a cut-off low pressure at 09h00 UTC based on the signature 'comma' cloud seen over the western parts of RSA and the dry air rotation is seen after the image is animated, on the MSG water vapor (WV06.2) channel (Section 3.2.2). The upper air low pressure is cut-off from the main westerly upper air flow indicated by the bold black 'L'. There is evidence of rotation of high potential vorticity around the 'comma' cloud which is another COL characteristic used for identification of a COL, as seen on the MSG Airmass RGB (Section 3.2.2) at 09h00 UTC (Figure 4.5 right).

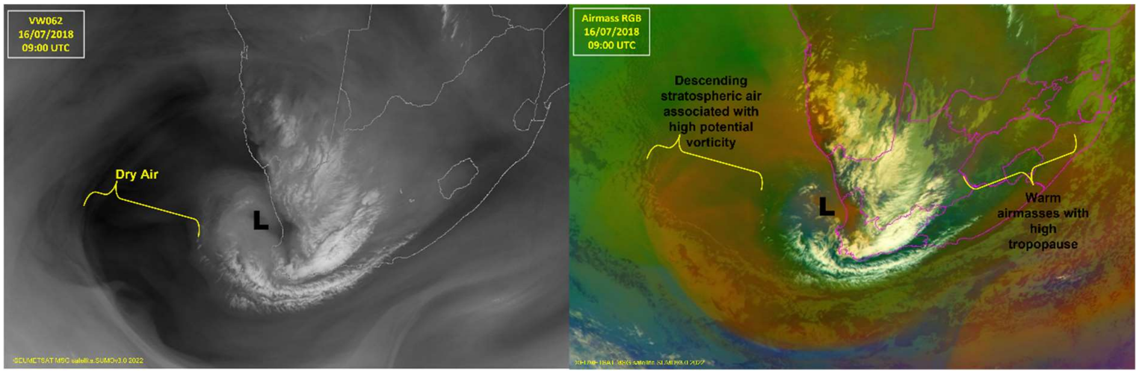

Figure 4.5: MSG WV062 channel (left) and Airmass (right) RGB of 16 July 2018 at 09h00 UT. A cut-off low is indicated to the west of the country and the low-pressure centre by the bold black 'L' (left).On the WV06 image dry mid and upper level air is indicated by the black shades, west of the low and on the airmass RGB the dry descending air from the stratosphere is indicated by the light brown shades. Copyright (2020) EUMETSAT.

At 09h00 EGNOM had been underneath *Altocumulus (AC)* cloud. The *AC* cloud band spreads to the northwest and western parts of EGNOM. Moreover there is convective cloud and cirrus cloud around EGNOM. The convective cloud is visible on Figure 4.6 by looking at the thick clumpy cellular white color clouds to the west of the waypoint, EGNOM (first yellow star on Figure 4.6). The cyan color are cloud tops that are high enough to contain ice particles, such as cirrus and anvils of convective clouds (Figure 4.6 left). The cirrus is also seen on the IR10.8 single channel, illustrated by the cold cloud top temperatures in light blue (Figure 4.6 right). This further illustrates that EGNOM was not situated in clear air and the turbulence reported by the PIREP was therefore not CAT and therefore not included in this analysis.

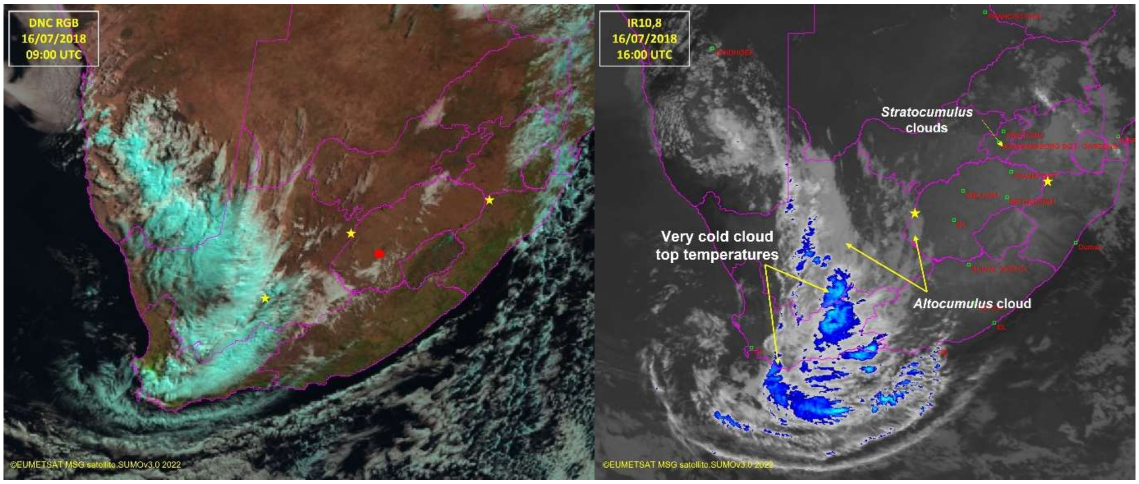

Figure 4.6: MSG DNC RGB (left) and IR10.8 single channel (right) of 16 July 2018 at 09h00 UT and 16h00 UT, respectively. The yellow stars indicate the locations of all three waypoints, from left to right it is EGNOM, KYV and then BEBAS. The red dots indicate the location of the two skew-t diagrams, FAUP (left) and FABL (right).The very cold cloud top temperatures over South Africa on the IR10.8 image is indicative of convective cloud. Copyright (2020) EUMETSAT

The waypoint, KYV at 09h00 UTC is clear of cloud (Figure 4.6 left) but by the afternoon, (16h10 UTC) the *AC* cloud band had reached KYV (Figure 4.6 right). The *AC* cloud tops are approximately at 17 500 ft (the cloud top temperature is approximately 12 °C taken from the IR10.8, which is around 515hPa on Figure 4.4) and the CAT event took place at 30 000 ft (300hPa/FL300) which is 12 500 ft above the *AC* cloud tops and can be considered that the CAT event took place free of cloud. The third waypoint, BEBAS, is to the west of the *stratocumulus* clouds as seen of the MSG DNC RGB (Figure 4.6, left) at 09h00 UTC and these clouds did not invade the area by the time of the PIREP (Fig 4.6 right). It is also important to note that *stratocumulus* cloud is a low level cloud which occurs close to the surface and will therefore not influence the occurrence of CAT.

The dominant weather pattern on 16 July 2018 is a COL, which is first weather category (Section 3.2.6). The aforementioned information provides confirmation that the atmosphere was conducive of a turbulent layer near the reported CAT levels and that at least 3 PIREPs were CAT. The heights and location at which the CAT occurred coincide with theoretically prone CAT regions relative to the development of a COL and upper air jet stream (Section 2.1.1, 2.1.2). CAT was experienced on the southern side of the subtropical jet stream (BEBAS), where wind shear takes place near the core of the upper air jet stream. The other CAT region (KYV) is closer to the COL than the upper air jet stream core and could possibly be CAT generated east relative to the COL and induced by Kelvin-Helmholtz instability, however more research is needed to confirm (Figure 2.3 3 and Figure 4.2) (Section 2.1.1).

The following Section discusses the Ellrod and the EDR indices as obtained from the CSEPS ensemble average and ensemble probability forecasts. These forecasts are compared to the observed CAT events. The investigation will focus on the three PIREPs that did take place over the waypoints KYV at 08h44 UTC, BEBAS at 14h27 UTC and KYV at 16h10 UTC. The time periods investigated considers two hours before and after the PIREP time stamp and the two model levels surrounding the height of the PIREP. See Table 4.2 for the hours and levels investigated for each PIREP. The levels around the observations were investigated along with the time, so to determine any CSEPS model time and level biases along with the evaluation towards the severity of the CAT event and location.

4.2.2 KYV – waypoint

Turbulence was reported twice at the way point, KYV on 16 July 2018. LGT-MDT turbulence was reported at 08h44 UTC at FL370, and LGTT in the afternoon at 225hPa/FL360 (Table 4.1). The morning PIREP will be investigated at 225hPa/FL360, since FL370 is the closest to that available model hight.

The geographical distribution of the ensemble average (ENS AVE) of the Ellrod and EDR indices at 225hPa/FL360 is given in Figure 4.7. Both indices predict an increase in values to the north-east and east of KYV (Figure 4.7), towards the position of the jet stream (>30 ms^{-1}, indicated by the black contour line on Figure 4.7 left). There is a general decrease in values to the west and south-west, with the exception of the south coast and adjacent interior (Figure 4.7). The EDR forecast pattern disagrees with the Ellrod forecast as to where maximum turbulence was predicted. The EDR forecast showed a band of SVRT (> 0.7) extending further northeast than the Ellrod forecast

(>8). Figure 4.7 shows that SVRT was predicted by both indices at the waypoint, KYV and does not agree with the observation of LGT-MDTT. It is noted that the region of SVRT predicted by the EDR forecast is over the generally cloud free area but extends to the location of the upper air jet stream where there are tight gradients of isotachs. Holopainen, (1962) stated that turbulence occurs where there is a sudden increase in wind speed resulting in an increase in dissipation rate (Section 3.3.2 d). Unfortunately, in the absence of turbulence observations, it is not possible to provide an opinion about the accuracy of the SVRT forecasts.

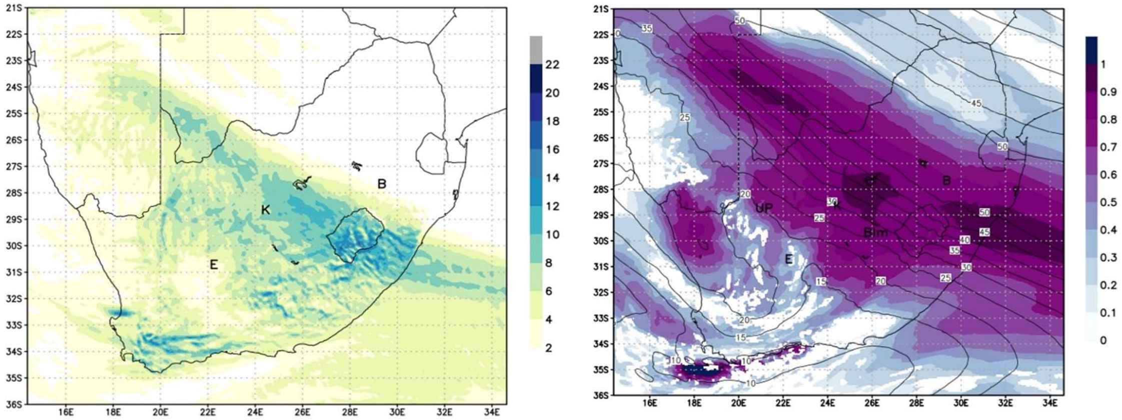

Figure 4.7: The Ellrod index ensemble average (left), and the EDR index ensemble average (right) with the ensemble average windspeed overlayed from the CSEPS on 16 July 2018 at 09h00 UT at 225hPa/FL360. The ensemble average wind speed (kt) is indicated by the black labelled contours. E denotes the way point EGNOM, where K is KYV, B is BEBAS and UP is Upington and Blm is Bloemfontein Airport, respectively.

Table 4.2 shows that the Ellrod ENS AVE predictions at KYV, 225hPa/FL360 predicted a SVRT (> 0.7) event from 07h00UTC to 09h00UTC followed by MDTT from 10h00 UTC to 11h00 UTC. The Ellrod ENS AVE forecast at 200hPa/FL390 in the morning was below the minimum value for turbulence for the entire 5hr time period (Table 4.2).

Table 4.2: The ensemble average at the waypoint KYV for the Ellrod (top) and EDR (bottom) indices on 16 July 2018 at 250hPa/FL340, 225hPa/FL360 and 200hPa/FL390 level, from 07h00 to 11h00 UTC. The grey cells show the model time and level which are closest to the observation. The results that fall within the event thresholds are highlighted. Orange Ellrod values indicate MDT (4-8) and dark blue Ellrod values indicate SVR (>8) turbulence forecasts (top). Purple EDR values indicate MDT (0.4-0.7) and red EDR values indicate SVR (>0.7) turbulence forecasts (bottom). LGT-MDTT was observed in the morning at KYV.

Time (UTC):	**250hPa/FL340**	**225hPa/FL360**	**200hPa/FL390**
Ellrod $10^{-7}s^{-2}$:			
07h00	9.83	9.28	1.88
08h00	10.17	8.76	1.60
09h00	8.72	8.24	1.78
10h00	8.04	7.12	1.80
11h00	7.76	7.34	1.98
EDR $\boldsymbol{m^{2/3}s^{-1}}$:			
07h00	0.95	0.94	0.77
08h00	0.93	0.91	0.73
09h00	0.89	0.87	0.70
10h00	0.87	0.85	0.69
11h00	0.85	0.83	0.68

Table 4.2 shows that there was a rapid decrease of Ellrod ENS AVE values with height, over a very short distance. It could therefore be considered that a LGT-MDT turbulence event may not be forecast at 225hPa/FL360 or between 225hPa/FL360 and 200hPa/FL390, since at 225hPa/FL360 (closer to FL370) a SVRT event is forecast. It is conceivable that a rounding error in determining the pressure level (model height) closest to FL370 could have resulted in this discrepancy of the Ellrod index between the forecast and the observation. The EDR ENS AVE predicted SVRT at 09h00 UTC at 225hPa/FL360 and MDTT at 0900UTC at 200hPa/FL390, this followed a 2-hr period of SVRT at the same level. Neither the Ellrod nor the EDR ENS

AVE values predicted the severity of the CAT event well at 09h00. It is seen that an over-forecasting of the CAT severity from the ENS AVE from both indices are evident.

The Ellrod ensemble probability (ENS PROB) forecast at 09h00 UTC at 225hPa/FL360 indicated a 50% probability towards a MDTT (4-8) event (Figure 4.8).

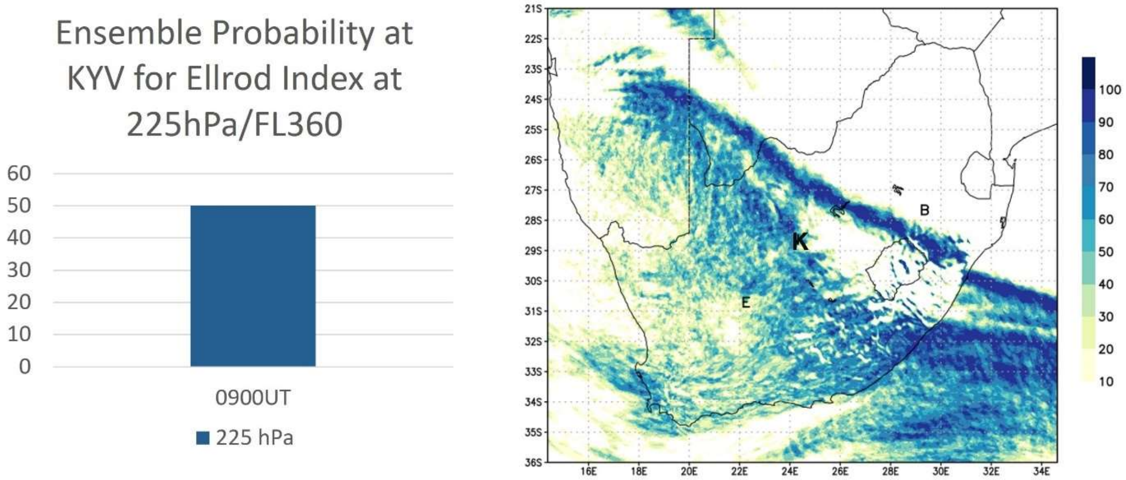

Figure 4.8: The Ellrod ensemble probability on 16 July 2018, at 225hPa/FL360. The E denotes the waypoint EGNOM, K is KYV, and B is BEBAS.

It is shown by the ensemble meteogram (Figure 4.9) of the Ellrod index values at KYV, that the spread of the ensemble members is symmetrical around the median (8.24) since the 'box' is from 7 to 9.5 Ellrod index values. That enforces confidence towards the forecast of a MDT-SVRT event and not a LGT-MDTT event as observed (Table 4.1). It was noted that the Ellrod ENS PROB forecast towards a LGTT event increased to 66% at 350hPa/FL260 and a MDTT event at the lower levels of the atmosphere, which became indicative of 58 – 60% from 325hPa/FL280 to 275hPa/FL320.

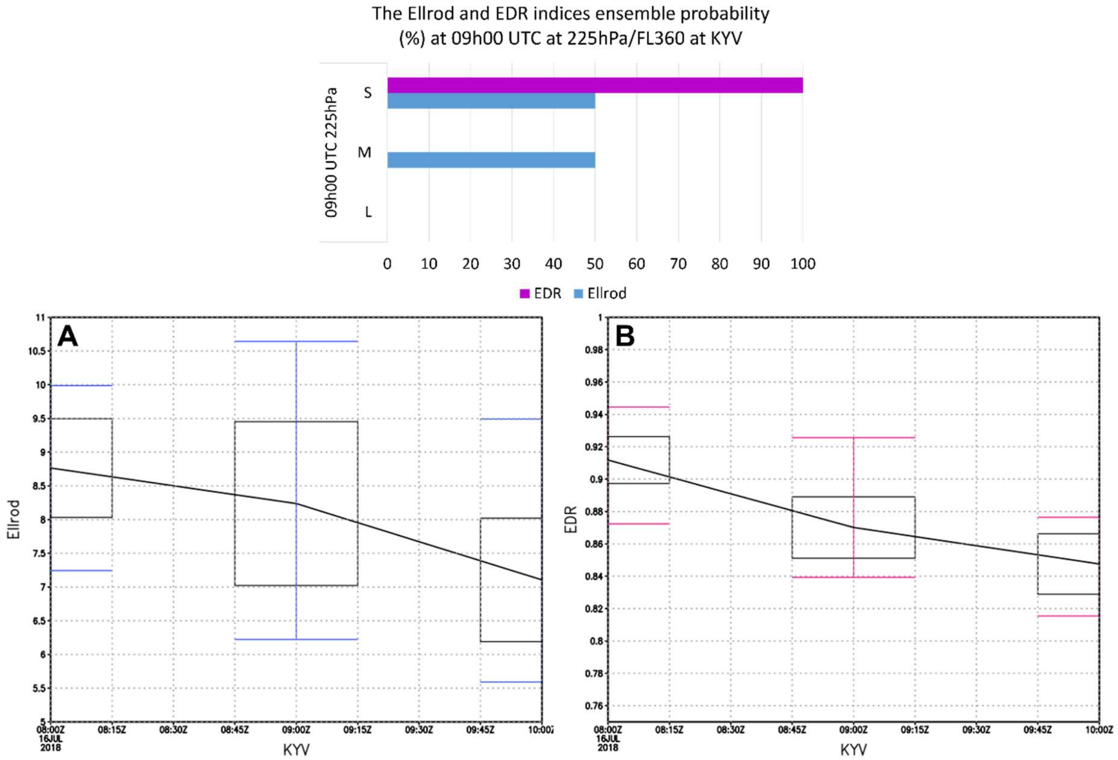

Figure 4.9: The ensemble meteogram on 16 July 2018, at 225hPa/FL360 from 08h00 to 10h00 UTC for both Ellrod (A) and EDR (B) indices at the way point KYV. The ensemble probability for the same time and level at KYV is shown on top for both indices. Blue represents the Ellrod forecast and the purple the EDR forecast. The middle box and whisker plot represents the corresponding event at 09h00 UT. The box and whisker plots are indicated per hour on the x-axis. The indices values are indicated on the y-axis. The black line within the boxes represents the median values. The 25% to 75% probability quartiles are represented by the bottom and top sides of the box. The whiskers and the vertical (blue and magenta) lines depict the lower and upper quartiles. Whereas the lower quartiles show the values where the probability is less than 25%, and the top quartiles are the values where the probability is more than 75%.

The EDR ENS PROB forecast for the same morning event, 09h00 UTC, predicted a probability of 100% in favour of a SVRT event at 225hPa/FL360 (Figure 4.9). The EDR index ensemble meteogram indicates a higher tendency towards a SVRT event than the Ellrod index forecast (Figure 4.9 50%). It is also noted that by the ensemble members being above the minimum limit of the SVRT threshold (>0.7) and the ‘box’ is a lot more compressed around the median (0.87) (Figure 4.9 right), the ensemble spread has a tendency towards a SVRT event. The EDR ENS PROB towards a LGTT event was 50% and more only at 375hPa/FL240 and 175hPa/FL410. It was noted that the ENS PROB towards a MDTT event, from the EDR index forecast of more than 50% was found at lower levels, 350hPa/FL260 to 325Pa/FL280, and from 200hPa/FL390 to 175hPa/FL410.

In the afternoon at 16h10 UTC at 225hPa/FL360 the Ellrod ENS AVE forecast predicted a MDTT, even though LGTT was observed (Table 4.3). The predictions at the surrounding levels and times were mostly for MDTT, but not at 200hPa (Table 4.3). The EDR ENS AVE forecast predicted SVRT at 16h00 UTC decreasing to MDTT in the early evening, with a general SVR-MDTT events at the surrounding times and levels.

Table 4.3: The ensemble average at the waypoint KYV for the Ellrod (top) and EDR (bottom) indices 16 July 2018 at 250hPa/FL340, 225hPa/FL360 and 200hPa/FL390 level, from 14h00 to 18h00 UTC. The grey cells show the model time and level which are closest to the observation. The results that fall within the event thresholds are highlighted. Green Ellrod values indicate LGT (2-4) and orange Ellrod values indicate MDT (4-8) turbulence forecasts (top). Purple EDR values indicate MDT (0.4-0.7) and red EDR values indicate SVR (>0.7) turbulence forecasts (bottom). LGTT was observed in the afternoon at KYV.

Time (UTC):	**250hPa/FL340**	**225hPa/FL360**	**200hPa/FL390**
Ellrod $10^{-7}s^{-2}$:			
14h00	7.28	6.76	1.26
15h00	6.47	6.08	1.15
16h00	6.01	5.05	0.84
17h00	5.30	4.84	0.72
18h00	4.67	3.83	0.43
EDR $\boldsymbol{m^{2/3}s^{-1}}$:			
14h00	0.76	0.77	0.63
15h00	0.75	0.75	0.60
16h00	0.74	0.74	0.55
17h00	0.72	0.72	0.53
18h00	0.70	0.70	0.49

Similar to the results depicted in Table 4.2, the ENS AVE of the Ellrod values predicts the same decrease in predicted values between 225hPa and 200hPa in Table 4.3. The Ellrod ENS PROB towards a LGTT event was only 17%, and did not become in favour at any other levels. The EDR ENS PROB towards a LGTT event was nil at 225hPa/FL360 and become in favour of LGTT at 175hPa/FL410. The Ellrod index meteogram illustrated a relatively large ensemble spread of the ensemble members forecast values. All the values were within the MDTT range, except for the minimum value. The uncertainty is similar as to what is seen at 09h00 UTC (Figure 4.9) and more than 80% of the ensemble members predicted a MDTT at 225hPa/FL360. That is not aligned with the observation of a LGTT event. The EDR ENS PROB forecast is 100% towards a SVRT event (Figure 4.9). The EDR ensemble uncertainty is less than that of the Ellrod ENS PROB forecast and has a very narrow ensemble spread. The EDR ENS PROB forecast at 16h00 UTC at 225hPa/FL360 did not capture the event well.

At the waypoint KYV, the Ellrod and EDR ENS AVE forecasts did not capture the turbulence observation well at KYV at 09h00 UTC nor at 16h00 UTC. The severity of the CAT events from the ENS AVE forecasts at 225hPa/FL360, seems to be an overestimation form both indices (Table 4.2&4.3). The Ellrod ENS PROB forecast captured a MDTT event, since 50% and above is considered a hit. The Ellrod EMS PROB forecast did not capture the PIREP event of LGT-MDT turbulence, since the forecast had a tendency towards a MDT-SVR turbulence event. The EDR forecast indicated less uncertainty than the Ellrod forecast despite not capturing the observations at 225hPa/FL360.

4.2.3 BEBAS – waypoint

This Section will focus on the time period from 12h00 to 16h00 UTC and the levels from 325hPa/FL280 to 275hPa/FL320. The PIREP at the BEBAS waypoint, which is located in the northern parts of KZN, near the border of the Free State province had logged a MDTT event. The event was observed at 14h24 UTC, at 300hPa/FL300 (Table 4.1) over a generally cloud free region and underneath the upper air jet stream (Figures 4.1-3, 4.6). The CAT experience at BEBAS may be generated due to the wind shear underneath the upper air jet stream (south of the 40 ms^{-1} ensemble average wind speed in Figure 4.9 right) (Section 2.1).

It is distinguishable that from Figure 4.7 and Figure 4.10 the upper air jet stream over the eastern parts RSA has migrated eastwards. The Ellrod ENS AVE values increase to the south-west of BEBAS, away from the upper air jet stream core but decrease to the extreme north-eastern parts of RSA (Figure 4.10 left). The EDR ENS AVE values, in comparison indicates a broader region of maximum value that extend further to the northeast but still south of the 40 ms^{-1} (jet stream core, > 30 ms^{-1}) ENS AVE wind speeds seen in Figure 4.10 (right). It should be kept in mind that in the absence of turbulence observations, it is difficult to provide an opinion about the accuracy of these forecasts.

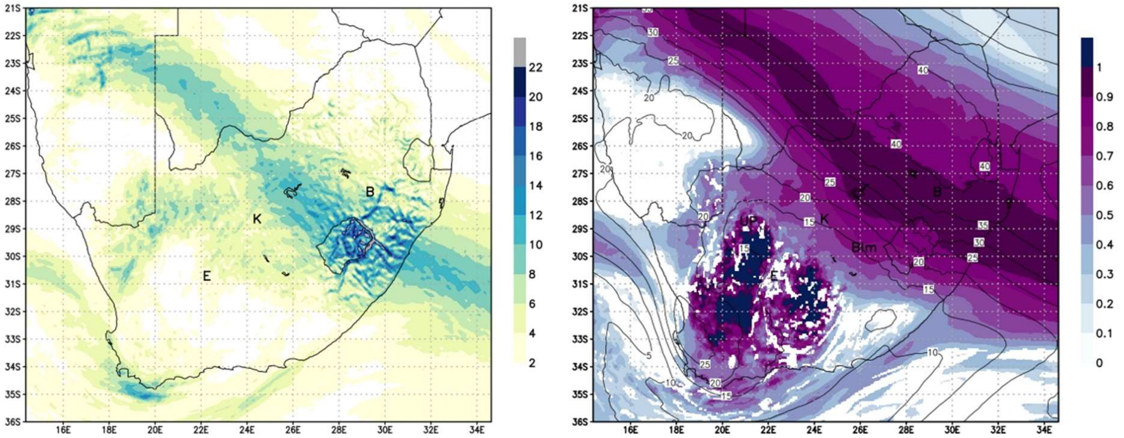

Figure 4.10: The Ellrod index ensemble average (left), and the EDR index ensemble average (right) with the ensemble average windspeed overlayed from the CSEPS on 16 July 2018 at 14h00 UT at 300hPa/FL300. The ensemble average wind speed is indicated by the black labelled contours. E denotes the way point EGNOM, K is KYV, B is BEBAS and UP is Upington and Blm is Bloemfontein Airport, respectively.

At 300hPa/FL300 at 14h00 UTC the Ellrod ENS AVE predicted a MDTT event at the time of the observation, as well as MDTT to occur at the surrounding levels and times (Table 4.4). The Elrod ENS AVE forecast predicted the observation well. The location of the CAT report coincides with the location of where theoretical MDT wind shear takes place near the upper air jet stream core (Section 2.1.2). The EDR ENS AVE forecast predicted, on the other hand, a SVRT event at 300hPa/FL300 at 14h00 UTC which seems to be an overestimation towards the turbulence severity observed (Table 4.4).

Table 4.4: The ensemble average at the waypoint BEBAS for the Ellrod (top) and EDR (bottom) indices 16 July 2018 at 325hPa/FL280, 300hPa/FL300 and 275hPa/FL320 level, from 12h00 to 16h00 UTC. The grey cells show the model time and level which are closest to the observation. The results that fall within the event thresholds are highlighted. Orange Ellrod values indicate MDT (4-8) turbulence forecasts (top) and the red EDR values indicate SVR (>0.7) turbulence forecasts (bottom). MDT CAT was observed in the afternoon at BEBAS.

Time (UTC):	**325hPa/FL280**	**300hPa/FL300**	**275hPa/FL320**
Ellrod $10^{-7}s^{-2}$:			
12h00	6.06	5.64	4.54
13h00	5.95	5.84	5.05
14h00	6.55	6.66	5.84
15h00	6.62	6.66	5.86
16h00	6.65	6.57	5.83
EDR $\boldsymbol{m^{2/3}s^{-1}}$:			
12h00	0.89	0.92	0.93
13h00	0.89	0.92	0.91
14h00	0.88	0.92	0.91
15h00	0.87	0.92	0.92
16h00	0.87	0.92	0.92

It is noteworthy to compare the EDR ENS AVE forecast from Table 4.3 to Table 4.4. Similar to the PIREP at KYV for the EDR ENS AVE forecast, there is an overestimation of the severity of the turbulence event from 325hPa/FL280 to 225hPa/FL360. The maximum EDR ENS AVE values pattern extends over a similar region at 09h00 UTC at 225hPa/FL360 (Figure 4.7 right) as at 14h00 UTC at 300hPa/FL300 but moved slightly to the northeast, as the system moved eastwards (Figure 4.9 right), over the waypoint BEBAS. There is, however a more defined narrow band of maximum EDR ENS AVE values at 14h00 UTC at 300hPa/FL300 (Figure 4.9 right), which was also seen at 09h00 UTC at 300hPa/FL300 (not shown). This correlates to the assumption that TKE contributes more at lower levels of the atmosphere than near the tropopause and as the system intensifies, since the COL only started to dissipate late into the evening and early morning hours of the 17th July 2018 (Section 2.1). More research is needed to confirm that assumption, that TKE at lower levels of the atmosphere may be one of many contributing factors for the overestimating from the EDR ENS AVE forecasts.

The Ellrod ENS PROB forecast was 100% indicative towards a MDTT event, whereas the EDR ENS PROB forecast was 100% towards a SVRT event at 300hPa/FL300 at 14h00 UTC. The EDR ENS PROB indicated no probability towards a MDTT event, even at surrounding model levels. The Ellrod ENS PROB is further additionally supported by the ensemble meteogram for the Ellrod index forecast at BEBAS seen in Figure 4.11 (A).

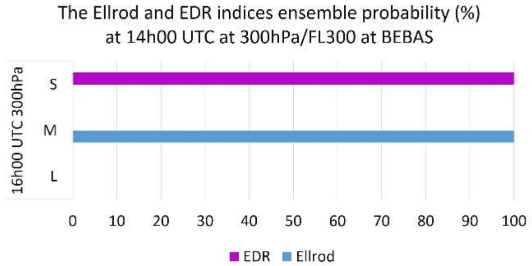

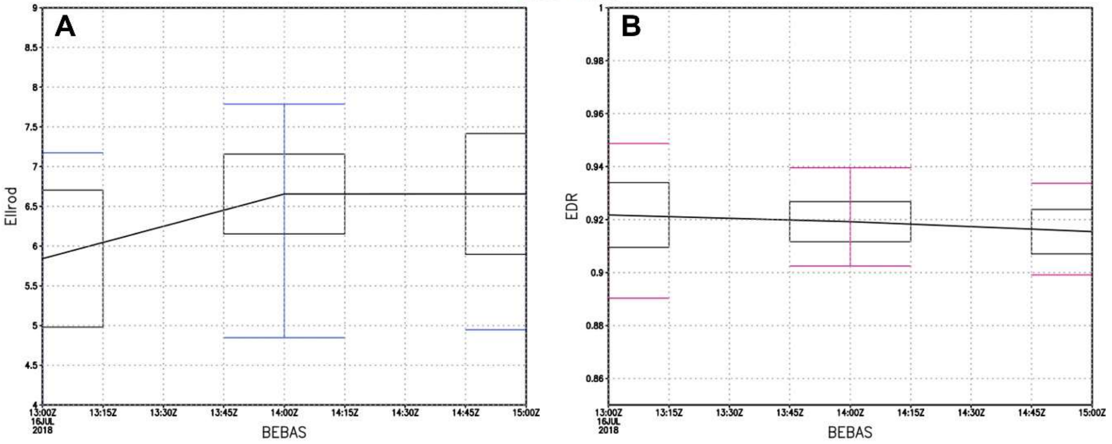

Figure 4.11: The ensemble meteogram for 16 July 2018, at 300hPa/FL300 for both Ellrod (A) and EDR (B) indices at the waypoint BEBAS, from 13h00 to 15h00 UT. The middle box and whisker plot represents the corresponding event at 14h00 UT. The box and whisker plots are indicated per hour on the x-axis. The index values are indicated on the y-axis. The red rectangle highlights the observation hour. The black line within the boxes represents the median values. The 25% to 75% probability quartiles are represented by the bottom and top sides of the box. The whiskers and the vertical (blue and magenta) lines depict the lower and upper quartiles. Whereas the lower quartiles show the values where the probability is less than 25%, and the top quartiles are the values where the probability is more than 75%. The red box highlights the boxplot corresponding to the event.

The ensemble meteogram for the Ellrod index at BEBAS (Figure 4.11, A) shows larger uncertainty than the EDR forecast (Figure 4.11, B), since the EDR index meteogram displays a more narrow ‘box’. The Ellrod ensemble meteogram 25 and 75% quartiles lie within the MDTT threshold (Figure 4.11, A) which coincides with the observation.

At the waypoint BEBAS, the Ellrod index forecast from the ENS AVE and ENS PROB forecasts proved to capture the observations from the PIREP well. The EDR index ENS AVE and ENS PROB forecasts missed the observations and overestimated the event severity, even though the EDR forecasts had less uncertainty.

Furthermore, it should be noted that position and time uncertainties have been evident in PIREPs (Sharman, et al., 2006), as well as the lack of observations could therefore contribute to the overestimating from the PIREPs. That would lead to misinterpretation of the CSEPS output. In general, there was evidence of overestimation from the ENS AVE forecasts for both indices and an underestimation from the ENS PROB forecast of both indices. It could be plausible that the increase in the CAT severity from the EDR ENS AVE forecast, may be due to an increase of magnitude of the temperature and buoyancy parameters within the TKE equation. That is calculated at the grid points within in the generally cloud free region, just south of the jet stream core (Figure 4.3, 4.6). The kinetic eddy dissipation rate is known to increase with the increase in wind speed as well, where the wind speeds increase from 25 to more than 40 ms^{-1} (Holopainen, 1962) (Section 2.2.1 a, 3.3.2 d). The assumption of the overestimation of wind speeds (3.3.2 c), may also influence the Ellrod index forecast values. Based on the assumption that the equation of the Ellrod index is double the result of vertical wind shear alone. It could be said that based on the severe wind shear calculation from the FABL skew-T diagram near the PIREP flight level (Figure 4.4) that MDTT to SVRT may be expected. Research is needed to confirm the aforementioned assumptions.

The following Section 4.3 discusses the other case study dates that fall within the COL weather pattern category as well as the other two weather pattern categories. The case studies details are tabulated in Table 4.5, 4.6a, b and 4.7 (Section 4.3). The tables list the case study dates in each weather category. The PIREP information is then listed along with the CSEPS output. The CSEPS forecasts are highlighted in grey when the CSESP output coincides with the observation. The first day, 16 July 2018 is discussed in Section 4.2 and the following dates under the COL weather category discussion follows in the Section 4.3.

4.3 Case study tables

4.3.1 Cut-off low pressure case events

The remainder of the case studies for the COL weather category are 20 May, 9 August and 3 September 2018 (Table 4.5) and the discussions follow before Table 4.5.

On 20 May 2018 the COL was positioned over the western interior of South Africa at 300hPa/FL300, but fully cut-off at 400hPa/FL240. Turbulence was reported 20 nm north of EGNOM waypoint, which was located south-east of the COL. A tight geopotential gradient at 300hPa and 400hPa was found east of the amplification of the upper COL (trough line), resulting in wind speeds of more than 25 ms^{-1}. A LGT turbulence event was logged at 15h20 UTC on 20 May 2018 at 275hPa/FL320 within a cloud free region. The LGTT event was captured well by both Ellrod and EDR indices ENS AVE forecasts (Table 4.5). The probability for LGT turbulence to occur was predicted to be 58% by Ellrod ENS PROB and the EDR ENS PROB indicates an 83.33% probability towards a LGT turbulent event. The ensemble meteogram of both indices had a symmetrical ensemble spread round the median. However, there was greater uncertainty from the EDR ensemble meteogram due to a wider ensemble spread around the median.

On 09 August 2018 the COL was situated south-west of the country at 400hPa/FL240. The PIREP logged LGT-MDT turbulence at 225hpa/FL360, at 06h18 UTC at the KYV waypoint. The turbulence event took place far north-east of the COL, however, within 100 nm of the upper air jet stream core. The jet stream core was found over the southern parts of Namibia extending across the central parts of RSA and exiting the county over the southern parts of the KwaZulu-Natal province.

The Ellrod index ENS AVE forecast is MDTT at 225hPa/FL360. When looking at surrounding model levels, the forecast becomes LGTT below the observational level and thus there is LGT to MDT turbulence around the observation. The EDR index ENS AVE forecast in comparison however, indicated a LGTT event but no MDTT was predicted, only at higher model levels.

The ENS PROB of a LGTT and MDTT events were captured by the Ellrod indices to occur at a 33 and 58% chance, respectively at 06h00 UTC at 225hPa/FL360. The EDR ENS PROB forecast indicated an 83.33% chance towards a LGTT event and a

17% chance for a MDTT event to occur at 06h00 UTC at 225hPa/FL360. The variability within the ensemble members of the ELLROD forecast at 06h00 UTC leads to large uncertainty. That was noted by the wide box and whisker plot at 06h00 UTC at 225hPa/FL360, for the waypoint KYV. The 25% quartile lies below the LGTT event threshold, but the 75% quartile is within the MDTT threshold. The tendency is thus towards a MDTT event. With regards to the EDR ENS PROB forecast, the uncertainty at 06h00 UTC becomes less towards a LGT turbulence event. That was noted since the entire 'box' is within the LGTT threshold. The PIREP was captured by both indices' forecasts, since the observation is a combination of a LGT to MDT turbulence. There is large uncertainty however, in comparison, the ENS PROB towards a MDTT event was larger from the ELLROD ensemble members spread, where the probability towards a LGTT event from the EDR ensemble members spread was narrower.

On 03 September 2018 the COL was situated south-east of South Africa at 500hPa/FL180. The MDTT PIREP was logged over the southern parts of the Eastern Cape near the waypoint, OKREV. The way point is found at the back end of the cut-off low where the PIREP logged MDT turbulence at 04h55 UTC at FL350. The observation took place closest to the model level of 250hPa/FL340. The observation relative to the COL is found within the region where the upper air jet stream splits away from the main westerly flow. The jet stream core within the COL was situated over the central interior of SA extending to the eastern parts and exiting over northern KwaZulu-Natal. An upper air jet stream core was found over the southern parts of Botswana extending across the northern parts RSA at 300hPa/FL300.

The Ellrod forecasts on 03 September 2018 at 05h00 UTC of the ENS AVE predicted the MDT turbulent event at 250hPa/FL340, whereas the EDR ENS AVE forecast did not capture the MDT event, but rather a LGTT event. The Ellrod forecast therefore captured the event well. The EDR forecast did not predict the observation (MDT event) well yet underestimated the intensity, but spatial and temporal aspects were predicted well. Regarding upper air low formation, studies have shown that light turbulence is associated with regions just south of a low centre, however, turbulence of larger intensity is rarely forecast in a similar region (Hopkin, 1977). In this case however, the location is south-west of the COL over rough and mountainous terrain, where the jet steam core around the COL is generated after the cyclogenesis redevelopment (Figure 2.3 3). The terrain may have contributed to the turbulence intensity increasing from LGT to MDT within the atmosphere. Yet more research is needed however to confirm the extent of surface terrain influence on CAT generation, other than mountain wave turbulence.

The Ellrod ENS PROB at 05h00 UTC predicted a 33% probability of MDTT to occur. The ENS AVE (mean) is within the MDTT threshold at 4.9. The ensemble meteogram of the Ellrod index on 03 September 2018 at 05h00 UTC, had indicated that the 25 and 75% quartiles are between 2 and 8, and the spread ranges from just below 1 to 10. Only 4 out of 12 of the ensemble members where within the MDTT threshold. It was noted that there was a 25% probability of a LGTT and SVRT at 250hPa/FL350. The meteogram provided confirmation that there is large uncertainty, but the ensemble members tend towards an MDTT event since a majority of the ensemble members values are between 4 and 8. The Ellrod ENS PROB did not capture the event well, since 50% probability is considered a hit for this research. The EDR ENS PROB forecast indicated a 17% probability of MDTT and 58% probability of a LGTT event. The ensemble meteogram of the EDR index on 03 September 2018 at 05h00 UTC, showed that the ensemble spread is similar to the Ellrod index meteogram, thus indicative of large uncertainty. The ensemble tendency is in favour of a LGT-MDTT event since the EDR index values range from below 0.1 to 0.5. The EDR ENS PROB forecast did not capture the MDTT event but underestimated the event severity.

The COL weather category had a total of 5 PIREPs (Table 4.5). Light and moderate turbulence intensity were observed more often than SVRT, whereas the combination of LGT-MDTT was reported twice. However, this is not to say that SVR turbulence did not take place. The location of the events was in similar regions for the 4 days over RSA, except on 3 September 2018. 2 waypoints, namely, EGNOM and KYV, were often utilised as location descriptions. This may be due to the waypoint locations being beneath a major flight path (Figure 4.1b), (which is fixed and does not change). This could also be due to the area relative to the COL's movement path over RSA, i.e. being from west to east and the position of the COL and timing of the event. The events took place on the eastern side of the COL, and on the southern side (cold side) of the upper air jet stream core. One case was observed at the back end relative to the COL.

The following Table 4.5 is the summary of the COL weather category that following the aforementioned discussion.

Table 4.5: PIREP of turbulence reported at the locations listed by case study dates categorised under the COL weather pattern for the of 2018. The flight level is indicated by FL and the pressure level closest to the flight level in the CSEPS data are included in hPa. The CSEPS forecast output in grey indicates a good forecast (Hit), the up arrow indicates that the forecast event severity was more than observed and down, is less than observed. 'High' indicates that the ensemble probability reflected the observation at a higher model level, and 'low' when it's a level lower than observed. 'No' is when the forecast is below the minimum limit of the lowest threshold. LGT=light, MDT=moderate and SVR=severe.

Weather system and date	**Time (UTC)**	**Waypoint**	**Level (hPa/FL)**	**Observation**	**Ensemble average**		**Ensemble probability (%) and severity**		**Event forecast level**	
COL					Ellrod	EDR	Ellrod	EDR	Ellrod	EDR
16 July 2018	08h44	KYV	225hPa/FL360 FL370	LGT-MDT	SVR ↑	SVR ↑	LGT, 0 ↓	LGT, 0 ↓	Low	High
							MDT, 50	MDT, 0 ↓	Hit	High
	16h10	KYV	225hPa/FL360	LGT	MDT ↑	SVR ↑	LGT, 17 ↓	LGT, 0 ↓	High	High
	14h27	BEBAS	300hPa/FL300	MDT	MDT	SVR ↑	MDT, 100	MDT, 0 ↓	Low	High
20 May 2018	15h20	20 nm N EGNOM	275hPa/FL320	LGT	LGT	LGT	LGT, 58	LGT, 83	Hit	Hit
09 Aug 2018	06h18	KYV	225hPa/FL360	LGT-MDT	MDT	LGT	LGT, 33 ↓	LGT, 83	Low	Hit
							MDT, 58	MDT, 17 ↓	Hit	High
03 Sep 2018	04h55	OKREV	250hPa/FL340 FL350	MDT	MDT	LGT ↓	MDT, 33 ↓	MDT, 17 ↓	Hit	Low

Source: PIREP data and CSEPS data

4.3.2 Upper air trough case events

This weather category has 5 case study dates, 03 May, 21 May, 03 October, 05 November, and 09 December 2018 with a total of 23 PIREPs (Table 4.6a-b). The following paragraphs discuss the case study dates.

The investigation for the 03 May 2018 focusses on 2-time intervals, namely 05h00 UTC and 14h00 to 15h00 UTC, and there are a total of 8 PIREPs (Table 4.6a). The two morning PIREPs on 03 May 2018, took place over the Northern Cape province, north north-west relative to the upper air trough within a cloud free area. Both PIREPs indicated a LGT turbulence events at the same level, 175hPa/FL410 but at 04h47 UTC and 05h00 UTC, respectively. The Ellrod ENS AVE forecasts overestimated the severity at both PIREPs at 175hPa/FL410, and the Ellrod ENS PROB underestimated the event severity. The EDR captured the LGT event well of the first PIREP with 100% EDR ENS PROB. The EDR ENS AVE forecast of the second PIREP, did not predict a LGTT event, but rather indicated a large area of MDT to SVR turbulence near the EGNOM waypoint. The Ellrod index ensemble box and whisker plot illustrated large uncertainty in the forecast, but less uncertainty from the EDR index ensemble metoegram.

The remaining six afternoon PIREPs took place over the eastern Free State province, being relatively north to the upper air trough, within a cloud free area. All six logged a MDTT event between 225hPa/FL360 and 175hPa/FL410 at 14h00 to 15h00 UTC, respectively. In the afternoon, the three events that took place closer to 14h00 UTC at 200hPa/FL390, 175hPa/FL410 and 225hPa/FL360 the Ellrod ENS AVE values are indicative of a LGTT, MDTT and SVRT events (Table 4.5a). The EDR ENS AVE values indicated a LGTT and two MDTT events, respectively. The Ellrod ENS AVE was at least once a hit at waypoint BLV, and the EDR ENS AVE was twice a hit at BLV and GEPES waypoints. Both indices underestimated the event at IMSIR, waypoint. The EDR ENS PROB forecast predicted the BLV and GEPES events well. The Ellrod ENS PROB forecast in comparison, only captured the MDTT event at BLV, where the forecast underestimated both events at IMSIR and GEPES. The ensemble meteogram of both indices, indicated similar spreads to that seem from the COL case studies. The EDR index ensemble members forecasts shows less uncertainty than the Ellrod index ensemble members forecasts.

The last three PIREPs, at 15h00 UTC (14h54 UTC Table 4.6a), both the Ellrod and EDR ENS AVE forecasts were a hit at APMIN, and the point 25 nm south of KYV. At the last PIREP at APRAX, the Ellrod ENS AVE forecast overestimated the severity and the EDR ENS AVE forecast underestimated the severity. The ENS PROB forecasts of both indices underestimated the severity as well at the same point, APRAX. The CSEPS ENS PROB forecast only captured a MDTT events at higher model levels for the Ellrod index more often than at lower level when underestimating. The EDR index ENS PROB forecasts were a hit at a lower model hights more often when underestimating.

On 21 May 2018, 5 LGT to MDT turbulence events were logged over the Northern Cape province in the morning and afternoon (Table 4.6a-b). In the upper air at 250hPa/FL340, an upper air jet, with winds speeds of 30 to 45 ms^{-1}, was situated over the far north-eastern (Limpopo province) parts of South Africa. All the waypoints that were logged on that day, were north-east within a cloud free area relative to the upper air trough (over the central parts of SA, Free State province), found west of the RSA. In the morning, at 06h00 UTC at FL350 (close to 250hPa/FL340) the Ellrod index ENS AVE forecast indicated at the waypoint KYV, a LGTT event at 250hPa/FL340 and the EDR index ENS AVE forecast predicted a LGTT event. The forecasts of both indices captured the LGTT event well. The Ellrod and EDR indices ENS PROB forecasts indicated an 83% probability of a LGTT event occurring at the waypoint KYV at 06h00 UTC. The second location, 100 nm north of EGNOM, the EDR index captured the event well, but the Ellrod index ENS AVE forecast overestimated and the ENS PROB forecast underestimated the event.

At 07h00 UTC the Ellrod index ENS AVE indicated a LGTT event, whereas the EDR was indicative of a MDTT event. The ENS PROB forecast towards the LGTT event form the Ellrod index was a hit and the MDTT event from the EDR index forecast was a hit as well. The afternoon (12h25 UTC) PIREPs logged a LGTT event. The Ellrod index ENS AVE forecast indicated a ‘No’ event. The ENS AVE from the EDR index forecast captured the LGTT event. The EDR index ENS PROB forecast is a good forecast, but the Ellrod ENS PROB forecast underestimated the event and was a hit at a lower model level only. The evening (18h25 UTC) event was similar as to the afternoon, looking at the ENS AVE forecast of both indices. The ENS PROB forecasts form both indices, underestimated the event severity but the EDR index ENS PROB did capture the MDTT.

On 3 October 2018, an upper air trough was seen over the south-eastern parts of the country. The associated upper air jet stream core (35 to 42 ms^{-1}) was situated across the central parts of the country and exited over the southwestern parts of KwaZulu-Natal (not shown). On this day, there were two PIREPs, at 08h45 and at 16h34 UTC, therefore, 09h00 UTC and 17h00 UTC will be looked at. The pilot report logged a MDTT event at 09h00 UTC at 325hPa/FL280 near the waypoint, EXOKU, which was to the south-west of the Gauteng province and on the warm side of the upper air jet stream. The 17h00 UTC PIREP reported an LGT-MDTT event that was experienced 50 nm to the east of the waypoint, EVUVA, at 225hPa/FL360. That is found south of Lesotho and to the north-east relative to the upper air trough. The Ellrod index ENS AVE forecast at 09h00 UTC at 325hPa/FL280 generated values that fell within the LGTT threshold, which missed the observation of a MDTT event at EXOKU waypoint. The EDR index ENS AVE forecast is also within the LGTT threshold, thus underestimating the severity (Table 4.5b). The ENS PROB forecast of both indies underestimated the event and only captured the MDTT event at EXOKU at lower model levels for the Ellrod index and a higher model level for the EDR index. Similar, at the afternoon PIREP, at EVUVA waypoint at 225hPa/FL360, the LGT-MDTT event was underestimated by the Ellrod ENS PROB forecast. The Ellrod index ENS AVE only captured the LGTT event as well as the EDR index ENS AVE forecast. The EDR index ENS PROB forecast for the LGTT at 17h00 UTC, at EVUVA waypoint was captured well but underestimated the MDTT event. The ensemble meteograms of both indices indicated similar uncertainty to the other case studies, where the EDR index showed less uncertainty than the Ellrod index.

On the 5 November 2018 there were 3 PIREPs that were logged, 2 of which reported MDTT events at 09h00 UTC at 200hPa/FL380 near the waypoint NEXIT and at 09h53 UTC at 175hPa/400hPa near ETKAL, respectively. The third PIREP logged a LGTT event at 13h41 UTC at FL370 (closest to 225hPa/FL360) 60 nm north of the waypoint EGTIL. In the upper air a trough was found to the southwest and the upper air jet stream was over the western parts of the country. All three waypoints are located over the central Northern Cape and north-eastern parts of the Western Cape provinces. The events took place in a cloud free region north of the upper air trough and directly within the same location of the upper jet. It is seen on the 05 November 2018 that the ENS AVE forecast from both the Ellord and EDR indices did not captured the MDTT event. The ENS PROB forecast at 09h00 UTC either, both the Ellrod and EDR indices underestimated the event severity. The Ellrod index ENS AVE and ENS PROB forecasts captured the MDTT event at 10h00 UTC at ETKAL, but the EDR index ENS AVE and PROB forecasts underestimated the event. The third PIREP at 14h00 UTC, Ellrod index indicated a 'No' event and underestimated the severity from the ENS PROB forecast. The Ellrod ENS PROB forecast capture a LGTT at much higher model levels. The EDR index ENS AVE forecast overestimated the event, but the ENS PROB forecast underestimated the event severity and only indicated a probability 50% and more at higher model levels.

On 9 December 2018 to the west of the country at 250hPa/FL340 an upper air trough was located. Over the north-eastern parts the upper air jet stream core (42 to 47 ms^{-1}) was found extending from the southern parts of Botswana and exiting the country over the eastern parts of KwaZulu-Natal. There were five PIREPs that were logged on 09 December 2018, reporting LGTT events, with on LGT-MDTT. The CAT events occurred over the western interior of RSA and one occurred near the southern border of Lesotho. The waypoints were in a region of no clouds, however, the waypoint (ETLUR) near the southern border of Lesotho had cloudy conditions and was therefore omitted. It can be seen that the EDR index ENS AVE and ENS PROB forecasts captured the observations more frequently than the Ellord index forecast (Table 4.6b). The EDR index forecast also indicated less uncertainty than the Ellrod index forecasts, when investigating the ensemble meteograms of both indices which shed light on the confidence towards a certain threshold from the spread of the CSEPS members. That was also seen for the COL weather category. The Ellrod index ENS AVE forecasts of all the PIREPs overestimate all the events severity, but the ENS PROB forecasts from the Ellrod index, underestimated. (Table 4.6 b).

The following Table 4.6 a to b, is the summary of the trough weather category.

Table 4.6a: PIREP listed by case study dates categorised under the Trough weather pattern for 2018. The CSEPS forecast output in grey indicates a good forecast (Hit), the up arrow indicates that the forecast event severity was more than observed and down, is less than observed. 'High' indicates that the ensemble probability reflected the observation at a higher model level, and 'low' when it's a level lower than observed. 'No' is when the forecast is below the minimum limit of the lowest threshold. LGT=light, MDT=moderate and SVR=severe.

Weather system and date	**Time (UTC)**	**Waypoint**	**Level (hPa/FL)**	**Observation**	**Ensemble average**		**Ensemble probability and severity**		**Event forecast level**	
Trough					Ellrod	EDR	Ellrod	EDR	Ellrod	EDR
03 May 2018	04h47	40 nm W APLEN	175hPa/FL410	LGT	MDT ↑	LGT	LGT, 33 ↓	LGT, 100	Low	Hit
	05h00	140 nm E EGNOM	175hPa/FL410	LGT	SVR ↑	SVR ↑	LGT, 0 ↓	LGT, 0 ↓	Low	Low
	13h46	IMSIR	200hPa/FL390	MDT	LGT ↓	LGT ↓	MDT, 25 ↓	MDT, 25 ↓	High	Low
	14h20	BLV	175hPa/FL410	MDT	MDT	MDT	MDT, 58	MDT, 83	Hit	Hit
	14h20	GEPES FL370	225hPa/FL360	MDT	SVR ↑	MDT	MDT, 8 ↓	MDT, 50	High	Hit
	14h54	APMIN	200hPa/FL390	MDT	MDT	MDT	MDT, 50	MDT, 100	Hit	Hit
	14h54	25 nm S KYV	200hPa/FL390	MDT	MDT	MDT	MDT, 58	MDT, 100	Hit	Hit
	14h54	APRAX FL370	225hPa/FL360	MDT	SVR ↑	LGT ↓	MDT, 17 ↓	MDT, 33 ↓	High	High
21 May 2018	05h30	KYV FL350	250hPa/FL340	LGT	LGT	LGT	LGT, 83	LGT, 83	Hit	Hit
	05h30	100 nm N EGNOM	250hPa/FL340	LGT	SVR ↑	LGT	LGT, 0 ↓	LGT, 92	High	Hit

Source: PIREP data and CSEPS data

Table 4.6b: PIREP listed by case study dates categorised under the Trough weather pattern for 2018. The CSEPS forecast output in grey indicates a good forecast (Hit), the up arrow indicates that the forecast event severity was more than observed and down, is less than observed. 'High' indicates that the ensemble probability reflected the observation at a higher model level, and 'low' when it's a level lower than observed. 'No' is when the forecast is below the minimum limit of the lowest threshold. LGT=light, MDT=moderate and SVR=severe.

Weather system and date	**Time (UTC)**	**Waypoint**	**Level (hPa/FL)**	**Observation**	**Ensemble average**		**Ensemble probability and severity**		**Event forecast level**	
Trough					Ellrod	EDR	Ellrod	EDR	Ellrod	EDR
21 May 2018	07h21	45 nm SW KYV	225hPa/FL360	LGT-MDT	LGT ↓	MDT	LGT, 50	LGT, 0 ↓	Hit	Low (08h00 UTC Hit)
							MDT, 0 ↓	MDT, 100	Low (08h00 UTC hit)	Hit
	12h25	APMIN	225hPa/FL360	LGT	No ↓	LGT	LGT, 33 ↓	LGT, 83	Low	Hit
	18h25	EGTIL	175hPa/FL410	LGT-MDT	No ↓	MDT	LGT, 25 ↓	LGT, 25 ↓	Low	Low
							MDT, 0 ↓	MDT, 67	Low	Hit
03 Oct 2018	08h45	Towards EXOKU	325hPa/FL280	MDT	LGT ↓	LGT ↓	MDT, 8 ↓	MDT, 0 ↓	Low	High
	16h34	50 nm E EVUVA	225hPa/FL360	LGT-MDT	LGT	LGT	LGT, 33	LGT, 82	Low	Hit
							MDT, 16 ↓	MDT, 0 ↓	High	No
05 Nov 2018	09h00	NEXIT	200hPa/FL390	MDT	LGT ↓	No ↓	MDT, 17 ↓	MDT, 0 ↓	High	Low
	09h53	ETKAL	255hPa/FL360	MDT	MDT	LGT ↓	MDT, 58	MDT, 17 ↓	Hit	Low
	13h41	**60 nm N EGTIL FL370**	**225hPa/FL360**	**LGT**	**No** ↓	**MDT** ↑	**LGT, 8** ↓	**LGT, 42** ↓	**High**	**High**

09 Dec 2018	**12h50**	**SLV**	**250hPa/FL340**	**LGT**	**SVR ↑**	**LGT**	**LGT, 0 ↓**	**LGT, 50**	**Low**	**Hit**
	14h35	5 nm W EGNOM	200hPa/FL390	LGT	MDT ↑	LGT	LGT, 33 ↓	LGT, 100	Low	Hit
	14h38	105 nm W EGNOM	200hPa/FL390	LGT	MDT ↑	MDT ↑	LGT, 8 ↓	LGT, 0 ↓	Low	Low
	18h31	EXELO	225hPa/FL360	LGT	SVR ↑	SVR ↑	LGT, 0 ↓	LGT, 0 ↓	Low	Low
	20h55	80 nm W EGNOM	250hPa/FL340	LGT-MDT	SVR ↑	LGT	LGT, 0 ↓	LGT, 75	Low	Hit
							MDT, 75	MDT, 17 ↓	Hit	Low

Source: PIREP data and CSEPS data

4.3.3 Zonal flow case events

The Zonal flow weather category (Table 4.7) tabulated 4 PIREPs over two days. The case study dates investigated are, 10 June that has 3 PIREPs and 18 November 2018, with one and will be discussed in the following paragraphs.

On the 10 June 2018 the mid to upper air flow was zonal, with no dominant upper air trough. However, at 500hPa/FL180, westerly winds speeds of 17 to 25 ms^{-1} were increasing with height to 200hPa/FL380, where the westerly winds speeds became 35 to 40 ms^{-1} overhead the waypoint locations. It was noted that these westerly winds were situated over a large region of the country, with a sharp decrease in winds speeds (35 to 25 ms^{-1} at 200hPa/FL380) over the north-eastern parts of RSA. The pilots logged 3 CAT events that day, all of MDTT intensity, which were experienced over the central interior of the Northern Cape province. The event waypoints that were logged in the afternoon, included the NIDOX waypoint which was logged mid-day at 175hPa/FL390, the second event logged was at 13h00 UTC at FL350 near the EGTIL waypoint, which is the closest to 250hPa/FL340. The third PIREP, being at the GEDOL waypoint, was logged at 17h00 UTC at 225hPa/FL360. All three events took place in clear air, and thin cirrus clouds were seen to the north-east of the waypoint cluster which is indicative of an upper air jet stream along with wind speeds greater than 30 ms^{-1} overhead. It is seen that both the Ellrod index ENS AVE and ENS PROB forecasts underestimated the CAT events severity but captured the observation once at GEDOL waypoint. The EDR index ENS AVE forecast at the first waypoint, underestimated the CAT event like the Ellrod index forecast. The EDR index ENS AVE forecasts at EGTIL and GEDOL captured the CAT events well. The EDR index ENS PROB forecast captured the CAT event at EGTIL but underestimated the other three CAT events (Table 4.7). It's noteworthy that for both the Ellrod and EDR forecasts, the index ENS AVE values increased with height over the central interior. It is in a similar area where the increase in upper air wind speeds where found. Wind speed that increases with height, is linked to the increase in TKE and thus also EDR values could increase. Wind shear could in turn increase near the cold side of the upper air jet steam, which is a theoretical CAT prone area.

On the 18 November 2018, the upper air flow was zonal, with an upper air jet stream over the western central parts of the country (core wind speeds between 35 to 40 ms^{-1}). The PIREP had logged a MDTT event near the waypoint SLV, Sutherland, at

07h00 UTC at 175hPa/FL400, which is found just south-east of the upper air jet stream core. The Ellrod ENS AVE values predicted an ‘No’ event and the EDR index ENS AVE indicated a MDTT event to occur at 07h00 UTC. Both indices did not capture the observation. The Ellord and EDR indices underestimated the event severity. The Ellrod index ENS PROB forecast become a hit only at lower model levels, whereas the EDR index ENS PROB forecast was a hit an hour later at the same level as the observation (Table 4.7).

The following Table 4.7 is the summary of the zonal flow weather category. All the case studies are now investigated and discussed. A summary of the CSESPS performance will follow Table 4.7 in the next Chapter 5.

Table 4.7: PIREP listed by case study dates categorised under the Zonal flow weather pattern for 2018. The CSEPS forecast output in grey indicates a good forecast (Hit), the up arrow indicates that the forecast event severity was more than observed and down, is less than observed. 'High' indicates that the ensemble probability reflected the observation at a higher model level, and 'low' when it's a level lower than observed. 'No' is when the forecast is below the minimum limit of the lowest threshold. LGT=light, MDT=moderate and SVR=severe.

Weather system and date	**Time (UTC)**	**Waypoint**	**Level (hPa/FL)**	**Observation**	**Ensemble average**		**Ensemble probability and severity**		**Event forecast level**	
Zonal flow					Ellrod	EDR	Ellrod	EDR	Ellrod	EDR
10 Jun 2018	12h18	NIDOX	175hPa/FL410	MDT	LGT ↓	LGT ↓	MDT, 33 ↓	MDT, 33 ↓	Low	Low
	12h55	EGTIL	250hPa/FL340	MDT	LGT ↓	MDT	MDT, 33 ↓	MDT, 67	High	Hit
	16h56	GEDOL	225hPa/FL360	MDT	MDT	LGT ↓	MDT, 58	MDT, 0 ↓	Hit	High
18 Nov 2018	06h52	50 nm S APLEN	175hPa/FL410	LGT	No ↓	MDT ↑	LGT, 8 ↓	LGT, 33 ↓	Low	Low (At 08h00 UTC Hit)

Source: PIREP data and CSEPS data

Chapter 5 : Summary and Discussion

The aim of this study was to establish whether the Ellrod and EDR indices could be utilised to forecast CAT over RSA utilising the ensemble average and probability forecasts from the CSEPS. The research was conducted using 11 case studies when 39 turbulence events were logged by 33 PIREPs. PIREPs were only available for 2018 and all 11 case study dates are therefore also in 2018. The locations of the CAT events were more frequently found clustered over the central parts of the Northern Cape and western parts of the Free State provinces. There were a few PIREPs located over the central eastern interior of the Western Cape province and close to Gauteng and northern parts of KwaZulu-Natal. The CAT events were reported between the levels 250hPa/FL340 and 175hPa/FL410. The following Sections discuss the findings from Chapter 4.

5.1 Severity thresholds

The first objective of this dissertation was to test whether the CAT severity thresholds from literature could be used to identify CAT over RSA. The thresholds were identified by obtaining past literature of where the indices are evaluated (Section 2.2.1; 3.2.6). Each individual CSEPS member Ellrod and EDR index forecast values were calculated and investigated. The values ranged within the thresholds of the indices from literature. The thresholds values used in this dissertation are given in Table 5.1.

Table 5.1: CAT severity threshold values for Ellrod and EDR as identified from literature and used to achieve the first objective of this study (Ellrod and Knapp, 1992; ICAO, 2018).

Index	LGT	MDT	SVR
Ellrod, values multiplied by $10^{-7}s^{-2}$	2 - 4	4 – 8	>8
EDR $m^{2/3}s^{-1}$	0.1 - 0.4	0.4 - 0.7	>0.7

The case studies conducted in Chapter 4 show that these universal thresholds could be applicable over RSA for both the CSEPS ENS AVE and ENS PROB forecasts of CAT. Despite the over and under forecasting of the CAT events that could also partially be due to the subjective reporting of the observation. More research is needed to accurately determine exactly why there is such under and overestimation of the results. Table 5.2 provides a summary of the comparison of the forecasts with the turbulence observations.

Table 5.2: Summary of accuracy of the CSEPS Ellrod and EDR indices total ensemble average and ensemble probability forecasts.

Total of 39 CAT events	Ellrod index forecast ($10^{-7}s^{-2}$)		EDR index forecast ($m^{2/3}s^{-1}$)	
	Forecast correct	Forecast missed	Forecast correct	Forecast missed
Ensemble average (ENS AVE)	31%	69%	44%	56%
Ensemble probability (ENS PROB)	31%	69%	44%	56%

Source: Table 4.5-7.

A total of 39 CAT events were investigated over the three weather categories (Table 4.5; 4.6a,b; 4.7) from 33 PIREPs over 11 case study days. Out of the 39 events, the PIREPs logged 19 LGTT events and 20 MDTT events (observations) where 6 of the events was a combination of LGT-MDTT. The CSEPS Ellrod ENS AVE forecasts were correct 31% of the time, but had the 69% of the forecasts incorrect (Table 5.2). Of the incorrect forecast 33% (36%) were underestimated (overestimated) (Table 5.3). The ENS AVE EDr forecast were correct more often (44%) (Table 5.2) but underestimating and underestimating the turbulence 28% of the time (Table 5.3). The correct forecast for the ENS PROB forecast were the same as the ENS AVE (Table 5.2) but here all the forecast was underestimated with no forecast overestimated (Table 5.3). Table 5.2 also shows that the EDR ENS AVE and PROB forecast fared slightly better than the forecast from Ellrod. Table 5.3 illustrates that both indices struggled to accurately predict the severity of the turbulence. However, in Chapter 6 a discussion is provided on some of the limitations of the PIREP reports to accurately capture the correct severity of turbulence

Table 5.3: Summary of accuracy of the CSEPS Ellrod and EDR severity forecast for the Ensemble average and Ensemble Probability.

Total of 39 CAT events	Ellrod index forecast ($10^{-7}s^{-2}$)		EDR index forecast ($m^{2/3}s^{-1}$)	
	Forecast underestimated	Forecast overestimated	Forecast underestimated	Forecast overestimated
Ensemble average (ENS AVE)	33%	36%	28%	28%
Ensemble probability (ENS PROB)	69%	0%	56%	0%

Source: Table 4.5-7.

5.2 Comparison of the CAT forecasts with PIREPs

The second objective of this study was to compare the CSEPS CAT forecast with the PIREPs and to determine the accuracy of the time, location and height of the turbulence events.

The temporal accuracy of the forecast is discussed first then the precision of the forecast location followed by the exactness of height of the turbulence forecast. Using the limited number of observations of CAT available from the PIREPs, the temporal accuracy of both Ellrod and EDR ENS AVE and PROB forecasts were only 31% and 44% correct respectively (Table 5.2). There were only two cases (21 May 2018, and 18 November 2018), where the forecast got the time of the turbulence wrong, but the height and location were accurately predicted and counted as a missed event. The other missed CAT events (observations) had neither captured the events at an hour later or before at the observed flight level and corresponding model heights and surrounding heights. On 21 May 2018, at 07h00 UCT (45 nm south-west of KYV) the LGT-MDTT event of the EDR ENS PROB forecast had missed the time of the LGTT event and was forecast an hour later (Table 4.6a). Similar on 18 November 2018, at 07h00 UTC (50 nm S APLEN) the LGTT event was captured one hour later as well (Table 4.7). It was noted that, in the COL weather category, there is one CAT event (09h00 at KYV) that captured the MDTT of the LGT-MDTT event, an hour later. While the location and the height were forecast correct and the observation was LGT-MDTT, this event is not included because the forecast went from MDTT to a ‘No’ event at surrounding model levels. The surrounding region around the waypoint were also in favour of MDTT and no opinion could be made to include this event due to lack of observations. Also, there were 4 instances that no turbulence was forecast when it was observed (see the ‘No’ event on table 4.6a, b and 4.7)

Table 5.2 indicates that the CSEPS Ellrod and ENS AVE and PROB turbulence forecasts were captured 31% of the time, and the EDR 44%, outperforming the Ellord forecast. It is not possible to say with certainty how accurate the location of turbulence was due to the lack of observations but the forecast location of CAT fits well with the areas know to be associated with CAT from literature (Section 2.1.2). The detailed case study in Chapter 4 showed how the ENS AVE forecast values for Ellrod and EDR increased in the regions of generally cloud free areas, and in the region to the south of the upper air jet streams. The difference was that the maximum EDR values were slightly northeast of the maximum Ellrod values (Section 4.2). The ENS AVE maximum forecast values pattern also moved to the east as the weather system moved eastwards with time (compare Figure 4.7 and 4.10). In the majority of the cases a similar ENS AVE forecast pattern was found. In the 11 case studies some CAT was generally forecast whenever there was an observation of turbulence.

Out of the total 39 observations from the 33 PIREPs used in the 11 case studies, the events were observed on flight levels between FL280 and FL410. Table 5.2 shows that only 31% of the Ellrod and 44% EDR ENS PROB forecasts were correct. Table 5.4 depicts that the Ellrod and EDR ENS PROB tended to predict the turbulence at levels lower than observed.

Table 5.4: Summary of accuracy of the CSEPS Ellrod and EDR height forecast for the Ensemble average and Ensemble Probability.

Total of 39 PIREPs	Ellrod severity forecast $(10^{-7}s^{-2})$		EDR severity forecast $(m^{2/3}s^{-1})$	
	Forecast model height too low	Forecast model height too high	Forecast model height too low	Forecast model height too high
Ensemble probability	46%	23%	33%	23%

Source: Table 4.5-7.

The levels on which CAT were reported correspond to the theoretical assumption that LGTT to MDTT is found to be more likely near the tropopause and slightly lower near the upper air jet (Section 2.1.2) (Trout and Panofsky, 1968; Hopkin, 1977; Ellrod and Knapp, 1992; de Villiers and van Heerden, 2001; Overeem, 2002). Table 5.4 indicated that the Ellrod and EDR indices have a tendency to forecast the observation at lower model heights. Overall, it seems that the EDR index ENS PROB height forecasts outperformed the Ellrod index ENS PROB height forecasts.

5.3 Accuracy of CAT forecast for different weather systems

The data analysis from the 33 PIREPs obtained over the year of 2018 were used to identify the weather systems most frequently associated with CAT. The 11 case studies were categorized into three weather categories which were COLs, upper air troughs and zonal flow.

The Ellrod outperformed the EDR ENS AVE and PROB forecasts with regards to the COL category. Notably, the CSEPS model captured the known prone CAT regions associated with the COLs found between 500hPa and 200hPa (Section 2.2.2) as well as related regions associated with an upper air trough and jet stream.

In the Table 5.5, it is shown that when COLs occurred, the Ellrod ENS AVE and PROB forecast was 50% correct of the time (Table 5.5). Out of the 8 CAT events, 50% were missed by the CSEPS Ellrod ENS AVE and PROB forecasts (Table 5.5). The EDR ENS AVE and PROB forecast was 25% a hit, and 75% a miss. The forecast accuracy is 50% a hit and miss for the LGTT and MDTT events. In the cases where the LGT-MDTT was reported, two out the six PIREPs, the Ellrod and EDR indices ENS AVE forecasts either got the one or the other part of the severity threshold correct. Otherwise, the combination CAT events from the ENS PROB forecasts were a hit or underestimated the CAT event (Table 5.3; 5.4).

Table 5.5: Summary of accuracy of severity of the the CSEPS Ellrod and EDR forecast for the Ensemble average and Ensemble Probability together for the three weather categories.

Number of PIREPs	Ellrod severity forecast $(10^{-7}s^{-2})$		EDR severity forecast $(m^{2/3}s^{-1})$	
	Forecast correct	Forecast missed	Forecast correct	Forecast missed
COL (8)	50%	50%	25%	75%
Trough (27)	26%	74%	52%	48%
Zonal flow (4)	25%	75%	25%	75%

Source: Table 4.5-7.

The upper air trough weather category had the most PIREPs but the COL weather category had the highest accuracy out of all three weather categories. It can be seen that the EDR forecast (52%) predicted turbulence better than Ellrod (26%). There was a total of 14 LGTT events and 13 MDDT events. EDR forecast LGTT accurately more often than Ellrod. The same is true for MDTT events. The ENS PROB forecasts of both indices had a greater tendency towards underestimation compared to the ENS AVE forecasts, whereby a more general overestimation occurred.

Under the Zonal flow weather category, the Ellrod and EDR indices captured 25% of the ENS AVE forecasts. The Ellrod index ENS AVE forecasts of the severity were 75% underestimated, with no overestimation noted. The EDR ENS AVE indicated a similar trend as the Ellrod forecast as well as for the EDR ENS PROB forecast. Both indices underestimated the first event. The EDR index overestimated the last case study date when the CAT events took place at 175hPa/FL410. (Section 4.3.3).

Overall, the Ellrod forecasts outperformed the EDR forecast for the COL weather category. The EDR outperformed the Ellrod when investigating the trough category and as seen from the zonal category, both indices did similarly.

The EDR index forecasts also indicated less uncertainty than the Ellrod index forecast. The Ellrod index overestimated the events at times when the observations were closer to the upper air trough axis and beneath the upper air jet stream more than the EDR index forecasts.

The LGT to MDT CAT events that were observed were related to a region where wind shear takes place in the upper air levels relative to the development of an upper air trough, COL and upper air jet stream (Section 2.1.2). When the upper air had zonal flow the EDR and Ellrod indices forecasts indicated a similar performance. The other CAT events were either underestimated or a hit at much lower model levels. The location of the CAT in the three different weather patterns correlated with previous study results (Chapter 2) (Hopkins, 1977; Overeem, 2002; Holton, 2004; Sharman et al., 2012) (Section 2.1.2).

Chapter 6 : Conclusion and Recommendations

6.1 Conclusion

The overall purpose of this dissertation was to improve the forecasting of a very specific type of turbulence, namely Clear Air Turbulence. Forecasting CAT accurately is important; as many as 65% of weather-related incidence by aircraft is due to CAT. There is also an ever-increasing demand for domestic and international flights. Improved forecasting of CAT could save lives and millions of dollars to the aviation industry.

The South African Weather Service (SAWS) in-house convective scale ensemble prediction system (CSEPS) has numerous diagnostics for CAT prediction and yet these diagnostics are not utilized operationally in the forecasting offices in South Africa. The results emanating from this dissertation intend to persuade aviation forecasters in South Africa to use the CSEPS Ellrod and EDR forecasts with confidence.

The aim of this study was to determine if the Ellrod and EDR indices, can predict clear air turbulence over South Africa utilising the ensemble average and probabilistic forecast from the CSEPS.

A total of 33 PIREPs were obtained with a total of 39 CAT events which all occurred in 2018. These events took place over 11 days that were identified for further analysis (Section 3.2.6). Due to the limited number of PIREP reports a case study approach was used to conduct this research. Shultz (2010) stated that case studies are indispensable to meteorology and also postulates that operational meteorologists (forecasters) are in a very good position to produce case studies.

Severity threshold values for the Ellrod and EDR indices, was established from literature. The Ellrod and EDR indices ensemble average and probability from the CSEPS members individual forecast values were found to fall within the range of the values form literature when compared to the PIREP report CAT events. The Ellrod index ensemble average forecast overestimated the severity of the CAT events more often than the EDR index forecasts. The ensemble probability forecasts underestimated the severity of the CAT events for both indices' forecasts. Overall, there was a large tendency to underestimate the severity.

The Ellrod and EDR ensemble average and probability forecast values from CSEPS were also compared to the PIREPs to determine the accuracy of the time, location, and height of the forecasts. The temporal and spatial accuracy of the CSEPS was considered to be good considering the limited number of observations available. There were only two PIREP events that were accurate at the location and model level but not temporally accurate and captured the observation one hour later. The PIREPs waypoints that were utilised, were noted to be in continuously similar regions. The accuracy of the CSEPS to predict the height of the CAT event was well captured by the EDR index ENS PROB forecast, however more likely at higher model levels. The Ellrod index ENS PROB forecasts captured the observations more frequently at lower levels than observed.

The three dominant weather systems identified when CAT occurred were COLs, upper troughs and upper air zonal flow. It was found that the CSEPS did the best with upper air troughs. The CSEPS EDR forecast outperformed the Ellrod for the trough weather category while the Ellrod fared better than the EDR forecasts for the COL weather category, whereas, for the zonal weather category, the Ellrod and EDR had a similar outcome. It is well known in the forecasting offices in South Africa that COLs are weather systems associated with CAT. The results from this research expands this understanding to include upper air troughs as well as when zonal flow occurs. de Villiers and van Heerden (2001) found that a jet stream is a foremost CAT indicator on the synoptic scale while Hopkins (1977) stated that the upper air jet is also prevalent east of the upper air troughs. The case studies conducted in this dissertation showed an increase in index values from both the Ellrod and EDR, towards and within the vicinity of the upper air jet stream (Chapter 4). Another recurring CAT region that was seen from the case studies was on the cold side of the jet stream core (Section 4.4). An increase in probability of CAT on the rear side of the upper air trough, which corresponds to the findings of Hopkins (1977) was also noted. The forecast CAT regions relative to the COL also correlated well with previous study findings, where LGT to MDT CAT was seen east of the COL, and in the region of wind shear associated with the jet stream (Chapter 2). The wind speeds of the upper air jet stream core that were forecast in the case studies were in general >30 ms^{-1}, which corresponds to what was stated by Hopkins (1977), who also suggested that a wind speed of at least 25 ms^{-1} is needed to generate strong enough shear so as to induce

CAT. It is however noteworthy that, when zonal flow is present, CAT occurred that may not explicitly be influenced by the upper air jet stream core which is present and may be weaker than 30 ms^{-1} at the core. Yet there were winds stronger than 25 ms^{-1} which could lead to the assumption that the atmosphere is conducive of wind shear strong enough to overcome the stable atmospheric conditions. More research is needed to confirm this subjective assumption.

6.2 Limitations

One of the major challenges in this research was obtaining observations of CAT. An appeal was made to the South African Airliners Association (SAAA) and the South African Civil Aviation Authority (SA CAA) to have access to their database of CAT reports, and this resulted in data being made available for one year only namely 2018. One of the challenges in using PIREPs is that not all pilots report CAT events and at most our database of CAT events is only a subset of possible CAT occurrences. The lack of observations of turbulence is an historic problem in South Africa. A previous study on CAT over South Africa had only fifteen pilot reports available over a three-year period from 1993 to 1995 (de Villiers and van Heerden, 2001). They made an appeal to the SAAA and the SA CAA staff to encourage pilots to log their CAT encounters. We had a total number of 226 PIREPs in 2018 and it appears as if this appeal bared fruit. We would nevertheless encourage all pilots to report all turbulence events they encounter.

A further challenge in using the PIREP observations is that the reports are subjective observations from different individuals. Therefore, the same criteria may not always apply in the observations of CAT from one event to the next. The reported CAT events hold uncertainty towards the CAT intensity (Sharman and Pearson, 2017). The intensity categories, LGT, MDT and SVR, are less likely to be reported separately due to the pilot flying through the region of CAT and therefore reporting the intensity as a combination of LGT to MDT, or MDT to SVR (Sharman and Pearson, 2017). This made the evaluation of the CSEPS difficult in terms of only having thresholds for the separate intensity categories. Another limitation towards PIREPs is that there is no definite certainty that the turbulence encountered by the pilots is indeed happening in clear air when logged at CAA. The more experienced the pilot becomes, the more unlikely it becomes for the pilot to report LGT-MDT CAT events. This can lead to underreporting of these encounters due to the fact that CAT is aircraft specific and experienced differently, due to the size and aerodynamics of the aircraft playing a role (Overeem, 2002).

This study had received a total of 226 PIREPs that were investigated, but only 33 were used in the research (as outlined in Section 3.2.6). A non-trivial consideration for the limited number of cases used was the availability of computing resources on the South African Weather Service in-house operational high preforming computer. This resulted in the ability to only run 11 case studies within a reasonable time frame for this research without interrupting operational NWP simulations.

6.3 Future Research and Recommendations

The turbulence forecast maps generated in the case studies, in practice would contribute to the forecasting of CAT over RSA at SAWS. The contribution from the conjoint display of the Ellrod index and EDR index forecasts, as presented in the present study (Chapter 4), indicates a possible increase in certainty towards the forecast location and the probability of the CAT event. The ability to forecast CAT regions with some certainty at atmospheric heights other than near the upper air jet stream core and away from the jet stream is shown to be possible (Chapter 4). The waypoints where CAT was reported were noted to be cluster in similar regions and could be conceptually used in the practical workplace. The severity of the CAT forecast will carry confidence based on the ensemble probability, which has been shown to be a good indicator, especially in relation to upper air troughs and zonal flow (Chapter 4). The ensemble average of both indices' forecasts could contribute as an additional ensemble member to the CSEPS model, thereby increasing the total members of 12 to 13. The ensemble meteograms are interpreted as a visualisation of the ensemble members behaviour. The ensemble tendency towards a certain CAT event threshold is helpful, since it leads to an increase in certainty towards a forecast CAT event (Storer et al., 2012; Gill and Buchanan, 2014; Storer et al., 2018).

It is recommended that forecaster workshops take place where the advantages of using the CSEPS CAT forecast can be demonstrated. They should be introduced to the EDR and Ellrod indices and there should be consensus on how the forecast should be made available in forecasting offices. Storer et al. (2018) provide some guidance on how ensemble forecast should be made available and proposed the graphical turbulence guide (GTG) over America. It is important to move away from deterministic forecasts as there is no indication of uncertainty.

The results from this research indicate that there is merit in using Elrrod and EDR from the CSEPS to predict CAT operationally. To further investigate the worth of these forecasts it is recommended that all PIREPs available for 2018 be used to isolate CAT events. This will allow for a more comprehensive and objective statistical analysis of model performance when predicting CAT. Furthermore, the CSEPS has several other turbulence forecasting indices available such as mountain waves turbulence, three-dimensional frontogenetic index, dissipation from convectively generated gravity waves index (Bechtold et al., 2021) and the Richardson's number. It is recommended that those PIREPs not associated with CAT be compared to these indices in order to determine their accuracy. Goecke and Machulskaya (2021) offer techniques on how to go about verifying ensemble probabilistic forecasts.

It is recommended that airline pilots be encouraged to report CAT more frequently. It is also recommended that the South African Airliners Association (SAAA) and the South African Civil Aviation Authority (SA CAA) make these observations available to researchers in order to facilitate research on turbulence.

References

BAKKER, H., 1993: Drie objectieve indices voor clear-air turbulence nader bekeken, *Technische rapporten*; TR-160, KNMI, de Bilt.

BALMEZ, M. & STEFAN, S., 2014. On the formation mechanism of low-level jet over Bucharest's airports. *Romania Journal of Atmospheric Physics*, 59, 792-807.

BARBER, K.A., MULLENDORE, G. & ALEXANDER, M.J., 2018. Out-of-Cloud Convective Turbulence: Estimation Method and Impacts of Model Resolution. *Applied Meteorology and Climatology*, 57, 121-136.

BECHTOLD P., BRAMBERGER, M., DORNBRACK, A., ISAKSEN, L., & LEUTBECHER, M., 2021. Experimenting with a clear air turbulence (CAT) index from the IFS. *Technical memorandum* No.874. Germany: ECMWF, p.1-15.

BEER, T., 1976. Mountain waves. *Science Progress*, 63, 1-25.

BOOMGAARD, M., 2014. SAA pilot gets hero’s welcome. IOL. 20 July 2014. [Online] Available at: https://www.iol.co.za/news/south-africa/saa-pilot-gets-heros-welcome-1722501. [Accessed 10 July 2022].

BOPAPE, M., PLANT, R.S. & COCEAL, O., 2020. Resolution Dependence of Turbulent Structures in Convective Boundary Layer Simulations. *Atmosphere*, 11, 1-28.

BROWN, R., 1973. New indices to locate clear-air turbulence. Meteor. Mag, 102, pp.347-361.

CAA, 2013. CAA Standards & Procedures (ATCIs) Manual. [Online] Available at: http://www.caa.co.za/Standards%20and%20Procedures%20Manuals/Contents.pdf.

CHEUNG, J.C..H, HALLY, A., & HEIJSTEK, J.J., 2015. Recommendations on trajectory selection in flight planning based on weather uncertainty. Conference: SESAR Innovation Days 2015. January 2015. Imaged used Hally, A.

CHAN, P.W. & WONG, W.K., 2014. An Analysis of a Severe Turbulence Event Encountered by an Aircraft over the South China Sea and the Application of Numerical Weather Prediction Models in the Early Alerting of the Event. *Advances in Meteorology*, 2014.

COLSON, D. & PANOFSKY, H.A., 1965. An index of clear air turbulence. *Quarterly Journal of the Royal Meteorological Society*, 91(390), pp.507-513.

DE VILLIERS, M. & VAN HEERDEN, J., 2001. Clear air turbulence over South Africa. *Meteorological Applications*, 8, 119-126.

DOLAPTCHIEV, S.I., Achatz, U. & Reitz, T., 2019. Planetary geostrophic Boussinesq dynamics: Barotropic flow, baroclinic instability and forced stationary waves. *Quarterly Journal of the Royal Meteorological Society*, DOI: 10.1002/qj.3655, pp.1-15.

DUTTON, J.A., 1971. Clear-Air Turbulence, Aviation, and Atmospheric Science. *Reviews of Geophysics and Space Physics, 9, 613-657.*

DUTTON, J.A. & PANOFSKY, H.A., 1970. Clear air turbulence: A mystery may be unfolding. *Science*, 167, 937-944.

EBERT, E.E., 2001. Ability of a Poor Man's Ensemble to Predict the Probability and Distribution of Precipitation. *American Meteorological Society Monthly Weather Review*, 129, 2461-2480.

ELLROD, G.P. & KNAPP, D.I., 1992. An objective clear-air turbulence forecasting technique: Verification and Operation Use. *Weather and Forecasting*, 7, 150-165.

ELLROD, G.P. & KNOX, J.A., 2010. Improvements to an Operational Clear-Air Turbulence Diagnostic Index by Addition of a Divergence Trend Term. *Weather and Forecasting*, 25, 789-798.

ELLROD, G.P., LESTER P.F., & EHERNBERGER J., 2002: Clear air turbulence. *Encyclopedia of the Atmospheric Sciences*, J. R. Holton et al., Eds., Academic Press, 393–403.

Eumetrain, 2012. Applications of Meteorsat Second Generation (msg), module notes. Available from: http://www.eumetrain.org/data/4/451/english/courses/msgcrs/index.htm [Accessed 08 Nov. 2019].

EUMETSAT, 2020. Meteosat Series. Available from: https://www.eumetsat.int/our-satellites/meteosat-series [Accessed 8 Oct. 2020]

GALLEGO, D., RIBERA, P., GARCIA-HERRERA, R., HERNANDEZ, E. & GIMENO, L., 2005. A new look for the Southern Hemisphere jet stream. *Climate Dynamics*, 24.

GELDENHUYS, M. & MESCHT, D.V.D., 2019. Observations of mountain waves with interference generated by coastal mountains in South Africa. *Meteorology Applications, 26(3), pp.409-415*.

GILL, P.G. & BUCHANAN, P., 2014. An ensemble based turbulence forecasting system*. Meteorology Applications*, 21, 12-19.

GOECKE, T. & MACHULSKAYA, E., 2021. Aviation Turbulence Forecasting at DWD with ICON: Methodology, Case Studies, and Verification. *Monthly Weather Review*, 149(7), pp.2115-2130.

GOLDING, B., ROBERTS, N., LEONCINI, G., MYLNE, K. & SWINBANK, R., 2016. MOGREPS-UK Convection-Permitting Ensemble Products for Surface Water Flood Forecasting: Rationale and First Results. *Journal of Hydro-meteorology*, 17, 1383-1406.

HAMAN, K.E. & BAJER, K., 2011. Prediction of clear-air turbulence induced by short gravity waves. *Journal of Physics: Conference Series*, 318.

HAMAN, K.E., 1962. On some possible causes of clear air turbulence. *Acta Geophysical Polonica*, 10, 335-357.

HOLOPAINEN, E.O., 1963. On the dissipation of kinetic energy in the atmosphere 1. Tellus, 15(1), pp.26-32. University of Stockholm.

HOLTON, J.R., 2004. *An introduction to dynamic meteorology*. 4th ed. USA: Elsevier Academic Press, pp.115-122, 142, 229, 274, 347-349.

HONGBO, L., MINGYANG, H., BIN, W. & QINGHONG, Z., 2014. Advance in low-level jet research and future prospects. *Journal of Meteorological Research*, 28, 57-75.

HOPKINS, L., 1977. Forecasting Techniques of Clear-air Turbulence Including that Associated with Mountain Waves. *Technical note No.155*. Geneva, Switzerland: World Meteorological Organization.

INTERNATIONAL CIVIL AVIATION ORGANIZATION (ICAO), 2018. Annex 3 — Meteorological Service for International Air Navigation. 12th ed.: INTERNATIONAL CIVIL AVIATION ORGANIZATION.

KHOSA, E., 2019. *South African Civil Aviation Authority (SACAA) Annual report* 2018-2019. Johannesburg, South Africa.

KIM, J.H. & CHUN, H.Y., 2011, August. A Numerical Study on Convectively Induced Turbulence (CIT) Encounter above a Dissipating Deep Convection. In *15th Conference on Aviation, Range, and Aerospace Meteorology.*

KOPEĆ, J.M., HAMAN, E.K. & BAJER, K., 2011. Prediction of clear-air turbulence induced by short gravity waves. In *13th European Turbulence Conference (ETC13)*. IOP Publishing.

KUDO, A., 2011. *Development of JMA's new turbulence index*. [Online] Available at: http://ams.confex.com/ams/14Meso15ARAM/webprogram/paper190738hmtl [Accessed 22 October 2019].

LANDMAN, S., ENGELBRECHT, F.A., ENGELBRECHT, C.J., DYSON, L.L. & LANDMAN, A.W., 2012. A short-range weather prediction system for South Africa based on a multi-model approach. *Weather SA*, 38(5).

LORENZ, E.N., 1955. Available Potential Energy and the Maintenance of the General Circulation, *Tellus*, 7:2, 157-167, DOI: 10.3402/tellusa.v7i2.8796

MARTNER, B. E., 1997. Vertical Velocities in a Thunderstorm Gust Front and Outflow. Journal of Applied Meteorology 36, 5, 615-622, available from: < https://doi.org/10.1175/1520-0450(1997)036<0615:VVIATG>2.0.CO;2> [Accessed 10 July 2020]

MOKOENA, S., 2018. *South African Civil Aviation Authority (SACAA) annual report* 2017/2018. Pretoria: SACAA Board.

National Centers for Environmental Prediction (NCEP) /National Weather Service/NOAA/U.S. Department of Commerce. 2000. NCEP/DOE Reanalysis

2 (R2). Research Data Archive at the National Center for Atmospheric Research, Computational and Information Systems Laboratory. https://doi.org/10.5065/KVQZ-YJ93. Accessed 27 Oct 2022.

NAIDOO, L., 2017. Turbulence causes mid-air panic on Kulula flight to Cape Town. Daily Voice. [Online] Available at: https://www.dailyvoice.co.za/news/turbulence-causes-mid-air-panic-on-flight-to-cape-town-9630954. [Accessed 10 July 2022].

NDARANA, T., RAMMOPO, T.S., BOPAPE, M., PREASON, C.J.C. & CHIKOORE, H., 2020. Downstream development during South African cut-off low pressure systems. *Atmospheric Research*, 249.

OLIVEIRA, M.I., NASCIMENTO, E.L. & KANNENBERG, C., 2018. A new look at the identification of low-level jets in South America. *Monthly Weather Review,* 146(7), pp.2315-2334.

OVEREEM, A., 2002. *Verification of clear air turbulence forecasts*. De Bilt, The Netherlands: KNMI.

PRESTON-WHYTE, R.A. & TYSON, P.D., 1988. *The Atmosphere and Weather of Southern Africa.* Oxford University Press.

SCHULTZ, D.M., 2010. How to research and write effective case studies in meteorology. *Electronic Journal: Severe Storms Meteorology*, 5, 1-18.

SHARMAN, R.D., TEBALDI, C., WIENER, G. & WOLFF, J., 2006. An Integrated Approach to Mid- and Upper-Level Turbulence Forecasting. *Weather and Forecasting*, 21, 268-287.

SHARMAN, R.D., TRIER, S.B., LANE, T.P. & DOYLE, J.D., 2012. Source and dynamics of turbulence in the upper troposphere and lower stratosphere: A review. *Geophysical research letters*, 39.

SHARMAN, R.D & PEARSON, J., 2017. Prediction of Energy Dissipation Rates for Aviation Turbulence. *Applied Meteorology and Climatology*, 56, 317-337.

SINGLETON, A.T. & REASON, C.J.C., 2007. Variability in the characteristics of cut-off low pressure systems over subtropical southern Africa. *International Journal of Climatology: A Journal of the Royal Meteorological Society*, 27(3), pp.295-310.

SOUTH AFRICAN WEATHER SERVICE (SAWS), 2019. *About Us* - WeatherSA Portal [Online]. Available at: http://www.weathersa.co.za/home/about. [Accessed 15 September 2019].

SPENSBERGER, C., SPENGLER, T. & LI, C., 2017. Upper-Tropospheric Jet Axis Detection and Application to the Boreal Winter 2013/14. *Monthly Weather Review*, 145, 2363-2374.

STANDER, J.H., DYSON, L.L., & ENGELBRECHT, C.J., 2016. A snow forecasting decision tree for significant snowfall over the interior of South Africa. *South*

African Journal of Science, 112(9-10), 1-10. https://dx.doi.org/10.17159/sajs.2016/20150221

STORER, L.N., WILLIAMS, P.D. & GILL, P., 2019. Aviation Turbulence: Dynamics, Forecasting, and Response to Climate Change. *Pure and Applied Geophysics*, 176, 2081-2095.

STORER, L.N., WILLIAMS, P.D. & JOSHI, M.M., 2017. Global Response of Clear-Air Turbulence to Climate Change. *Geophysical research letters*, 44, 9976-9984.

STRANGE SOUNDS, 2014. *Are these planes entering a new dimension? No, It's just wake vortex.* [Online] Available at: https://strangesounds.org/2014/05/are-these-planes-entering-a-new-dimension-no-its-just-wake-vortex.html. [Accessed 10 July 2022].

STULL, R.B., 2018. *Weather for sailing, flying and snow sports*. Course notes. [Last update October 2018] [Online] Available at: https://www.eoas.ubc.ca/courses/atsc113/flying/met_concepts/03-met_concepts/03e-CAT/index.html. [Accessed 08 November 2019].

STULL, R.B. 1988. *An introduction to boundary Layer Meteorology*, The Netherlands, Kluwer Academic Publishers Group.

TENNANT, W.J., TOTH, Z. & RAE, K.J., 2007. Application of the NCEP Ensemble Prediction System to Medium-Range Forecasting in South Africa: New Products, Benefits, and Challenges. *Weather and Forecasting*, 22, 18-35.

TURNER, J., 1999. Development of a mountain wave turbulence prediction scheme for civil aviation. *Forecasting Research Technical Report* (265). United Kingdom.

VENKATESH, T.N. & MATHEW, J., 2013. The problem of clear air turbulence: Changing perspectives in the understanding of the phenomenon. *Indian Academy of Sciences*, 38, 707-722.

WALLACE, J.M. & HOBBS, P.V., 2006. *Atmospheric Science An Introductory Survey*, London, Academic Press Publications.

WEDAWATTA, G., INGIRIGE, B. & AMARATUNGA, D., 2011. *Case study as a research strategy: Investigating extreme weather resilience of construction SMEs in the UK*.

WILKS, D.S., 2011. *Statistical Methods in the Atmospheric Sciences*, Elsevier Inc.

WILMS, H., BRAMBERGER, M. & DÖRNBRACK, A., 2020. Observation and simulation of mountain wave turbulence above Iceland: Turbulence intensification due to wave interference. *Quarterly Journal of the Royal Meteorological Society*, 146(732), pp.3326-3346.

WORLD METEOROLOGY ORGANIZATION, 2007. *World Meteorological Organization, Aviation hazards: Education and training program*, Geneva - Switzerland

WORLD METEOROLOGY ORGANIZATION, 2016. *The World Meteorological Organization: AMDAR Observing System*. Geneva, Switzerland. [Online] Available at: https://www.wmo.int/pages/prog/www/GOS/ABO/AMDAR/. [Accessed 8 September 2019].

Yamada. Y, 2008: Technical development for turbulence probability forecast. Note for aviation weather (in Japanese, Kouku kishou note). 1-11.